

**Spatial Beam Shaping of High-Power Ultrashort Laser Pulses**

**Shuyan Zhang**

**Luoyang City, He'nan Province, P.R.China**

**Master of Science, the College of William and Mary, Virginia, 2002  
Master of Science, Fudan University, Shanghai, P.R.China, 2000  
Bachelor of Science, Fudan University, Shanghai, P.R.China, 1997**

**A Dissertation presented to the Graduate Faculty  
Of the College of William and Mary in Candidacy for the Degree of  
Doctor of Philosophy**

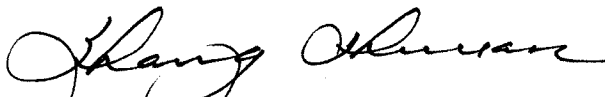
**Applied Science Department**

**The College of William and Mary  
August, 2007**

# APPROVAL SHEET

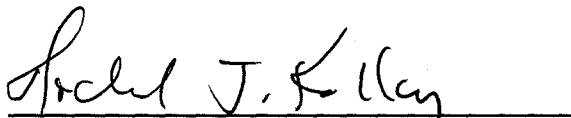
This dissertation is submitted in partial fulfillment of  
the requirements for the degree of

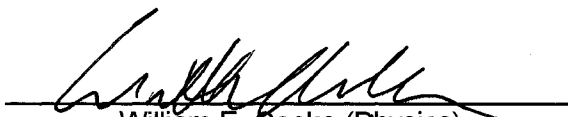
Doctor of Philosophy


  
\_\_\_\_\_  
Shuyan Zhang

Approved by the Committee, May 2007

  
\_\_\_\_\_  
Gunter Lüpke, Chair

  
\_\_\_\_\_  
Michael J. Kelley

  
\_\_\_\_\_  
William E. Cooke (Physics)

  
\_\_\_\_\_  
Jan L. Chaloupka (Physics)

## ABSTRACT

This thesis presents both theoretical and experimental studies of a diffractive beam shaping system for ultrashort high-power laser pulses.

A theoretical model is developed to simulate the reshaped intensity profiles for a 100-fs pulse with various energy levels. Both temporal evolution and spatial intensity distribution of the pulse at the target plane of the beam shaping system are calculated. Numerical simulation shows that after passing through the beam shaping system, the pulse front is significantly curved due to the propagation time delay, and the pulse duration time through the target plane is broadened because of the group velocity dispersion. However, for relatively low energy pulses (on the order of millijoules), although the intensity distribution is changed considerably, the fluence top-hat profile is well maintained. This feature extends the application of this beam shaping system into the regime of ultrashort laser pulses. Theoretical calculation also shows the limit when the top-hat profile starts to degrade. For very high-energy laser pulses ( $>20$  mJ per pulse), the homogeneous fluence profile, as well as the intensity distribution, is destroyed due to the non-linear self phase modulation.

This thesis also presents an experimental study of the beam shaping system for ultrashort high-power laser pulses. A terawatt CPA laser amplification system was built in order to verify the theoretical simulation in experiment. The laser amplification system adopts a multi-pass configuration. The output of this CPA amplifier is operating at 30 Hz repetition rate with a pulse energy of 20 mJ/pulse. The compressed pulse duration is 70 fs, resulting in a pulse peak power of 0.3 TW. Experimental results of the beam shaping system with ultrashort laser pulse input agree with the numerical simulation of the reshaped fluence profiles at various energy levels from 6nJ to 20 mJ. The experimental results confirm the validity of this diffractive beam shaping system for ultrashort pulses with a pulse energy on the order of millijoules. While millijoule pulses are commonly used in the micromachining technology, the adaptability of this diffractive beam shaping system is greatly improved.

Dedicated to my parents, Zhizhong Song & Xiumin Zhang

# TABLE OF CONTENTS

	<b>Page</b>
<b>Abstract</b> .....	<b>iii</b>
<b>Acknowledgements</b> .....	<b>viii</b>
<b>List of Tables</b> .....	<b>ix</b>
<b>List of Figures</b> .....	<b>x</b>
<b>1 Introduction</b> .....	<b>2</b>
1.1 Field mapping laser beam shaping techniques.....	2
1.1.1 Reflective beam shaping system .....	4
1.1.2 Refractive beam shaping system.....	7
1.1.3 Diffractive beam shaping system .....	11
1.2 Beam integration techniques.....	13
1.2.1 Multi-aperture beam integration approach.....	14
1.2.2 Band limited optical diffuser beam shaping technique.....	16
1.3 Scope of this dissertation .....	19
<b>2 Beam shaping system</b> .....	<b>21</b>
2.1 Theory of wave propagation and diffraction.....	22

2.1.1 Fresnel approximation .....	23
2.1.2 Stationary phase approximation.....	24
2.2 Modeling of ultrashort pulse beam shaping.....	25
2.3 Nonlinear optical effects.....	33
2.4 Experimental setup.....	37
2.4.1 Fabrication of multi-level beam shaping element.....	37
2.4.2 Beam size control and profile diagnostic systems.....	39
<b>3 Terawatt laser amplification system.....</b>	<b>43</b>
3.1 Introduction .....	43
3.2 Pulse stretcher.....	49
3.3 Preamplifier.....	55
3.4 Power amplifier.....	62
3.5 Pulse compressor.....	66
<b>4 Results and discussion.....</b>	<b>74</b>
4.1 Numerical simulation.....	74
4.1.1 Low-energy pulse beam shaping.....	74
4.1.2 Alignment and scaling errors.....	82
4.1.3 Medium- and high-energy pulse beam shaping.....	84
4.2 Experimental data.....	87
4.2.1 Low-energy pulse beam shaping.....	87
4.2.2 Alignment and scaling errors.....	90
4.2.3 Medium- and high-energy pulse beam shaping.....	94
<b>5 Conclusion and future work.....</b>	<b>97</b>

5.1 Conclusion.....	97
5.2 Future work.....	98
<b>Bibliography .....</b>	<b>101</b>
<b>Vita .....</b>	<b>112</b>

## ACKNOWLEDGEMENTS

My first, and most earnest, acknowledgement must go to my advisor, Professor Gunter Lüpke. Without his support and guidance, this dissertation would not have been possible. I am indebted to him not only for his encouragement and mentoring throughout my doctoral studies at the College of William and Mary, but also for all that he has shared with me over the years that I know will benefit me in many ways throughout my career.

I owe special thanks to my doctoral dissertation committee members: Prof. Michael Kelley of Applied Science Department, Prof. William Cooke and Prof. Jan Chaloupka of Physics Department for their comments and suggestions during the course of completing this dissertation. Their academic support and input are greatly appreciated.

I am fortunate to have the opportunity to work with a group of energetic people in Dr. Lüpke's lab: Yuhang Ren, Haibin Zhao, Baozhou Sun, Qiguang Yang, Andrea Lucarelli, Erik Spahr, Kevin Smith, Yichun Fan, Ran Yang, Andreas Peterson and Stephanie Hümmert. I appreciate all their friendships and their collective encouragement to finish this dissertation. I have enjoyed working with and learned a lot from each of them.

I also thank Prof. Greg Smith at the College of William and Mary for providing us computing resources. The calculations were made on the Sciclone computer cluster system at the College of William and Mary.

It is impossible to have my research career without my parents' love and support. Both have instilled many admirable qualities in me and given me a good foundation with which to meet life. My gratitude is also extended to my brother – Shuwei Zhang and my sister – Shuping Zhang. Their constant love, encouragement and support have always been the source of my strength and motivation.

This acknowledgment would not be complete without giving thanks to my wife Ying Cheng for supporting me in so many ways, for being the source of energy and joy that keep me going. She has my everlasting love.

## LIST OF TABLES

	Page
3.1. Specifications of the beam seeding the CPA amplifier.....	49
3.2. Specifications of the grating used in the pulse stretcher.....	52
3.3. Physical specifications of the Ti:sapphire crystal used in the eight-pass preamplifier. ....	55
3.4. Optical specifications of the Ti:sapphire crystal in the preamplifier.....	58
3.5. Specifications of the eight-pass preamplifier .....	59
3.6. Amplification factor and pulse energy per pass. ....	60
3.7. Thermal properties of various heat transfer media .....	63
3.8. Specifications of the four-pass power amplifier.....	64
3.9. Pulse duration versus spectral bandwidth for Gaussian-shaped pulses .....	65
3.10. Specifications of the pulse compressor .....	67

## LIST OF FIGURES

	Page
1.1. Aperture method to obtain a nearly flat intensity distribution.....	4
1.2. One-mirror beam shaping system, $f(r)$ is the mirror surface, and $F(R)$ is the receiver surface.....	5
1.3. Reflective surface in a one-mirror beam shaping system converting a cosine beam into a homogeneous intensity distribution. ....	7
1.4. A two-lens beam shaping system converting a laser beam into a uniform intensity distribution .....	7
1.5. Surface profiles of aspherical lenses in a refractive beam shaping system converting a Gaussian beam into a uniform intensity distribution.....	10
1.6. A typical diffractive beam shaping system consisting of a phase element and a transform element. The target plane is at the focal plane of the transform element. ....	12
1.7. Phase delay function $\phi(\xi)$ that turns a Gaussian beam into a top-hat profile .....	13
1.8. A diffracting multi-aperture beam integration system .....	14
1.9. Effect of a multi-aperture beam integration system: (a) two-dimensional intensity distribution on the target without the lenslet array, and (b) one-dimensional intensity distribution in the target plane with the lenslet .....	16
1.10. Binary phase structure of a diffractive diffuser converting a Gaussian laser beam into a ring shape .....	18
1.11. Intensity profile at the target plane of the ring diffuser. ....	19
2.1. Geometry for the Rayleigh-Sommerfeld diffraction integral. $A(x_A, y_A, z_A)$ is	

the observation point, and $O(x,y,0)$ is a secondary wave source in the aperture plane $(x, y, z=0)$ .	22
2.2. A typical diffractive beam shaping system.	26
2.3. Geometrical optics representation of the beam shaping process.	26
2.4. Phase delay in different regions of the beam passing through the beam shaping element.	30
2.5. Surface profile of the beam shaping element as a function of normalized radius	31
2.6. Comparison of the theoretical curve and the 10th order polynomial fitting of the phase delay function. The dots represent the theoretically calculated.	38
2.7. Surface profile of the phase delay element designed for $\beta=32$ . The smooth curve is the theoretical surface profile, compared with the fabricated step structure.	39
2.8 Experimental setup of the beam shaping system consisting of a laser beam source, a CPA laser amplification system, a beam shaping setup and a beam diagnostic system.	40
2.9. Beam expander with variable magnification	41
3.1. Scheme of an amplifier system based on CPA technique	45
3.2. Schematic of the Terawatt laser amplifier system	48
3.3. Optical setup of the pulse stretcher.	49
3.4. Geometrical optics illustration of the pulse stretcher.	50
3.5. Spectrum of the seed beam before entering the pulse stretcher. Bandwidth of this spectrum is 40.35 nm centered at 800 nm.	53
3.6. Spectrum of the seed beam after the pulse stretcher. The bandwidth of this spectrum is 32.8 nm.	53
3.7. Comparison of the spatial mode profiles of the seed beam before and after the pulse stretcher.	54
3.8. Autocorrelation measurement of the stretched pulse. FWHM of the curve is 220 ps. Assuming a Gaussian pulse profile, the pulse width is 156 ps.	54

3.9. Optical setup of the eight-pass amplifier .....	55
3.10. Synchronization timing scheme used in the amplification system.....	57
3.11. Spatial mode profile of the amplified beam after the eight-pass. ....	60
3.12. Autocorrelation measurement of the pulse width after the eight-pass preamplifier. Assuming a Gaussian temporal profile, the pulse duration is 181 ps.....	61
3.13. stability of the output power from the eight-pass amplifier: (a) pulse-to-pulse stability of the unamplified seed beam; (b) pulse-to-pulse stability of the amplified seed beam.....	61
3.14. Configuration of the four-pass power amplifier.....	62
3.15. Spectrum of the amplified pulse after the four-pass amplifier.....	64
3.16. Autocorrelation measurement of the pulse width after the four-pass preamplifier. Assuming a Gaussian temporal profile, the pulse duration is 189 ps.....	65
3.17. Optical configuration of the pulse compressor.....	66
3.18. Spectrum of the pulse after the compressor. The bandwidth of this spectrum is 23.4 nm.....	68
3.19. Autocorrelation measurement of the pulse width after the pulse compressor.....	68
3.20. Beam mode profile after the compressor: (a) CCD captured beam profile; (b) intensity distribution along the horizontal cross section of the beam profile; and (c) intensity distribution along the vertical cross section of the beam profile.....	69
3.21. Layout of the whole CPA laser amplification system. (a) Tsunami Ti:sapphire laser operating at 800 nm wavelength, serving as the seed beam in the amplification system; (b) Quanta-Ray Nd:YAG laser, the pumping laser in the system; (c) Pulse stretcher and 8-pass pre amplification stages; (d) 4-pass power amplification stage; (e) Two-grating based pulse compressor.. ....	70
3.22. Layout of the pulse stretcher and the eight-pass preamplifier stage. (a), (b) and (c) dispersive grating, folding mirror and parabolic mirror of the pulse stretcher, respectively; (d) Pockel's cell serving as a pulse picker; (e) Ti:sapphire crystal in the eight-pass amplifier stage; (f) focusing mirrors for the pump beam.. ....	71

3.23. Layout of the pulse stretcher and the four-pass power amplification stage. (a), Ti:sapphire crystal in a thermal-electric cooling mount; (b) Beam splitter separating the pump beam so that the crystal is pumped from both sides; (c) Plano-convex lens slightly focusing the pumping beam. ....	72
4.1. Flow chart of the algorithm used in the numerical simulation.....	77
4.2. Intensity profile of the pulse at the target plane as a function of time and radius. The pulse front is curved due to the Propagation Time Delay (PTD) and broadened due to the Group Velocity Dispersion (GVD).. ....	79
4.3. Spatial profiles of the laser pulse at different times: (a) $t = 0$ , (b) $t = -0.1ps$ , and (c) $t = -0.35ps$ .....	80
4.4. (a) Peak intensity of the pulse front as a function of radius in the target plane, and (b) pulse duration time in the target plane as a function of radius.....	81
4.5. Fluence profile through the target plane as a function of radius.....	82
4.6. Fluence profile when the input beam is off-center by 10%.....	82
4.7. Effects of input beam size 10% larger (a) or smaller (b) than the designed value, respectively.....	83
4.8. Defocusing effects: (a) before and (b) after the focusing plane of the Fourier lens by 2.5% of the focusing length.. ....	84
4.9. Intensity profiles as function of radius and local time at the target plane. The laser pulse duration is 100 fs, and the peak power in each figure is a) $1.5 \times 10^{11} W/cm^2$ , b) $5 \times 10^{11} W/cm^2$ , c) $2.5 \times 10^{12} W/cm^2$ and d) $5 \times 10^{12} W/cm^2$ ...	85
4.10. Integrated fluence in the target plane. The pulse duration is 100 fs, and the beam diameter is 10 mm. The pulse peak intensity is: a) $1.5 \times 10^{11} W/cm^2$ , b) $5 \times 10^{11} W/cm^2$ , c) $2.5 \times 10^{12} W/cm^2$ , and d) $5 \times 10^{12} W/cm^2$ .....	86
4.11. (a) Input laser beam with a Gaussian profile, (b) output beam with a flat-top profile.....	88
4.12. Normalized energy-fluence profile along the central axis of the target plane. The theoretical result is plotted as solid curves, and the two sets of experimental data are plotted as filled squares and triangle.....	90

- 4.13. Effect of lateral misalignment of 10% of the laser beam diameter. The theoretical result is plotted as solid curves, and the two sets of experimental data are plotted as filled squares and triangles.. ..... 91
- 4.14. Effects of beam size deviation. (a) input beam size 10% larger than the designed value, (b) input beam size 10% smaller than the designed value. The theoretical result is plotted as solid curves, and the two sets of experimental data are plotted as filled squares and triangles.....92
- 4.15. Defocusing effects. (a) intensity profile before the focusing plane of the Fourier lens by 2.5% of the focal length, (b) intensity profile after the focusing plane of the Fourier lens by 2.5% of the focal length, The theoretical result is plotted as solid curves, and the two sets of experimental data are plotted as filled squares and triangles.....93
- 4.16. Fluence profile along the central axis of the target plane for a 1-mJ, 80-fs laser pulse passing through the beam shaping system. The theoretical result is plotted as solid curves, and the two sets of experimental data are plotted as filled squares and triangles..... 94
- 4.17. Fluence profile along the central axis of the target plane for a 20-mJ, 70-fs laser pulse passing through the beam shaping system. The theoretical result is plotted as solid curves, and the two sets of experimental data are plotted as filled squares and triangles..... 95



# Chapter 1

## Introduction

Beam shaping technology has been studied for decades. In 1965, Frieden[1] discussed the lossless conversion of a single-mode Gaussian beam into a plane wave of uniform irradiance. This is the first known study of lossless beam shaping problems. Kreuzer[2] patented a coherent light optical beam shaping system yielding an output beam of an arbitrary desired intensity[3] in 1969. After the earlier work of Frieden and Kreuzer, various optical beam shaping systems were developed to reshape the irradiance profile of a laser beam. Reflective beam shaping approach was studied by Herriott[4] and McDermit[5] using geometric optics methods. Rhodes and Shealy [6] developed a set of equations defining the surface shapes of two plano-aspherical lenses that redistribute a plane wave into a homogeneous intensity distribution. During the past decade, laser beam shaping technology has been widely used in many fields such as micromachining, optical lithography, material processing, optical data processing, medical procedures and many other applications.

A normal Gaussian laser beam can be reshaped into an arbitrary spatial profile depending on the beam shaping system. In many scientific and technical applications, a flat-top irradiance profile is especially preferred over other spatial profiles[7-9]. For example, in a holographic recording system[10] a top-hat laser beam can increase the

recording efficiency significantly. Kley[11] has tested a holographic system for a more efficient hologram recording which can be used for full color application. The essential part in the setup is a refractive beam shaping element to convert a Gaussian beam into a homogeneous irradiance profile. Another example of the application of top-hat laser beam is in the Z-scan measurement technique[12-14]. The sensitivity of Z-scan measurements can be increased by a factor of 2.5 by using a top-hat beam in the measurement compared to the usage of a regular Gaussian beam [15]. Using a relay-imaged top-hat Z-scan technique[16] can further improve the measurement by eliminating diffraction fringes and therefore minimize spurious effects such as varying interference fringes.

Current studies of top-hat laser beam shaping, however, have always focused on continuous wave (CW) lasers. Beam shaping of ultrashort laser pulses (subpicosecond pulses) is also very important because of the many advantages of short-pulse treatment in micromachining technology[17]. For example, in a hole-drilling process, the use of ultrashort pulses can minimize the heat-affected zone (owing to each pulse's short duration time) without influencing the overall efficiency which is determined by the total energy of the pulse train.

A beam shaping system can use various types of optical components, e.g., reflective mirrors, refractive optics or diffractive elements including optical diffusers and beam integrators, to control the propagation properties of a laser beam, i.e. the irradiance distribution at a certain aperture and the phase profile of the beam at that position. By changing the laser beam's propagation properties, a beam shaping system reshapes a normal Gaussian laser beam into a desired spatial intensity profile. The goal of this thesis

is to study both theoretically and experimentally the reshaping of ultrashort laser pulses into a flat-top beam profile.

### 1.1 Field mapping laser beam shaping techniques

A trivial method to generate a top-hat beam profile is to aperture an expanded Gaussian beam (shown in Figure 1.1). The achieved flatness of the beam is at the price of the energy loss after the aperture.

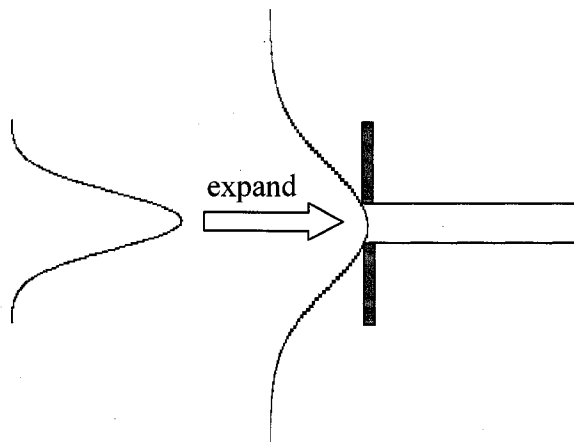


Figure 1.1. Aperture method to obtain a nearly flat intensity distribution.

Due to the disadvantage of energy loss, this method has very limited applications. It also creates diffraction rings which are a problem for some applications. Lossless beam shaping can be achieved with various optical approaches.

#### 1.1.1 Reflective beam shaping system

A reflective beam shaping system usually consists of one or two aspherical mirrors[18] or even deformable mirrors to convert a Gaussian beam into a uniform distribution. The surface profile of the reflector(s) can be determined with geometrical optics. Ray-tracing method is an efficient way to simulate the beam shaping problem. The process of ray-trace formulation is to develop a set of

differential equations expressing the law of reflection, conservation of energy and the condition of constant optical path length. McDermit and Horton[19] have developed the general ray-trace equations for the configuration shown in Figure 1.2.

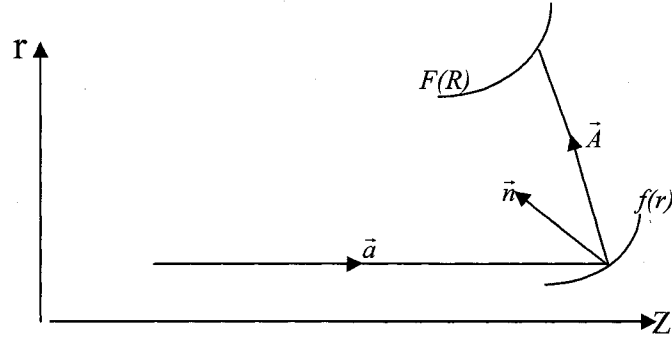


Figure 1.2. One-mirror beam shaping system,  $f(r)$  is the mirror surface, and  $F(R)$  is the receiver surface[20].

The geometrical configuration of the axis symmetric beam shaping system can be put into a  $r$ - $z$  plane coordinate system. In the configuration shown in Figure 1.2,  $f(r)$  is the mirror surface, and  $F(R)$  is the receiver surface.  $\vec{a}$  and  $\vec{A}$  are unit vectors of the incident beam and the reflected beam, respectively.  $\vec{n}$  is the unit vector along the normal to the mirror surface at the point of reflection. The law of reflection requires:

$$\vec{A} = \vec{a} - 2\vec{n}(\vec{a} \cdot \vec{n}) \quad (1.1)$$

Let the incident beam propagate along the optical axis which coincides with the  $Z$  axis. Therefore,  $\vec{a} = \vec{k}$ , where  $\vec{k}$  is the unit vector of the  $Z$  axis. The unit vector of the normal to the surface  $f(r)$  can also be expressed as the function of the derivative of the surface profile:  $\vec{n} = \frac{1}{\sqrt{1+(f')^2}}(-f'\vec{r} + \vec{k})$ , where  $\vec{r}$  is the unit vector along the  $r$  axis. Insert the explicit expressions of  $\vec{a}$  and  $\vec{n}$  into Eq. (1.1), the unit vector along the reflection beam can be rewritten as:

$$\vec{A} = \frac{2f' \vec{r} - (1 - f'^2) \vec{k}}{(1 + f'^2)} \quad (1.2)$$

This unit vector  $\vec{A}$  can connect the reflecting surface and the receiving surface in the following equation:

$$\frac{A_x}{A_z} = \frac{2f'(r)}{-[1 - f'^2(r)]} = \frac{R - r}{F(R) - f(r)} \quad (1.3)$$

Eq. (1.3) describe the trace of one ray in the beam. As far as the ray bundle between any two surfaces intersecting the beam is concerned, the condition of energy conservation gives:

$$I_1(r) 2\pi r dr = I_2(R) 2\pi R [dR^2 + dF^2]^{1/2} \quad (1.4)$$

where  $I_1(r)$  is the intensity profile of the beam incident on the mirror surface, and  $I_2(R)$  is that of the beam on the receiver surface. In most cases,  $I_1(r)$  represents a Gaussian laser beam profile.

Differentiating Eq. (1.3) with respect to  $r$  and incorporating the resulting equation into Eq. (1.4) gives :

$$\frac{f''}{f'} = \frac{1}{R - r} \left\{ \frac{I_1(r)}{I_2(R)} \frac{r}{R} \frac{\frac{dR}{dF} \frac{1 - f'^2}{1 + f'^2} + \frac{2f'}{1 + f'^2}}{\sqrt{1 + \left(\frac{dR}{dF}\right)^2}} - 1 \right\} \quad (1.5)$$

Eq. (1.5) gives the general ray tracing formula connecting the incident intensity profile  $I_1(r)$  with the output beam profile  $I_2(R)$  through the reflecting surface function  $f(r)$ . Solving this differential equation will yield the surface profile of the mirror. Similar procedures can be performed to obtain the ray tracing equation for a two-mirror beam shaping system. Several specific solutions to Eq. (1.5) for a given source irradiation distribution and a desired receiver irradiation profile have been analyzed by McDermit and Horton[12][13]. For example, the reflective surface in a one-mirror beam shaping

system converting a cosine beam  $I(r) = \cos \frac{\pi r}{2}$  into a uniform receiver irradiation distribution is solved to have a profile shown in Figure 1.3.

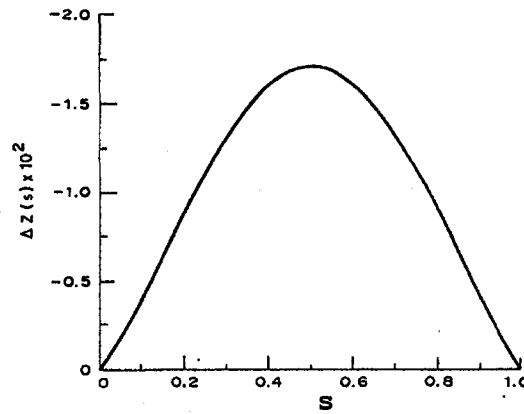


Figure 1.3. Reflective surface in a one-mirror beam shaping system converting a cosine beam into a homogeneous intensity distribution[19].

### 1.1.2 Refractive beam shaping system

A reflective beam shaping system, however, has to be used off axis in order to avoid any blockage in alignment. For a rotationally symmetric beam, a refractive beam shaping approach[20-24] is more convenient for a coaxial optical arrangement. Rhodes and Shealy[22] have developed the equations for a two-lens beam shaping system with an output of a top-hat beam profile. Ray-tracing method is used again to formulate the equations.

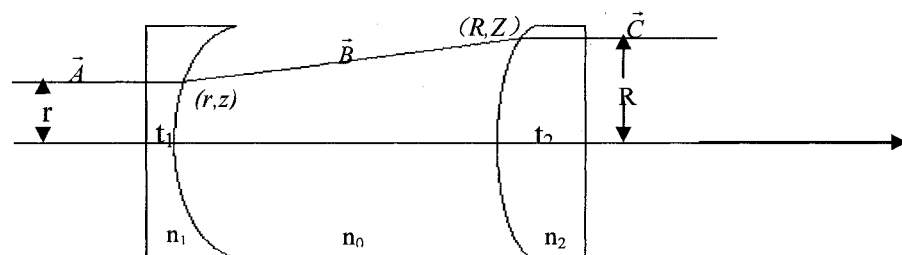


Figure 1.4. A two-lens beam shaping system converting a laser beam into a uniform intensity distribution[22].

Consider a two-lens optical configuration as shown in Figure 1.4. Let the incident intensity profile of the incident beam and the output beam be  $f(r)$  and  $F(r)$ , respectively.

The law of energy conservation requires:

$$\int_0^{2\pi} \int_0^{r_0} f(r) r dr d\theta = \int_0^{2\pi} \int_0^{R_0} F(r) r dr d\theta, \quad (1.6)$$

where  $r_0$  and  $R_0$  are the radius of incident and output beam, respectively. Since the output intensity is constant over the cross section of the beam, the right side of Eq. (1.6) equals  $\pi F R_0^2$ . Given the constant  $F$ , the radius of the output ray can be expressed as a function of the radius of the incident beam:

$$R = \left[ \frac{2}{F} \int_0^r f(x) x dx \right]^{\frac{1}{2}}. \quad (1.7)$$

According to Snell's law, the unit vector along the refracted rays is given by:

$$\vec{B} = \gamma \vec{A} + \Omega \vec{n}, \quad (1.8)$$

where  $\gamma = \frac{n_1}{n_0}$ ,  $\vec{A} = \vec{k}$ ,  $\Omega = \frac{-\gamma + [1 + z'^2 (1 - \gamma^2)]^{\frac{1}{2}}}{(1 + z'^2)^{\frac{1}{2}}}$ ,  $\vec{n} = \frac{-z' \vec{i} + \vec{k}}{(1 + z'^2)^{\frac{1}{2}}}$ ,  $z' = \frac{dz(r)}{dr}$ , and  $\vec{i}$  and  $\vec{k}$  are the

unit vectors along x axis and z axis, respectively.

The unit vector  $\vec{B}$  connects the surface profiles of the first and the second lenses with the following relation:

$$\frac{R - r}{Z - z} = \frac{B_x}{B_z}, \quad (1.9)$$

where  $(r, z)$  and  $(R, Z)$  are the starting and the ending points of the ray transferred from the surface of the first lens to that of the second lens.

Combining Eq. (1.8) and Eq. (1.9) gives:

$$z'^4 [\gamma^2 (R-r)^2 + (\gamma^2 - 1)(Z-z)^2] + z'^3 [-2(R-r)(Z-z)] + z'^2 \{-(1-\gamma^2)[(R-r)^2 + (Z-z)^2]\} + z'[-2(R-r)(Z-z)] + (R-r)^2 = 0. \quad (1.10)$$

If the incident beam is a plane wave, then in order to retain the same wave front when the beam passes through the beam shaping system, all rays must have the same optical path length as that of the central ray  $L_{central} = n_1 t + (Z_0 - t)n_0 + n_2 T$ . The optical path length for an arbitrary ray is given by:

$$L = n_1 z + n_0 [(R-r)^2 + (Z-z)^2]^{\frac{1}{2}} + n_2 [Z_0 + T - Z]. \quad (1.11)$$

Therefore, the constant optical path length condition requires:

$$n_1 z + n_0 [(R-r)^2 + (Z-z)^2]^{\frac{1}{2}} + n_2 [Z_0 + T - Z] = n_1 t + (Z_0 - t)n_0 + n_2 T \quad (1.12)$$

Apply Snell's law for the refracted ray  $\vec{C}$  in the same way as performed to obtain Eq. (1.10), the ray-tracing equation including  $Z'(R)$  can be given by:

$$Z' = \frac{\gamma_2 z' \{\gamma - [1 + z'^2 (1 - \gamma^2)]^{\frac{1}{2}}\}}{1 + z'^2 - \gamma_2 \gamma z'^2 - \gamma_2 [1 + z'^2 (1 - \gamma^2)]^{\frac{1}{2}}}. \quad (1.13)$$

For a specific beam shaping problem, the solution to the surface profiles of the lenses can be obtained in the following procedure: (1) given the incident beam profile  $f(r)$ , one can solve the energy conservation equation (Eq. 1.7) to get  $R(r)$ ; (2) the constant optical path length equation (Eq. 1.12) yields  $Z(z)$ ; (3) inserting these results into the ray tracing equation for ray  $\vec{B}$  (Eq. 1.10), the slope of the first surface  $z'(r)$  can be obtained. This result usually needs numerical calculation; (4) finally, from the result obtained in step (3), the slope of the second surface  $Z'(R)$  can also be obtained by solving the ray tracing equation for ray  $\vec{C}$  (Eq. 1.13).

For such a refractive laser beam shaping system converting a Gaussian laser beam into a homogeneous intensity distribution, Shealy[22] has solved the above equations numerically and obtained the surface profiles of the aspherical lens shown in Figure 1.5.

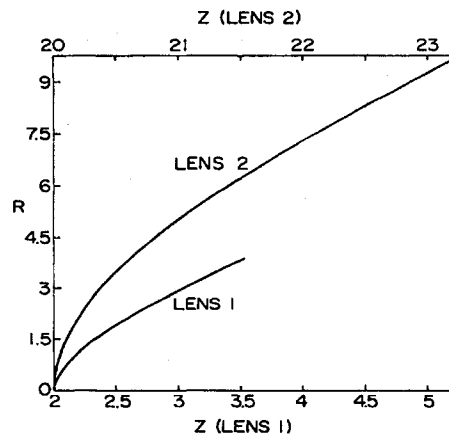


Figure 1.5. Surface profiles of aspherical lenses in a refractive beam shaping system converting a Gaussian beam into a uniform intensity distribution[22].

It is very convenient to simulate reflective or refractive beam shaping systems with ray-tracing technique. Interference or diffraction effects are not included in the analysis. However, in practical applications, fabrication of such plano-aspherical lenses is not easy. Another way to obtain the same refraction but with spherical lenses is to make use of gradient-index glass materials. It has been demonstrated that the contributions of an axial gradient-index glass to the third-order aberrations are equivalent to those of an aspherical surface[25]. Therefore, it can be used to control the spherical aberration with equivalent effects as obtained by using aspherical lenses. Wang has designed a three-element gradient-index glass beam shaping system[26].

### 1.1.3 Diffractive beam shaping system

Diffraction-based method is the most frequently used beam shaping approach. A diffractive beam shaping system consists of a phase element and a transform element. Similar to those in the refractive beam shaping system, the phase element can be an aspherical lens. But it is different from a refractive beam shaping element in that the diffraction-based design introduces a phase delay scaling parameter  $\beta = \frac{2\pi r_i R_o}{f\lambda}$ , where  $r_i$  and  $R_o$  are the radii of the incident and the desired output beam, respectively. This scaling parameter will affect the output top-hat beam quality. Moreover, different optical parameters can share the same phase delay function as long as the combined values of  $\beta$  for the two sets of parameters are the same. This feature makes the diffraction-based design more flexible for different optical parameters.

A typical diffractive beam shaping system is shown in Figure 1.6. The transform element in the figure can be a spherical lens which provides a Fourier transform relation between the input and output beam.

Dickey[27] studied a beam shaping system as shown in Figure 1.6 using Fourier optics. The beam shaping problem is defined as finding a certain phase delay function so that the wave front of a beam is curved due to the phase modulation and thus the energy within the beam will be redistributed to a given profile as traveling to the target plane of the beam shaping system.

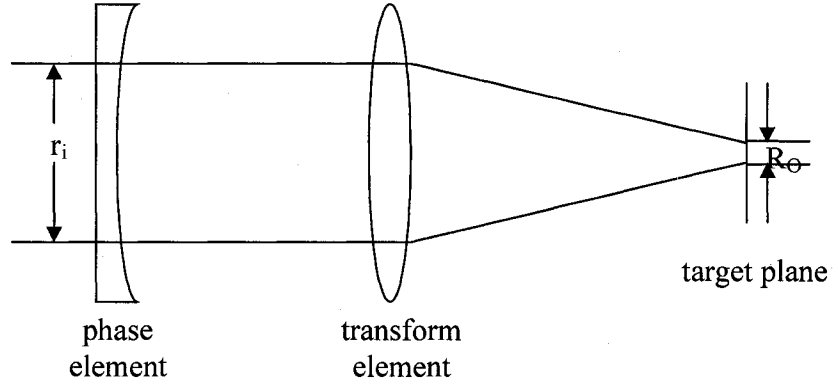


Figure 1.6. A typical diffractive beam shaping system consisting of a phase element and a transform element. The target plane is at the focal plane of the transform element[27].

Let  $E_0 g(x/r_i, y/r_i)$  be the incident field, where  $r_i$  is the beam radius.  $U_l(x, y)$  is the field distribution after the phase delay element, i.e. the input field to the Fourier lens with focal length  $f$ . Therefore,

$$U_l(x, y) = E_0 g(x/r_i, y/r_i) \exp[i\beta\phi(x/r_i, y/r_i)] \quad , \quad (1.14)$$

where  $\beta\phi(x/r_i, y/r_i)$  is the phase delay function caused by the phase element.

Using the wave theory of light, the field distribution at the focal plane  $z = z_0$  can be given by the Fresnel approximation[28]:

$$U(x_f, y_f) = \exp(i\psi_0) \frac{1}{i\lambda z_0} \int_{-\infty}^{\infty} \int_{-\infty}^{\infty} U_l(x, y) \exp\left\{-i\frac{2\pi}{\lambda z_0} [xx_f + yy_f + \frac{1}{2}(\frac{z_0}{f} - 1)(x^2 + y^2)]\right\} dx dy, \quad (1.15)$$

where  $\psi_0 = \frac{\pi}{\lambda z_0} (x_f^2 + y_f^2 + 2z_0^2)$  is a constant phase factor,  $x_f$  and  $y_f$  are the coordinates in the plane  $z = z_0$ .

Inserting Eq. (1.14) into Eq. (1.15), and after arrangement, the output field distribution at the focal plane of the Fourier lens can be rewritten as:

$$U(\omega_x, \omega_y) = \frac{E_0 \exp(i\psi_0) r_i^2}{i\lambda z_0} \int_{-\infty}^{\infty} \int_{-\infty}^{\infty} g(\xi, \eta) \exp\{i[\beta\phi(\xi, \eta) - \xi\omega_x - \eta\omega_y]\} d\xi d\eta, \quad (1.16)$$

where  $\omega_x = x_f / R_o$  and  $\omega_y = y_f / R_o$  are the normalized radius in the target plane.

Given an incident field  $g(\xi, \eta)$  and the desired output field  $U(\omega_x, \omega_y)$ , the phase delay function can be obtained by solving Eq. (1.16). Dickey solved the Equation for a beam shaping system converting a Gaussian beam into a top-hat profile, and the resulting phase delay function is given by[27]:

$$\phi(\xi) = \frac{\sqrt{\pi}}{2} \xi \operatorname{erf}(\xi) + \frac{1}{2} \exp(-\xi^2) - \frac{1}{2}. \quad (1.17)$$

Here the phase delay function is a one-dimensional function because Eq. (1.16) is a separable problem. The phase delay function (1.17) is plotted in Figure 1.7. Hoffnagle[29] gives a new derivation of the above phase function using paraxial approximation, and obtains the identical phase function as expressed in Eq. (1.26). The identity demonstrates the equivalence, in the paraxial limit, of two different methods of solving the beam shaping problem.

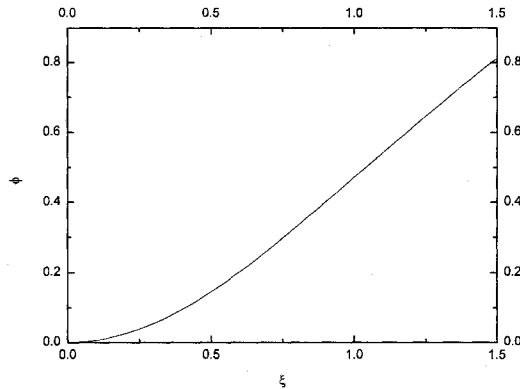


Figure 1.7 Phase delay function  $\phi(\xi)$  that turns a Gaussian beam into a top-hat profile[27].

## 1.2 Beam integration techniques

Besides the field mapping beam shaping approaches, another major class of beam shaping techniques is beam integration method. This category includes two major

techniques: multi-aperture beam integrators and diffractive beam diffusers. The latter technique can be viewed as a more general case of the former one.

### 1.2.1 Multi-aperture beam integration approach

Geometrical optical methods can be applied in solving beam shaping problems in which the mode of the incident beam is well defined, such as a  $TEM_{00}$  mode of a Gaussian irradiance profile. When the incident beam has a multi-mode intensity distribution, the calculations based on geometrical optics as discussed in the previous section would be much more complicated. In such cases, a multi-aperture beam integration approach is more desired. Brown [30] has patented a multi-aperture beam integrator producing a continuously variable complex image.

A diffracting multi-aperture beam integrator is illustrated in Figure 1.8. This beam shaping system consists of a subaperture array component and a primary lens which overlaps the beamlets from each subaperture.

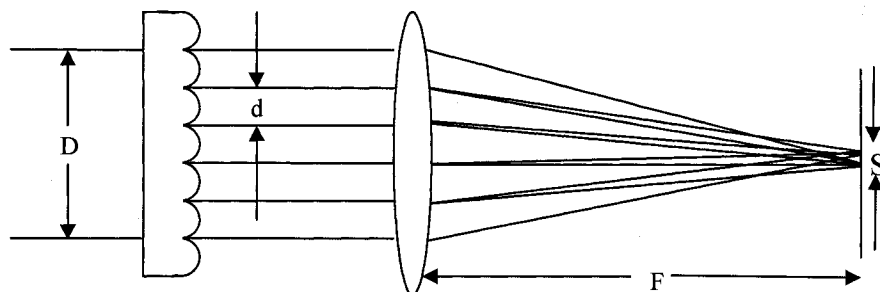


Figure 1.8. A diffracting multi-aperture beam integration system[17].

The incident beam with diameter  $D$  is segmented by the lenslet arrays into an array of beamlets. In the target plane which is located at the focal plane of the primary focusing lens, the total amplitude of the output beam is a Fourier transform of the beamlets generated by the subapertures. Assuming the amplitude of the beam is uniform

over each subaperture, and each beamlet has a uniform phase front, that is, the beam is spatially coherent over each lenslet aperture, the target spot will have an approximate flat-top intensity as long as the number of the subapertures is large enough.

The  $f$ -number of the subaperture lens is defined as  $\frac{f}{d}$ , where  $f$  is the focal length of each subaperture lens, and  $d$  the diameter of the subaperture. Using Paraxial geometrical optics, one can obtain the following relationship between the target spot size  $S$ , the focal length of the primary lens  $F$  and the  $f$ -number of each subaperture lens:

$$S = \frac{F}{f/d}. \quad (1.18)$$

This relationship can be used to determine the geometrical configuration of the beam shaping system[31]. The number of the lenslets can be approximated by  $(\frac{D}{d})^2$ . Deng[31] has performed experimental study for uniform illumination of large targets using a lens array. Figure 1.9 shows the effect of the multi-aperture beam integration system.

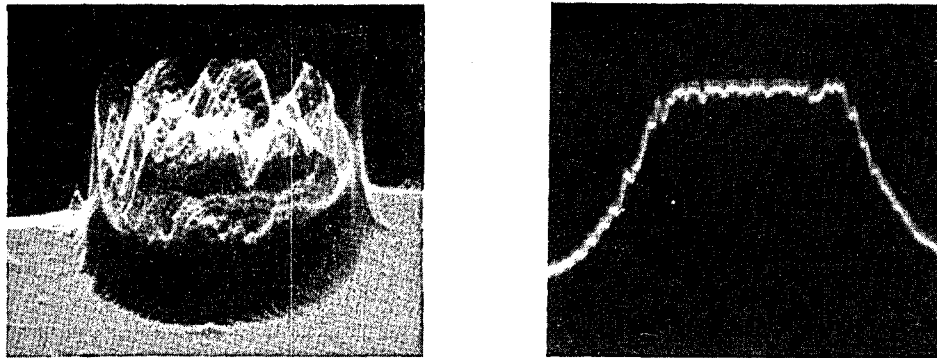


Figure 1.9. Effect of a multi-aperture beam integration system: (a) two-dimensional intensity distribution on the target without the lenslet array, and (b) one-dimensional intensity distribution in the target plane with the lenslet array[31].

Since the beam source is coherent, the interference effect needs to be considered. The field at the target plane is given by the sum of the coherent diffraction from each subaperture :

$$E(x, y) = \sum_{0,0}^{M,N} [A_{mn} \exp(i(k(\alpha_m x + \beta_n y) + \theta_{mn}))] F(x, y) \quad , \quad (1.19)$$

where  $A_{mn}$  is the amplitude of the beamlet field,  $\alpha_m$  and  $\beta_n$  are the direction cosines of an arbitrary beamlet,  $\theta_{mn}$  is the phase of the beamlet, and  $F(x, y)$  is the Fourier transform of the aperture function. The spatial period of the interference pattern is given by  $\frac{\lambda}{\alpha}$ , where  $\alpha$  is the angle between adjacent beamlets. In order to make the interference pattern fine enough so that it can be neglected in the application, the value of  $\alpha$  must be sufficiently large. When this condition is met, the intensity distribution in the target plane can be approximated as:

$$I(x, y) = \sum_{0,0}^{M,N} |A_{mn}|^2 |F(x, y)|^2 \quad . \quad (1.20)$$

The subaperture array can also be reflective, Dickey and O'Neil has studied a multi-faceted reflective beam integration system[32].

### 1.2.2 Band limited optical diffuser beam shaping technique

Band-limited optical diffuser beam shaping technique is a far field beam shaping method. This approach has the advantage of being insensitive to the shape and alignment of the input beam, and therefore has wide application in systems where the input beam quality or the alignment of the optical system is not sufficient for other beam shaping techniques. Tommasini[33] applied the Yang-Gu algorithm[34][35] for phase-amplitude

retrieval to the general problem of beam shaping through amplitude masks. Brown[36] discussed in detail about the design of binary diffusers used for beam shaping purpose.

A diffractive diffuser works in this way: it introduces a spatial structure to the phase front of a laser beam. As the beam propagates, the interference within the beam caused by the spatial frequencies in the phase will result in a redistribution of the energy in the beam. The spatial pattern of the diffuser determines the final irradiance profile in the target plane.

Brown[36] has demonstrated that the field of a traveling optical wave at a distance from the diffuser is simply the convolution of the spatial frequency structure of the phase and the amplitude of the beam propagating the same distance. The procedure of designing a diffractive diffuser is as following:

- (1) Randomize the desired intensity distribution by multiplying the intensity profile by a random function.

- (2) Perform inverse Fast Fourier transform (FFT) on the randomized intensity profile function obtained in setp (1).

- (3) Truncate the phase of the inverse transform function to obtain a binary phase function.

- (4) Obtain the binary pattern of the phase structure in the diffractive diffuser.

- (5) Use scalar wave theory to simulate the intensity of the beam propagating to the target plane.

A diffractive diffuser beam shaping element converting a Gaussian beam into a ring of laser light can be designed following the above procedure[36]. The binary phase structure for the ring diffuser is shown in Figure 1.10. This pattern resulted from a high-

frequency randomization of the desired amplitude function. It is the randomization process that provides the system with the advantage of being insensitive to the alignment and the input beam quality.

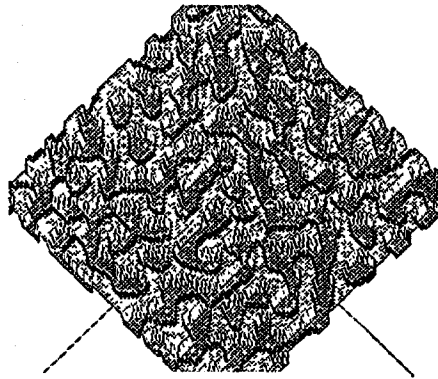


Figure 1.10 Binary phase structure of a diffractive diffuser converting a Gaussian laser beam into a ring shape[36].

With scalar wave theory, the intensity distribution at the target plane can be simulated for the transmitted beam through this diffractive diffuser. Figure 1.11 shows the simulation of the irradiance profile at the target plane of the ring diffuser beam shaping system.

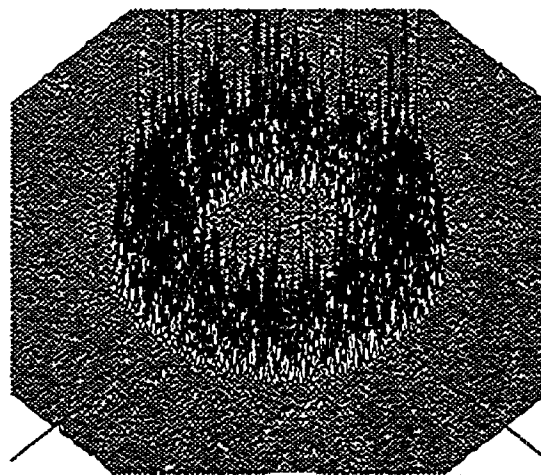


Figure 1.11. Intensity profile at the target plane of the ring diffuser[36].

A lot of speckles can be seen in the output ring pattern shown in Figure 1.8. These speckles originate from the interference of the coherent beam. Discussion on the speckles can be found in Refs 37 and 38. This speckle characteristic of diffusers is the major drawback of diffractive diffusers used in the beam shaping technology.

### **1.3 Scope of this dissertation**

In the course of this dissertation, I performed theoretical and experimental studies on the spatial beam shaping of high-power ultrashort laser pulses passing through a diffractive irradiance redistribution system.

Theoretical simulation of pulsed laser beam shaping: spatial beam shaping study is extended to the regime of high-power ultrashort laser pulses. A theoretical model describing the spatio-temporal evolution of a femtosecond pulse propagating through a diffractive beam shaping system is developed. Numerical simulation shows that the Gaussian-flattop beam shaping system originally developed for Continuous Wave laser beams can work well with ultrashort laser pulses when the pulse energy is relatively low (<10 mJ). At higher energy levels, however, when the nonlinear self phase modulation effect is taken into account, the top-hat profile is gradually degraded until diffraction rings appear at extremely high energy level (~100 mJ).

Terawatt laser amplification system: a Chirped Pulse Amplification (CPA) laser amplifier system has been built up. The output pulse energy reaches 20 mJ with a pulse width of 73 fs. This brings the peak power of the pulse into the terawatt range. The amplifier system is seeded by a 80-MHz, 450-mW Ti:Sapphire laser, and pumped by a 30-Hz, 24-W Nd:YAG laser. It consists of a reflective one-grating pulse stretcher, an

eight-pass preamplifier, a four-pass power amplifier and a two-grating hybrid pulse compressor.

Experimental study of ultrashort laser pulse beam shaping: Experimental verification of the theoretical simulation is performed at various energy levels using the beam generated from the CPA laser amplifier system. Output spatial intensity profiles are captured. The intensity profiles are fitted with the results obtained in the numerical simulation. Experimental results show good agreement with the theoretical calculation.

## **Chapter 2**

### **Beam Shaping System**

This chapter describes an optical beam shaping system which uses diffractive optical elements to reshape the Gaussian beam profile into a flat-top distribution. A theoretical model is developed for high-power ultrashort laser pulses passing through the beam shaping system. Section 2.1 gives a brief introduction to the theory of wave propagation and diffraction, especially the Stationary Phase approximation and the Fresnel propagation approximation, which are necessary for the modeling of the beam shaping system. The mathematical model is presented in section 2.2. The case of high-power laser pulse input is also considered in the theoretical model. Section 2.3 describes various nonlinear optical effects and their significance in an optical system. The Self Phase Modulation effect is the most important nonlinear optical effect and it is therefore included in the theoretical model. The diffraction integral including self Phase Modulation effect is discussed in section 2.3.

Next, the experimental setup of the beam shaping system is described in section 2.4. This section shows the optical layout of the beam shaping system. Fabrication of the phase delay element is first discussed since it is the core element in the beam shaping

system. The beam size control and beam diagnostic system are described following the discussion of the phase delay element fabrication.

## 2.1 Theory of wave propagation and diffraction

The process of wave propagation and diffraction can be described by the Rayleigh-Sommerfeld diffraction integral. The amplitude of a wave  $U_A$  at an observation point  $A(x_A, y_A, z_A)$  (see Figure 2.1) is given by[39]:

$$U_A(x_A, y_A, z_A) = \int U_0(x, y, 0) P(x_A - x, y_A - y, z_A) dx dy, \quad (2.1)$$

where  $P(x_A - x, y_A - y, z_A) = -\frac{1}{2\pi} \frac{\partial}{\partial z_A} \left( \frac{\exp ikr}{r} \right)$ , and  $r = [(x_A - x)^2 + (y_A - y)^2 + z_A^2]^{\frac{1}{2}}$  is

the distance between the observation point A and an arbitrary point  $(x, y, 0)$  in the aperture plane. Function  $P(x_A - x, y_A - y, z_A)$  is called a propagator. When  $r$  is sufficiently large,  $P(x_A - x, y_A - y, z_A)$  can be approximated in several different ways. The Fraunhofer approximation[40] and the Fresnel approximation[41] are the most frequently used approximations. In our beam shaping system, the Fresnel approximation is used to describe the beam propagation in free space. This will be further discussed in the following section.

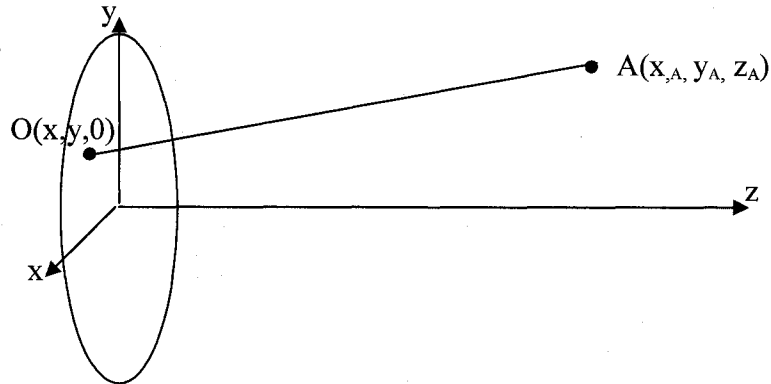


Figure 2.1. Geometry for the Rayleigh-Sommerfeld diffraction integral.  $A(x_A, y_A, z_A)$  is the observation point, and  $O(x, y, 0)$  is a secondary wave source in the aperture plane.

Diffraction integrals always have the form  $I(x) = \int f(t) \cdot \exp(i\psi(t) \cdot x) dx$  which we call “Generalized Fourier Integrals”. As  $x \rightarrow \infty$ , the exponential term in the integral will be a fast oscillating function. If the variation of function  $f(x)$  is much smaller than that of the exponential function, we can use the Stationary Phase Method[42] to evaluate the diffraction integral with greatly reduced computation load. As an asymptotic method, the stationary phase approximation is a very important technique in the theory of wave propagation and diffraction.

### 2.1.1 Fresnel Approximation

According to Huygen’s principle, each point  $(x, y, 0)$  in the aperture plane may be considered as the source of a secondary wave, and the sum of all these secondary waves gives the diffracted field at a target point. The contribution of each source point can be expressed by a point spread function as shown in Equation (2.1). For an observation point  $A(x_A, y_A, z_A)$  far away from the light source, the radiation pattern of the propagator  $P(x_A - x, y_A - y, z_A) = -\frac{1}{2\pi} \frac{\partial}{\partial z_A} \left( \frac{\exp ikr}{r} \right)$  can be approximated in different ways depending on the far field condition. then the propagator can be rewritten as[41]:

$$P(x_A - x, y_A - y, z_A) = -\frac{1}{2\pi} \frac{\partial}{\partial z_A} \left( \frac{\exp ikr}{r} \right) = -\frac{z_A}{2\pi} \left( \frac{ik}{r^2} - \frac{1}{r^3} \right) \exp(ikr). \quad (2.2)$$

In a moderately stringent condition, the distance  $r = z_A \sqrt{1 + \frac{(x_A - x)^2 + (y_A - y)^2}{z_A^2}}$  can

be replaced by its Taylor series, truncated after the quadratic terms:

$$r \approx z_A + \frac{(x_A - x)^2 + (y_A - y)^2}{2z_A} - \frac{[(x_A - x)^2 + (y_A - y)^2]^2}{8z_A^3}. \quad (2.3)$$

After inserting Equation(2.3) into Equation(2.2), the propagator becomes:

$$P(x_A - x, y_A - y, z_A) = \frac{1}{i\lambda z_A} \exp(ikz_A) \exp(ik \frac{(x_A - x)^2 + (y_A - y)^2}{z_A}). \quad (2.4)$$

This approximation is referred to as the Fresnel approximation. Another way of reaching the same result is to use the small angle approximation, that is, the angle of the observation point with respect to the optical axis is relatively small. Using the angular spectrum of the field, we can obtain exactly the same expression as Equation (2.4).

### 2.1.2 Stationary Phase Approximation

For an integral of the form  $I(x) = \int f(t) \cdot \exp(i\psi(t) \cdot x) dt$ , where the phase function  $\exp(i\psi(t) \cdot x)$  is fast oscillating, small changes in  $\psi(t)$  will lead to a full cycle of oscillation. If the amplitude function  $f(t)$  is relatively smooth, the contribution of the integrand over these regions is essentially zero to the value of the integral. However, if  $\psi'(t)$  vanishes at some points where  $\exp(i\psi(t) \cdot x)$  oscillates less rapidly, the contribution of the integrand near these regions to the value of  $I(x)$  will be nonzero. These stationary points give dominant contributions to the integral.

If  $t = t_0$  is a stationary point, the function  $\psi(t)$  can be expanded into a Taylor series around this point, and the series can be truncated after the second order term:

$$\psi(t) = \psi(t_0) - \frac{1}{2}(t - t_0)^2 \psi''(t_0). \quad (2.5)$$

After inserting Equation (2.5) into the integral,  $I(x)$  can be approximated as:

$$I(x) \approx f(t_0) \exp(i\psi(t_0) \cdot x) \int \exp(i \frac{1}{2} \psi''(t_0) (t - t_0)^2 \cdot x) dt, \quad (2.6)$$

where  $f(t_0)$  is moved out of the integral since the dominant contribution comes from a region very near to the stationary point  $t_0$ , and therefore the value of  $f(t)$  is approximately constant.

With this approximation, the integral can be solved analytically as[43]:

$$I(x) \approx f(t_0) \exp(i\psi(t_0) \cdot x) \exp(\pm \frac{i\pi}{4}) \sqrt{\frac{2\pi}{|\psi''(t_0)| \cdot x}} \quad , \quad (2.7)$$

where the sign in the second exponential function follows the sign of the second derivative of  $\psi(t)$ . This Stationary Phase approximation can be easily carried over to higher-dimensional integrals. In a two-dimensional integral, for example, the approximation gives:

$$I(x) \approx f(t_0, s_0) \exp(ix\psi(t_0, s_0)) \iint \exp(i\frac{1}{2} x \Psi''(t, s)) dt ds \quad , \quad (2.8)$$

where  $\Psi''(t, s) = \frac{\partial^2 \psi(t_0, s_0)}{\partial^2 t} (t-t_0)^2 + 2 \frac{\partial^2 \psi(t_0, s_0)}{\partial t \partial s} (t-t_0)(s-s_0) + \frac{\partial^2 \psi(t_0, s_0)}{\partial^2 s} (s-s_0)^2$  is the

Hessian of the function  $\psi(t, s)$ .

## 2. 2 Modeling of ultrashort pulse beam shaping

Among various laser beam shaping approaches, the diffractive beam shaping technique is the most widely used method. The schematic of a typical diffractive beam shaping system is shown in Figure 2.2. This system consists of a beam expander, a phase delay element and a Fourier lens. For a monochromatic wave, this beam shaping system works as follows: a laser beam is expanded to the desired input size by the telescope, then it passes through the phase delay element where the wave front of the laser beam is curved in an aspherical manner. After being focused by the Fourier lens, the laser beam can form an arbitrary intensity profile in the target plane depending on the wave front

pattern at the output of the phase delay element. In other words, given a desired output beam profile (top-hat profile, for example), one can find a specific phase delay function such that the intensity distribution in the target plane is the desired profile.

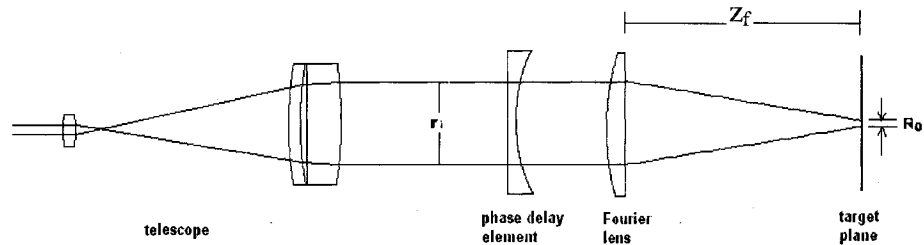


Figure 2.2. A typical diffractive beam shaping system

In the view of geometrical optics, the input beam consists of collimated rays with a transversal density of Gaussian distribution. When the rays encounter the phase delay element and the focusing lens, they will be bent to form a given irradiance distribution in the target plane. Figure 2.3 shows the Geometrical optics representation of the beam shaping process. In this figure the intensity profile in the target plane is a homogeneous distribution as an example.

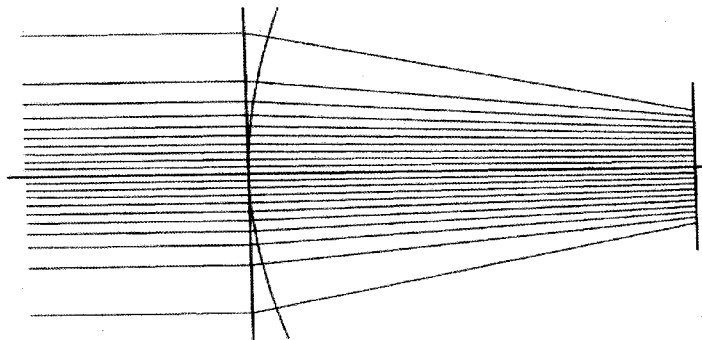


Figure 2.3. Geometrical optics representation of the beam shaping process[44]

The form of the phase delay function corresponding to a top-hat output profile can be deduced with this geometrical optical method.  $I_{in}(\xi)$  is the intensity of an incident beam with a radius  $r_i$ , where  $\xi$  is the normalized radius in the incident aperture.  $I_{out}(\alpha) \cdot A \frac{r_i^2}{R_0^2}$  is the intensity profile of the output beam with a radius  $R_0$ , where  $\alpha$  is the normalized radius in the target plane, and  $A \frac{r_i^2}{R_0^2}$  is a scaling constant. The phase delay function caused by the beam shaping element is given by  $\phi(\xi)$ . When an originally collimated ray encounters the optical element at position  $(\xi r_i, 0)$ , it will be bent and then propagates to the position  $(R_0 \alpha, f)$  in the target plane—the focal plane of the Fourier lens with a focal length of  $f$ . The conservation of energy requires:

$$\int_{\xi r_i}^{\infty} I_{in}(r/r_0) r dr = A \frac{r_i^2}{R_0^2} \int_{\alpha R_0}^{\infty} I_{out}(R/R_0) R dR. \quad (2.9)$$

After transformation of variables, this equation can be written as:

$$\int_{\xi}^{\infty} I_{in}(r) r dr = A \int_{\alpha(\xi)}^{\infty} I_{out}(R) R dR. \quad (2.10)$$

A differentiated form of the above equation is given by:

$$A \alpha I_{out}(\alpha) \frac{d\alpha}{d\xi} = \xi I_{in}(\xi). \quad (2.11)$$

For a beam shaping system to reshape a Gaussian beam into a top-hat profile,

$$I_{in}(\xi) = e^{-\xi^2} \text{ and } I_{out}(\alpha) = \begin{cases} 1 & \text{when } |\alpha| \leq 1 \\ 0 & \text{when } |\alpha| > 1 \end{cases}. \text{ Normalization of the energy requires } A = \frac{\sqrt{\pi}}{2}, \text{ and}$$

Equation (2.11) becomes:

$$\frac{d\alpha(\xi)}{d\xi} = \frac{2}{\sqrt{\pi}} \exp(-\xi^2). \quad (2.12)$$

The solution of this equation is  $\alpha(\xi) = \text{erf}(\xi)$ , where  $\text{erf}(\xi) = \frac{2}{\sqrt{\pi}} \int_0^\xi \exp(-x^2) dx$  is the error function. In geometrical optics, Fermat's principle requires that  $\frac{d\phi(\xi)}{d\xi} = \alpha(\xi)$ . Therefore, the phase delay function can be determined by solving the equation  $\frac{d\phi(\xi)}{d\xi} = \text{erf}(\xi)$ . The solution to this equation is given by[44]:

$$\phi(\xi) = \frac{\sqrt{\pi}}{2} \xi \text{erf}(\xi) + \frac{1}{2} \exp(-\xi^2) - \frac{1}{2}. \quad (2.13)$$

This phase delay function will curve the phase front of the beam in such a way that when the beam travels to the target plane, a top-hat intensity profile will be formed.  $\phi(\xi)$  is expressed as a function of the normalized radius  $\xi$  in the incident aperture. It can be multiplied by a scaling factor  $\beta = \frac{2\pi r_1 R_0}{f\lambda}$  without changing the property of the phase delay function. This scaling property allows the system with a phase delay function  $\beta\phi(\xi)$  to work for various optical parameters as long as the two sets of parameters have the same value of  $\beta$ , that is, the same phase delay function  $\beta\phi(\xi)$  can be used for a new beam shaping system with a desired output radius  $R_0'$  and focal length  $f'$  provided  $R_0'/f' = R_0/f$ .

In order to evaluate the spatio-temporal intensity distribution over the target plane of an ultrashort laser pulse passing through this diffractive beam shaping system, we trace each spectral component of the pulse. Each monochromatic component will experience a phase delay when traveling through the phase delay element and the Fourier lens. When they reach the target plane, the complex amplitude of all spectral components are

superpositioned using inverse Fourier transform. In this way, the spatio-temporal profile can be obtained.

The electric field of the incoming laser pulse can be written as:

$$E_{in}(r, t) = E_0 \exp\left(-\frac{r^2}{2r_i^2}\right) \exp\left(-\frac{t^2}{2\tau_i^2}\right) \exp(i\Omega_0 t), \quad (2.14)$$

where  $\exp\left(-\frac{r^2}{2r_i^2}\right)$  and  $\exp\left(-\frac{t^2}{2\tau_i^2}\right)$  are the spatial and the temporal Gaussian profile, respectively.  $2r_i$  is the Full Width at Half Maximum (FWHM) of the laser beam,  $2\tau_i$  is the pulse duration time and  $\Omega_0$  is the carrier frequency.

The Fourier transform of  $E_{in}(r, t)$  gives the frequency spectrum of this pulse:

$$\tilde{E}_{in}(r, \Omega) = F\{E_{in}(r, t)\} = E_0 \exp\left(-\frac{r^2}{2r_i^2}\right) \exp\left(-\left(\frac{\Omega - \Omega_0}{\delta}\right)^2\right), \quad (2.15)$$

where  $\delta$  is the band width of the spectrum. Therefore, at the target plane ( $z = z_f$ , shown in Figure 2.2), the complex field as a function of radius  $r_f$  for each frequency component is given by:

$$\tilde{E}(r_f, z_f, \Omega) = \iint \tilde{E}_{in}(r, \Omega) \cdot \exp[iT_{pd}(r, \Omega)] \cdot \exp\left(-ik \frac{r^2}{2f}\right) \cdot \frac{1}{i\lambda z_f} \exp(ikz_f) \exp\left[ik \frac{(r_f - r)^2}{2z_f}\right] dr, \quad (2.16)$$

where  $T_{pd}(r, \Omega)$  is a frequency-dependent phase delay function caused by the beam shaping element. The  $\exp\left(-ik \frac{r^2}{2f}\right)$  term is the phase delay caused by the Fourier lens, and

the  $\frac{1}{i\lambda z_f} \exp(ikz_f) \exp\left[ik \frac{(r_f - r)^2}{2z_f}\right]$  term in the integral is the Fresnel approximation as

discussed in section 2.1.1. We use this approximation to describe the propagation process of the pulse traveling from the beam shaping system ( $z = 0$ ) to the target plane ( $z = z_f$ ) in free space.

Next, we need to specify the mathematical form of the frequency-dependent transmission function  $T_{pd}(r, \Omega)$ . For a single frequency  $\Omega_0$ , a top-hat profile can be obtained with the following phase delay function :

$$T_{pd}(\xi) = \beta \left[ \frac{\sqrt{\pi}}{2} \xi \operatorname{erf}(\xi) + \frac{1}{2} \exp(-\xi^2) - \frac{1}{2} \right]. \quad (2.17)$$

Here radius  $r$  is replaced with normalized radius  $\xi = \frac{r}{r_i}$ . Given the phase delay function, the surface profile of the beam shaping element can be determined. In order to obtain the surface profile function, the phase delays in the beam at two different positions are compared. Figure 2.4 shows the geometry of the beam passing through the phase delay element:

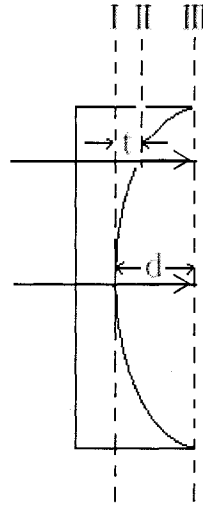


Figure 2.4. Phase delay in different regions of the beam passing through the beam shaping element

Suppose the laser beam's wave front is flat before entering the beam shaping element. When emerging from the beam shaping element, beam A will have a relative phase delay with respect to beam B due to their different traveling distance within the optics and in air.

At surface III, the phase of beam A and beam B are  $\phi_{III-A} = \phi_I + \frac{2\pi d}{\lambda}$ , and  $\phi_{III-B} = \phi_I + \frac{2\pi nt}{\lambda} + \frac{2\pi(d-t)}{\lambda}$ , respectively. Therefore, the relative phase delay between beam A and beam B can be obtained as:

$$\phi_{delay} = \phi_{III-b} - \phi_{III-a} = \frac{2\pi(n-1)t}{\lambda}. \quad (2.18)$$

By comparing Equation (2.18) with the phase delay function in Equation (2.13) given in section 2.2.1, one can get the surface profile of the phase delay element:

$$t(\xi) = \frac{\lambda \cdot \beta \phi(\xi)}{2\pi(n-1)} = \frac{\lambda \cdot \beta \left[ \frac{\sqrt{\pi}}{2} \xi \operatorname{erf}(\xi) + \frac{1}{2} \exp(-\xi^2) - \frac{1}{2} \right]}{2\pi(n-1)}. \quad (2.19)$$

This surface profile is plotted in Figure 2.5 as a function of the normalized radius in the beam shaping element. In this calculation, The value of the scaling factor  $\beta$  is chosen to be 32. When the value of  $\beta$  increases, the surface profile will become even sharper.

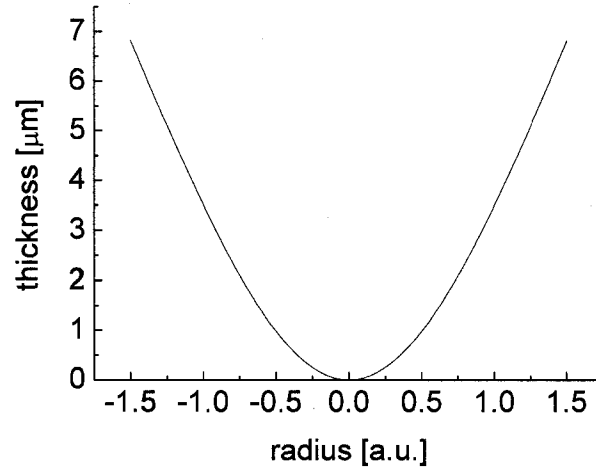


Figure 2.5. Surface profile of the beam shaping element as a function of normalized radius

Now that the surface profile  $t(\xi)$  of the phase delay element is determined, one can write out the frequency-dependent phase delay function  $T_{pd}(\xi, \Omega)$  as:

$$T_{pd}(\xi, \Omega) = \exp\{-i[k_m(\Omega) \cdot t(\xi) + k_v(\Omega)(t(0) - t(\xi))]\}, \quad (2.20)$$

where  $k_m$  and  $k_v$  are the wave vector of each frequency component in the medium and in vacuum, respectively.

The dispersion relationship of the optical medium is given by:

$$k_m(\Omega) = k_m(\Omega_0) + k_m'(\Omega_0)(\Omega - \Omega_0) + \frac{1}{2}k_m''(\Omega_0)(\Omega - \Omega_0)^2 + \dots \quad (2.21)$$

Inserting Equation (2.21) into Equation (2.20), and after arrangement, the expression for the frequency-dependent transmission function is obtained:

$$\begin{aligned} \exp[iT_{pd}(\xi, \Omega)] &= \exp[-iT_{pd}(\xi, \Omega_0) \frac{\Omega - \Omega_0 \cdot n(\Omega_0)}{\Omega_0 - \Omega_0 \cdot n(\Omega_0)}] \cdot \exp[-ik_m'(\Omega_0) \cdot t(\xi) \cdot (\Omega - \Omega_0)] \\ &\quad \cdot \exp[-\frac{1}{2}ik_m''(\Omega_0) \cdot t(\xi) \cdot (\Omega - \Omega_0)^2]. \end{aligned} \quad (2.22)$$

Applying this expression into Equation (2.16) yields the complex amplitude of each frequency component at the target plane ( $z = z_f$ ):

$$\begin{aligned} E(\xi_f, \Omega) &= \int E_0 \exp(-\frac{1}{2}\xi^2) \exp(-(\frac{\Omega - \Omega_0}{\delta})^2) \\ &\quad \cdot \exp[-iT_{pd}(\xi, \Omega_0) \frac{\Omega - \Omega_0 n(\Omega_0)}{\Omega_0 - \Omega_0 n(\Omega_0)}] \\ &\quad \cdot \exp[ik_m'(\Omega_0) \cdot t(\xi)(\Omega - \Omega_0)] \\ &\quad \cdot \exp[-\frac{1}{2}ik_m''(\Omega_0) \cdot t(\xi)(\Omega - \Omega_0)^2] \\ &\quad \cdot \frac{1}{i\lambda z_f} \exp(ik_v z_f) \exp(ik_v \frac{(r_f - \xi r_f)^2}{2z_f}) d\xi \end{aligned} \quad (2.23)$$

This integral can be converted from frequency domain to time domain using the inverse Fourier transform:

$$\begin{aligned}
E(\xi_f, t) = & \int E_0 \exp(-\frac{1}{2} \xi^2) \exp(-(\frac{\Omega - \Omega_0}{\delta})^2) \\
& \cdot \exp[-iT_{pd}(\xi, \Omega_0) \frac{\Omega - \Omega_0 n(\Omega_0)}{\Omega_0 - \Omega_0 n(\Omega_0)}] \\
& \cdot \exp[ik_m'(\Omega_0) \cdot t(\xi)(\Omega - \Omega_0)] \\
& \cdot \exp[-\frac{1}{2} ik_m''(\Omega_0) \cdot t(\xi)(\Omega - \Omega_0)^2] \\
& \cdot \frac{1}{i\lambda z_f} \exp(ik_v z_f) \exp(ik_v \frac{(r_f - \xi r_f)^2}{2z_f}) \exp(i\Omega t) d\xi
\end{aligned} \tag{2.24}$$

Next, one can insert the mathematical expression of  $T_{pd}(\xi, \Omega_0)$  given in Equation (2.13) into the above integral, and make a substitution of  $t' = t - \frac{z_f}{c}$  for  $t$ , where  $t'$  represents the local time at the target plane. The final result is then given by[45]:

$$\begin{aligned}
E(\xi_f, t') = & \int E_0 \exp(-\frac{1}{2} \xi^2) \exp(-(\frac{\Omega - \Omega_0}{\delta})^2) \\
& \cdot \exp[-i\beta(\phi(\xi) \frac{\Omega - \Omega_0 n(\Omega_0)}{\Omega_0 - \Omega_0 n(\Omega_0)} - \xi \xi_f \frac{\Omega}{\Omega_0})] \\
& \cdot \exp[ik_m'(\Omega_0) \cdot t(\xi)(\Omega - \Omega_0)] \\
& \cdot \exp[-\frac{1}{2} ik_m''(\Omega_0) \cdot t(\xi)(\Omega - \Omega_0)^2] \\
& \cdot \frac{1}{i\lambda z_f} \exp(ik_v \frac{\xi_f^2 R_0^2}{2z_f}) \exp(i\Omega t') d\xi
\end{aligned} \tag{2.25}$$

### 2. 3 Nonlinear optical effects

The discussion in previous sections does not include any effects caused by the material's nonlinear properties, which could be essential when the intensity of the pulse becomes extremely high. The effect of the linear susceptibility  $\chi^{(1)}$  is included through the refractive index. For those materials with inversion symmetry at the molecular level, the second-order susceptibility  $\chi^{(2)}$  is zero. The lowest-order nonlinear effects in glasses originate from the third-order susceptibility  $\chi^{(3)}$ . Derived from Maxwell's equation, the Nonlinear Schrödinger Equation (NSE)[46] can be used to study the nonlinear effects of a pulse propagating through an optical material:

$$[(1 + \frac{i}{\omega_0} \frac{\partial}{\partial \tau})^{-1} \nabla_{\perp}^2 + 2ik_0 \frac{\partial}{\partial z} + 2k_0 \hat{D}]A(\vec{r}, t) = -\frac{4\pi\omega_0^2}{c^2} (1 + \frac{i}{\omega_0} \frac{\partial}{\partial \tau}) \tilde{p}, \quad (2.26)$$

where  $\hat{D} = \sum_{n=2}^{\infty} \frac{1}{n} k_n (i \frac{\partial}{\partial \tau})^n$  is the dispersion operator, and  $\tilde{p} = \chi^{(3)}(\omega_0) |A|^2 A$  is the nonlinearity of the material. This equation includes higher-order dispersion effects ( $\hat{D} = \sum_{n=2}^{\infty} \frac{1}{n} k_n (i \frac{\partial}{\partial \tau})^n$ ), spatial-time coupling ( $[(1 + \frac{i}{\omega_0} \frac{\partial}{\partial \tau})^{-1} \nabla_{\perp}^2]$ ) and several nonlinear effects such as self-focusing, pulse splitting, self-steepening, shock wave formation, etc.

Using the expression  $\tilde{p}(\tau) = 3[\chi^{(3)}(\omega_0) + \frac{d\chi^{(3)}}{d\omega} i \frac{\partial}{\partial \tau}] |A|^2 \tilde{A}$ , Equation (2.26) becomes the pulse propagation equation:

$$[(1 + \frac{i}{\omega_0} \frac{\partial}{\partial \tau})^{-1} \nabla_{\perp}^2 + 2ik_0 \frac{\partial}{\partial z} + 2k_0 \hat{D}]A(\vec{r}, t) = -\frac{12\pi\omega_0^2}{c^2} \chi^{(3)}(\omega_0) [1 + (2 + \frac{\omega_0}{\chi^{(3)}(\omega_0)} \frac{d\chi^{(3)}}{d\omega}) \frac{i}{\omega_0} \frac{\partial}{\partial \tau}] |A|^2 \tilde{A} \quad (2.27)$$

Some characteristic lengths can be defined to estimate the distance over which each of the terms in Equation (2.27) becomes appreciable. The diffraction length and the dispersion length are given by  $L_{DIF} = \frac{1}{2} k_0 w_0^2$  and  $L_{DIS} = \frac{T^2}{|k_2|}$  respectively, where  $w_0$  is the incident beam radius,  $T$  is the pulse duration time, and  $k_2$  is the second-order dispersion coefficient of the optical material. The nonlinear length can be defined as  $L_{NL} = \frac{1}{(\omega/c)n_2 I}$ . Using this nonlinear length, we can estimate the significance of nonlinear optical effects for a given physical situation.

Self-phase modulation (SPM) [47] is a nonlinear optical effect that as a laser pulse is traveling in a medium, a varying refractive index of the medium will be induced due to the optical Kerr effect. The variation in refractive index will produce a change in the phase of the optical pulse. The nonlinear refractive index of an optical medium can be

characterized by  $n(I) = n_0 + n_2 I$ , where  $n_0$  is the linear refractive index, and  $n_2$  is the second-order nonlinear refractive index of the medium. For a time-dependent intensity  $I(t)$ , the phase shift of the transmitted pulse is given by  $\phi_{NL}(t) = -n_2 I(t) \omega_0 L / c$ , where  $L$  is the beam path length.

The significance of other propagation effects can also be estimated by considering their characteristic lengths[48]:

- third-order dispersion length:  $L_{TOD} = T^3 / |k_3|$ ,

where  $k_3$  is the third order dispersion coefficient;

- nonlinear self-phase modulation length:  $L_{SPM} = \frac{1}{(\omega/c)n_2 I}$

- self-steepening length:  $L_{ss} = \frac{cT}{n_2^{(g)} I}$ ,

- Raman length:  $L_R = \frac{T}{T_R} L_{NL}$ ,

where  $n_2 = \frac{3}{8n} \text{Re}(\chi_{xxxx}^{(3)})$  is the nonlinear-index coefficient,

and  $n_2^{(g)} = \frac{48\pi^2}{n^2 c} \chi^{(3)}(\omega_0) \left[ 1 + \frac{1}{2} \frac{\omega_0}{\chi^{(3)}(\omega_0)} \frac{d\chi^{(3)}}{d\omega} \right]$ .

In BK7 glass material used for the beam shaping element,  $k_3 = 324 \text{ fs}^3 / \text{cm}$ . For a 100-fs pulse, the propagation length of the third order dispersion is 30 m, therefore, it is only necessary to consider the first- and the second-order dispersion. The nonlinear susceptibility of BK7 glass is  $\chi^{(3)} = 3 \times 10^{-22} \text{ m}^2 / \text{V}^2$ , and the nonlinear index coefficient is  $n_2 = 3.711 \times 10^{-20} \text{ m}^2 / \text{W}$ . For a 1-mm beam propagation length (the thickness of the beam shaping element's base is 1 mm), the self-steepening effect will not be significant when the peak power of the pulse is below  $0.8 \times 10^{14} \text{ W} / \text{cm}^2$ . However, the nonlinear self-phase modulation effect will not be negligible when the pulse peak power reaches

$3.8 \times 10^{11} W/cm^2$ . The Raman scattering time for BK7 glass is only 3 fs, and therefore it can be neglected

Self-phase modulation is dominant among all the nonlinear effects based on the characteristic length of each nonlinear optical effect, and it is therefore incorporated into the beam shaping simulation. SPM will introduce an intensity-dependent phase shift given by:

$$\psi_{NL} = n_2 |E|^2 k_0 L, \quad (2.28)$$

where  $n_2 = \frac{3}{8n} \text{Re}(\chi_{xxxx}^{(3)})$  is the nonlinear-index coefficient, and  $L$  is propagation length. Since this propagation length depends on the radius of the optical elements in the beam shaping system, the SPM phase shift will introduce a radius-dependent distortion of the pulse wave front, and therefore influence the final intensity distribution. The SPM phase shift is added to the diffraction integral in Equation (2.25), and the final intensity profile of the laser beam is given by[49]:

$$\begin{aligned} E(\xi_f, t') = & \iint E_0 \exp(-\frac{1}{2} \xi^2) \exp(-(\frac{\Omega - \Omega_0}{\delta})^2) \\ & \cdot \exp[-i\beta(\phi \frac{\Omega - \Omega_0 n(\Omega_0)}{\Omega_0 - \Omega_0 n(\Omega_0)} - \xi \xi_f \frac{\Omega}{\Omega_0})] \\ & \cdot \exp[ik_m'(\Omega_0) \cdot t(\xi)(\Omega - \Omega_0)] \\ & \cdot \exp[-\frac{1}{2} ik_m''(\Omega_0) \cdot t(\xi)(\Omega - \Omega_0)^2] \\ & \cdot \frac{1}{i\lambda z_f} \exp(-ik_v \frac{(\xi_f R_0)^2}{2z_f}) \exp(i\Omega t') \\ & \cdot \exp(i\psi_{NL}) d\Omega d\xi, \end{aligned} \quad (2.29)$$

where  $t'$  is the local time at the target plane. This equation includes the nonlinear self-phase modulation, as well as the first and the second-order dispersion of the laser pulse.

## 2.4 Experimental setup

### 2.4.1 Fabrication of multi-level beam shaping element

Equation 2.19 gives the surface profile of the phase delay element:

$$t(\xi) = \frac{\lambda \cdot \beta \phi(\xi)}{2\pi(n-1)} = \frac{\lambda \cdot \beta \left[ \frac{\sqrt{\pi}}{2} \xi \operatorname{erf}(\xi) + \frac{1}{2} \exp(-\xi^2) - \frac{1}{2} \right]}{2\pi(n-1)}.$$

However, the surface profile expressed in this equation contains both exponential and error functions, which is very difficult to achieve in the fabrication process. A polynomial fitting is therefore necessary to reduce the complexity of fabrication. The form of polynomial fitting of the phase function  $\phi(\xi)$  is given by:

$$\phi(\xi) = a_2 \xi^2 + a_4 \xi^4 + a_6 \xi^6 + a_8 \xi^8 + a_{10} \xi^{10} + \dots, \quad (2.30)$$

where  $a_i$  ( $i = 2, 4, 6, 8, 10$ ) are the coefficients of the power series:

$$\begin{aligned} a_2 &= 4.73974 \times 10^{-1} \\ a_4 &= -5.50034 \times 10^{-2} \\ a_6 &= 4.99298 \times 10^{-3} \\ a_8 &= -2.37191 \times 10^{-4} \\ a_{10} &= 4.41478 \times 10^{-6} \end{aligned}$$

With the coefficients of the 10th order polynomial fitting of the phase function, the surface profile of the phase delay element can also be fitted. Figure 2.6 shows the profile of the phase delay function calculated from Equation (2.19) and the curve of the 10th order polynomial fitting function. Comparison of the two curves indicates that the 10th-order polynomial series fitting curve agrees very well with the theoretical curve of the phase delay function.

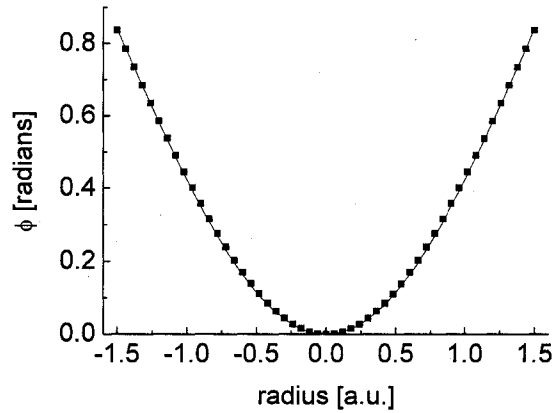


Figure 2.6. Comparison of the theoretical curve and the 10th order polynomial fitting of the phase delay function. The dots represent the theoretically calculated. phase delay profile, and the solid line is the 10th order polynomial series expansion of the phase delay function.

As the distance from the center of the beam increases, the phase delay also increases monotonically. At a certain radius, it will reach  $2\pi$ . Therefore, the phase function can be shifted by  $2\pi$ . And the corresponding thickness of the phase delay element can also be reduced by  $\frac{\lambda}{n-1}$ .

The phase delay element is fabricated with grey scale photolithography technique. Phase levels of the diffractive optical element are generated as grey levels on the optical glass. After being exposed to the writing laser beam (the intensity of which determines the grey scale of the illuminated area on the optical element), the optical glass is etched in 0.6% HF liquid. In this way a pre-designed 3-D microstructure can be produced. The optical material used to fabricate the beam shaping element is BK7 glass. The phase delay pattern is designed for an incident beam of 5 mm radius. The overall diameter of the optical element is 25.4 mm, and the thickness of the glass base is 2 mm (the same

thickness was considered in the theoretical simulation of the beam propagation through the beam shaping element). The fabricated step structure of the phase delay element is shown in Figure 2.7.

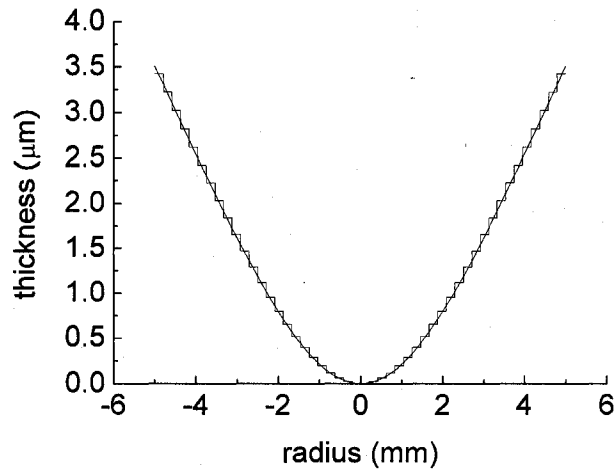


Figure 2.7. Surface profile of the phase delay element designed for  $\beta = 32$ . The smooth curve is the theoretical surface profile, compared with the fabricated step structure.

#### 2.4.2 Beam size control and profile diagnostic systems

Besides the phase delay element, the beam shaping system also includes a Ti:sapphire oscillator, a high-power CPA laser amplification system, a continuous beam expander, a Fourier lens and a beam diagnostics CCD camera. The final result is analyzed with beam diagnostic software compatible with the CCD camera. Figure 2.8 shows a schematic of the optical setup.

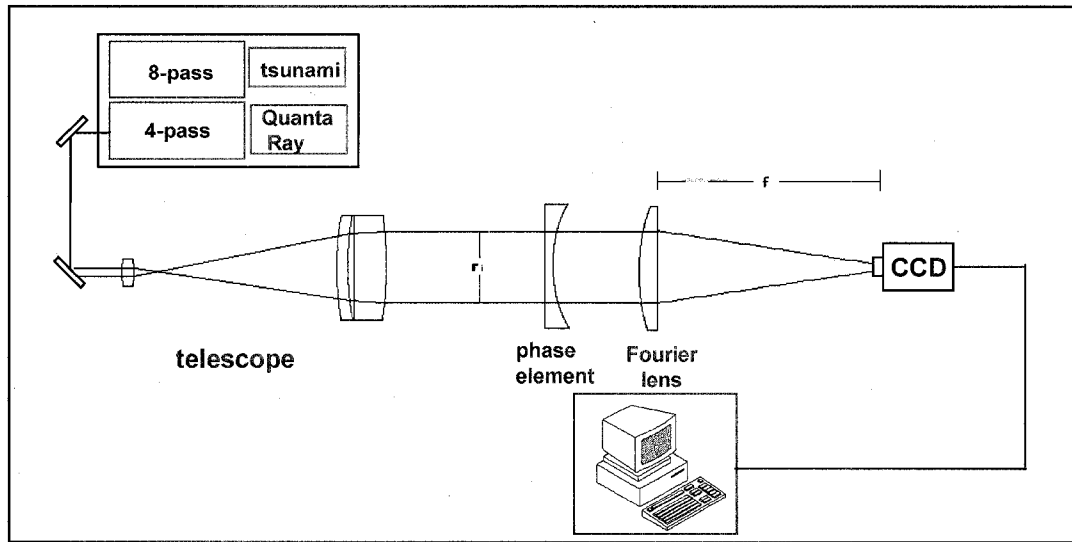


Figure 2.8 Experimental setup of the beam shaping system consisting of a laser beam source, a CPA laser amplification system, a beam shaping setup and a beam diagnostic system.

A Ti:sapphire oscillator and the following CPA laser amplification system serves as the laser beam source in our experiment. Detail description of the CPA laser amplifier is presented in the next chapter. It is a two-stage multi-pass laser amplification system: an eight-pass preamplifier and a four-pass power amplifier. The two amplification stages are independent modules, and this feature allows us to study the beam shaping system with different energy levels. On the one hand, we can use the final output laser beam from the four-pass amplifier to study the high-power beam shaping system. On the other hand, the output from the eight-pass preamplifier with a relatively low energy level can be switched into the pulse compressor directly, skipping the four-pass power amplifier. So we can use the compressed eight-pass output to study the beam shaping system, as well.

A beam expander is used to adjust the beam size to the required input diameter. At a lower energy level, we use a continuous beam expander (Linios Photonics, 4401-256-000-20) with variable magnification factor ranging from 2 to 8. The beam expander includes a zooming group and a focusing group. With setting values of the focusing ring and the zoom ring, a collimated expanded beam can be obtained. Figure 2.9 shows the structure of the beam expander.

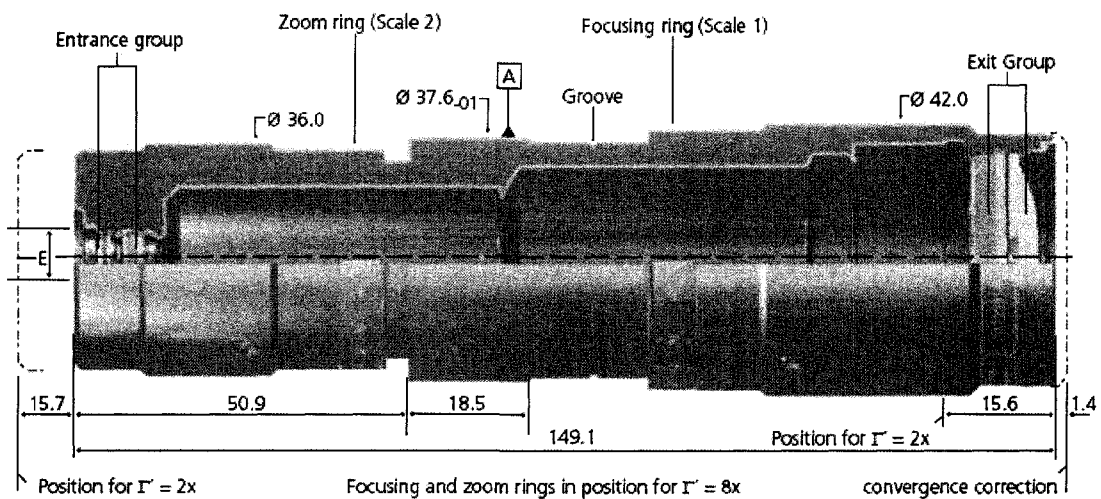


Figure. 2.9. Beam expander with variable magnification

However, at higher energy levels, the damage threshold of the beam expander makes it inapplicable for the experiment. We use three curved mirrors with high-power optical coating (CVI Laser, TLM1 coating) to form the telescope. The expansion ratio is adjustable between 1:1 and 1:3.

The Fourier element in the experiment is a plano-convex focusing lens with 25 cm focal length. The target plane of the whole beam shaping system coincides with the focal plane of the Fourier lens. One flexibility of the beam shaping system is that the output beam size can be scaled up or down by adjusting the focal length of the Fourier element. The scaling factor  $\beta = \frac{2\pi r_1 R_0}{\lambda f}$  indicates that when the beam shaping element is

determined, the input beam size  $r_i$  is fixed, however, the output beam size  $R_o$  can be proportionally scaled in accordance with  $f$ , the focal length of the Fourier element, while the quality of the output top-hat profile is maintained.

At the target plane, the beam profile is diagnosed with a CCD camera (Pulnix, TM-7CN) and is analyzed with a laser beam diagnostic software (Spiricon, LBA-300PC).

### **Summary**

In this chapter, a theoretical model is developed for the ultrashort laser pulse beam shaping process, and a diffraction integral is deduced. The non-linear self-phase modulation is included in the theoretical model for high-power ultrashort laser pulse beam shaping. The experimental setup of the beam shaping system is also described in this chapter, including the laser beam source, the phase delay element, the beam size control and profile diagnostic systems.

## **Chapter 3**

### **Terawatt Laser Amplification System**

In order to study experimentally spatial beam shaping of ultrashort high-energy pulses, a Terawatt laser system is necessary. I built a multi-pass Chirped Pulse Amplification (CPA) system which amplifies the pulse energy of a seed beam to 20 mJ. With a pulse width of 73 fs, the amplified seed beam from the laser amplification system has a peak power of about 0.3 Terawatt. This Chapter describes our laser amplifier and its specification. Section 3.1 gives a brief introduction to the progress in the development of high-power ultrafast lasers. Like other systems, our amplifier consists of a pulse stretcher, two stages of multi-pass amplifiers and a pulse compressor. The pulse stretcher and compressor are discussed in Section 3.2 and Section 3.5, respectively. Section 3.3 and 3.4 describe the eight-pass preamplifier and the four-pass power amplifier. Some photos of the optical layout are also presented at the end of this chapter.

#### **3.1 Introduction**

Advances in ultrafast laser technology[50-52] have opened up new possibilities in many scientific and technological fields. Amplification of ultrashort laser pulses was

dramatically improved since the introduction of CPA technique[53]. The CPA technique is a scheme to amplify the energy of a laser pulse without damaging the gain medium due to the pulse's high peak power and nonlinear processes such as self-focusing. In solid state lasers, some amplifying media have a high energy storage capacity[54]. For example, the Ti:sapphire crystal has a stored energy density of  $1.2 \text{ J/cm}^2$ [55], and that for Nd:glass is  $0.6 \text{ J/cm}^2$ [56]. For ultrashort laser pulse amplification, when the energy storage is fully extracted, the peak power will far exceed the damage threshold of the gain media. The CPA technique provides a very useful solution to avoid damage to the crystal while keeping an efficient energy extraction out of an amplifying media.

The CPA technique works in the following way: an ultrashort laser pulse is stretched out in time by a normally dispersive chirp introduced on the pulse. Various dispersive delay lines such as an optical fiber or a diffractive grating configuration can realize the dispersive chirp on the pulse. This positive chirp increases the pulse duration by a factor of  $10^3$ - $10^4$ , and therefore, while the pulse energy is amplified, the peak power of the chirped pulse is kept at a low level (below the threshold of crystal damage and nonlinear optical effects) so that the pulse will be free of distortion caused by nonlinear optical effects and the gain medium is working safe. Subsequently, in order to temporally compress the pulse duration back, a pulse compressor is used to generate a negative chirp which compensates that of the pulse stretcher, the amplifier medium and any optics in the system. Therefore, the output pulse will have both high energy and short pulse width, resulting in extremely high peak power laser pulses. Figure 3.1 shows the scheme of an amplifier system based on the CPA technique.

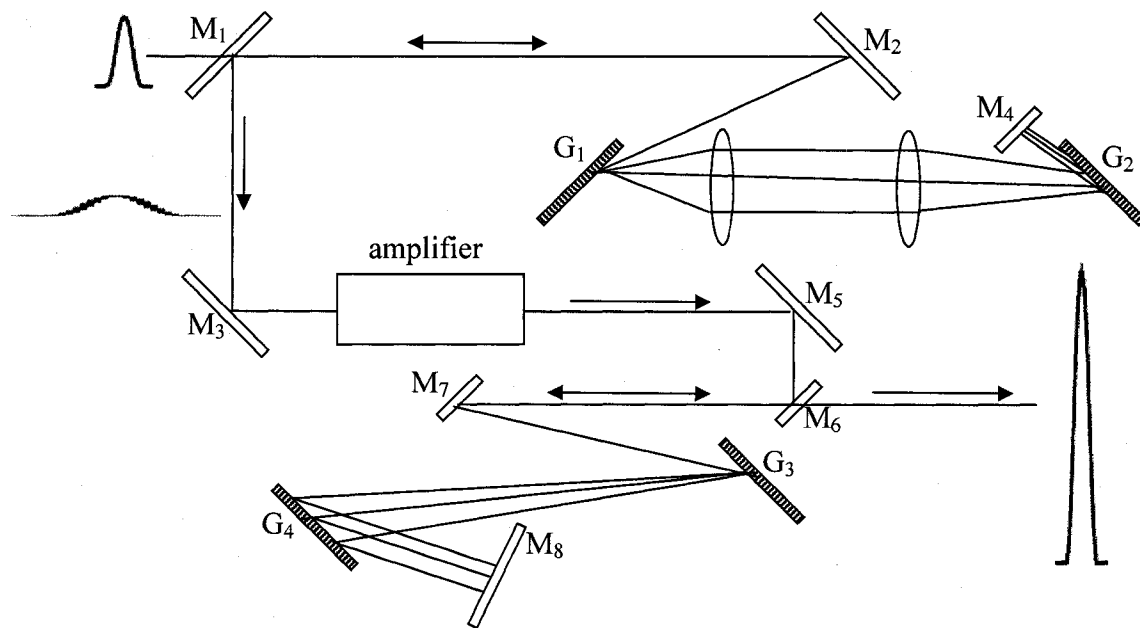


Figure 3.1. Scheme of an amplifier system based on CPA technique

Depending on applications, CPA amplifiers have different configurations[57,58]. For example, in a high repetition-rate CPA system, thermal distortion effects such as thermal lensing, birefringence and stress must be considered. These thermal effects may cause damage to the crystal. While Surface fracture or melting damage of the crystal is mainly caused by local heating of the crystal, most bulk damages of the crystal in a high-power amplifier result from nonlinear self focusing of the laser beam. Thermal effects limit the diameter of the laser crystal in a high repetition-rate amplifier, which in turn limits the amplification of the whole system. For a 120-Hz Nd:YAG laser amplifier, the maximum size of the laser rod is about 0.5 cm. Therefore, using a laser material with good thermal properties is important to reduce heat-related effects. Ti:sapphire crystal has relatively high thermal conductivity (0.11 cal/(°C sec cm) and can therefore dissipate thermal power efficiently. Another solution to overcome thermal lensing is to use a

radially heated compensation plate in the cavity to compensate the thermal lensing effect. A radially heated compensation plate[59] is usually an optical flat with a heating wire on the circumference so that a thermal lens of the opposite sign of the thermal lensing induced by the laser beam is formed. Further cooling the amplifier crystal can also be helpful since the thermal conductivity will increase by an order of magnitude at very low temperature[60].

Thermal birefringence[61,62] is caused by the anisotropic thermal stress in a laser rod which will de-polarize the laser beam[63] and reduce the efficiency of the amplification system[64]. Thermal birefringence can be compensated by a 45° Faraday rotator[65,66]. Lee has studied a diode-pumped, thermal birefringence compensated Nd:YAG laser and analyzed the stability of a resonator with and without the compensation of a rotator[67].

A second example is the ultrashort-pulse CPA systems. In such systems where the pulse duration is less than 100 fs, maintaining a broad bandwidth and minimizing high-order dispersions will be the major concern in the system design. Gain narrowing effect due to the finite gain bandwidth of the amplifier medium will result in a reduction of the spectral bandwidth. For a Ti:sapphire amplifier with an amplification factor of  $10^7$ , gain narrowing limits the output bandwidth within 47 nm[68]. Using thin-film dielectric filters can partially compensate the gain narrowing effect[69]. Hentschel studied gain narrowing compensation in a 0.1-TW, sub-20fs CPA amplification system using a spectral amplitude filter[70]. With a net power gain of  $10^6$ , the amplifier shows obvious gain narrowing effect. The input spectrum bandwidth is 148 nm, and after amplification the

FWHM is reduced down to 41 nm FWHM due to gain narrowing. With the spectral amplitude filter, the bandwidth is partially recovered to 75 nm.

The amplification process also causes a shifting of the spectrum. When the amplification is close to saturation, the red leading edge of a chirped-pulse will deplete the excited-state population, and result in a higher gain than that of the blue edge of the pulse. For very short pulse (<30 fs) amplification, high-order dispersion is the major limiting effect. Adjusting the grating separation and incident angle can cancel the second- and the third-order dispersion. The residual high-order dispersion can be compensated by adding optical materials of negative high-order dispersion in the beam path, using chirped multilayer dielectric coating on the mirrors[71] or actively modulating the pulse's wave front using liquid crystal spatial light modulators[72].

Based on the CPA technique, I built a two-stage multi-pass Terawatt laser amplification system. Figure 3.2 shows a schematic of the whole amplifier system. Each module of the system (pulse stretcher, eight-pass preamplifier, four-pass power amplifier and pulse compressor) will be described in the following sections, respectively.

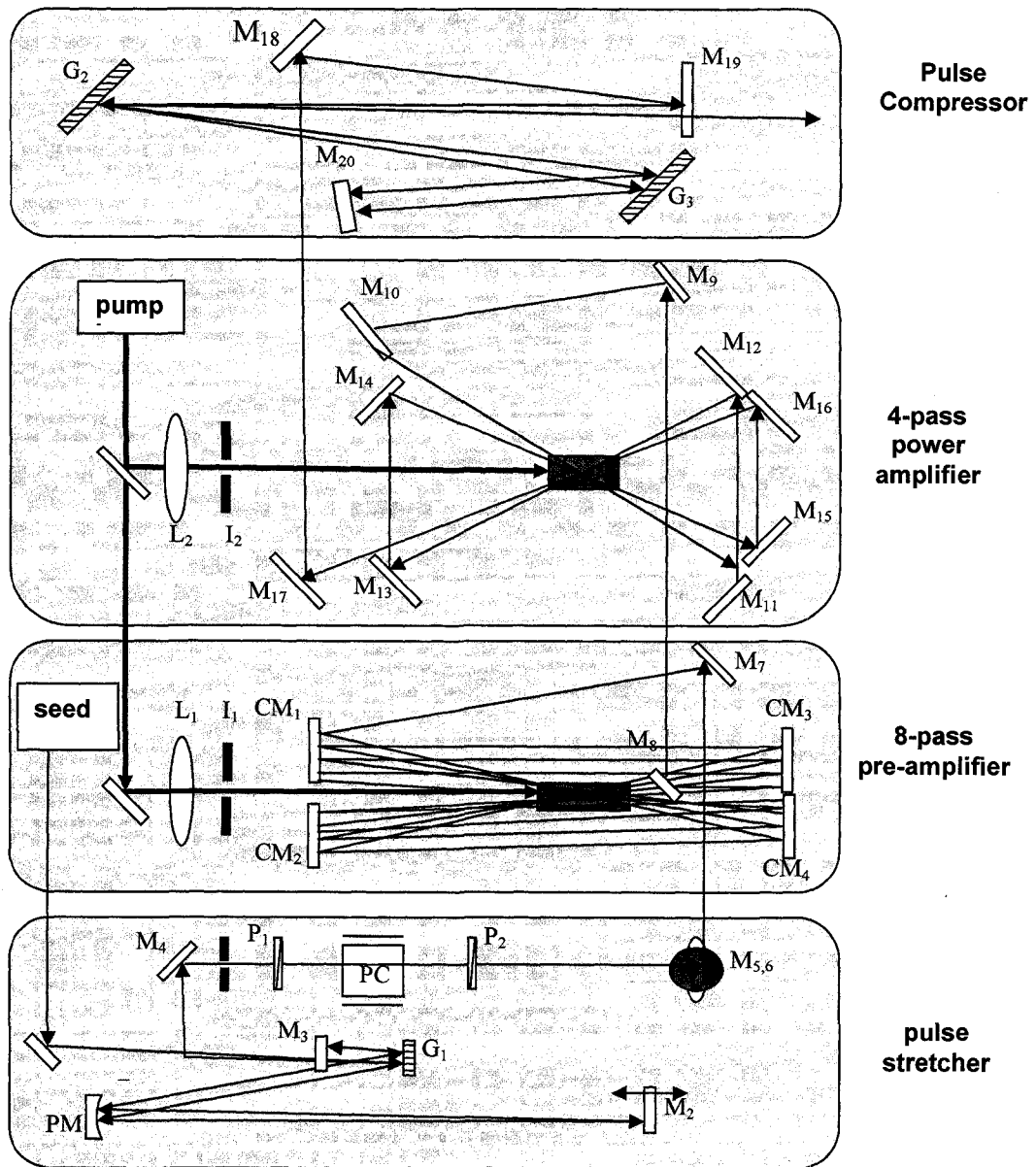


Figure 3.2. Schematic of the Terawatt laser amplifier system.

### 3.2 pulse stretcher

Our amplifier is seeded with an infrared laser beam from a Ti:sapphire oscillator (Tsunami, Spectra-Physics). Specifications of the seed beam are listed in Table 3.1.

Table 3.1. Specifications of the beam seeding the CPA amplifier

Central wavelength:	800 nm
Repetition rate:	80 MHz
Pulse energy:	6 nJ
Beam diameter (FWHM):	2.1 mm
Spectrum bandwidth:	40 nm
Pulse width:	100 fs (uncompressed)

Before entering the multi-pass amplification stages, the seed beam is first stretched by a factor of  $10^3$ . The optical setup of the reflective one-grating pulse stretcher is illustrated in Figure 3.3. The optics in the pulse stretcher is designed in such a way that light with longer wavelengths takes less time to travel through the whole setup than light with shorter wavelengths does, and therefore, a positive frequency chirp is introduced into the pulse.

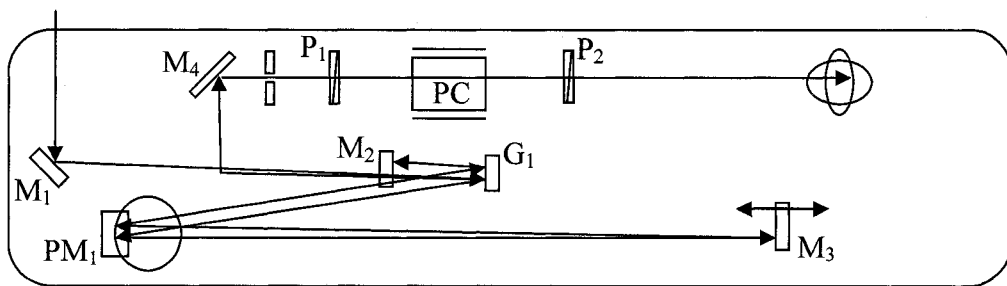


Figure 3.3. Optical setup of the pulse stretcher.

The parabolic mirror  $PM_1$  and the folding mirror  $M_3$  in the pulse stretcher form a 1:1 telescope. The image of the grating  $G_1$  through the telescope is separated from the original grating. Alignment of the telescope is crucial for the recompression of the

stretched pulse. First, the folding mirror is placed at the focal point of the focusing mirror in order to ensure the magnification of the telescope equal to 1, which can guarantee the image of the grating has exactly the same characteristics as the original grating. Second, the orientation of the folding mirror must be aligned to be perpendicular to the beam so that the image of the grating is perfectly stigmatic on the optical axis of the telescope. Otherwise, the diffracted beam will be incident on the second grating (the image of the original one) at a slightly different angle. This will result in both spatial chirp and astigmatism in the laser beam and makes it difficult to temporally compress the pulse duration back to its original width.

Figure 3.4 is a geometrical optics illustration of the diffracted beam passing through the imaging telescope in the pulse stretcher. An equivalent two-lens pulse stretcher configuration replaces the all-reflective setup in this figure. The positions of the second lens and grating are symmetric to those of the first lens and grating with respect to the middle line between the two lenses. The image of the first grating is located behind the second one, and the distance between the two determines the effective dispersion of the pulse stretcher.

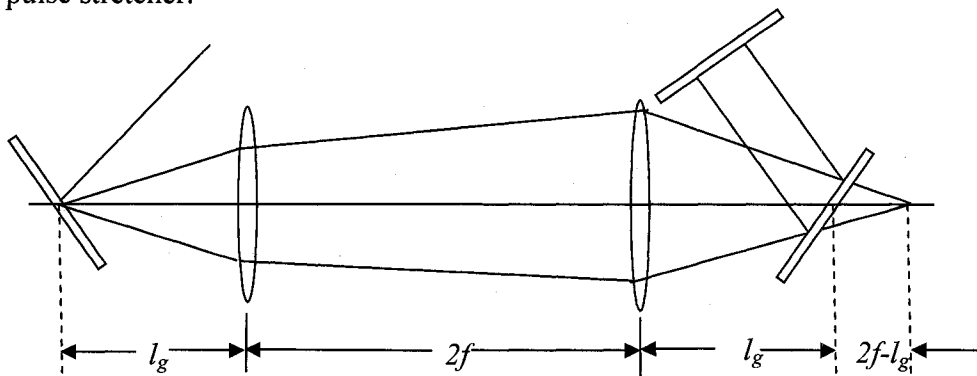


Figure 3.4. Geometrical optics illustration of the pulse stretcher.

The grating is placed at a distance of  $l_g$  before the first lens. After the telescope, the grating is imaged at a distance of  $2(f-l_g)$  behind the second lens. Using geometrical optics, it can be shown that the converging angle of the beam after the second lens is equal to the dispersion angle of the incident beam at the first grating. Therefore, the beam spreads on the second grating with a width of  $2(f-l_g)\sin\Delta\beta$ , where  $\Delta\beta$  is the difference between the dispersion angles of the longest and the shortest wavelengths. As a result of this spreading width, a difference in optical path length among the dispersed beams is introduced into the pulse. The optical path length difference between the shortest and the longest wavelengths is  $\Delta p = \frac{w}{\cos\beta}(\sin\beta + \sin\alpha)$ , where  $\alpha$  is the incident angle on the grating, and  $\beta$  is the dispersion angle of the central wavelength. Considering the return path of the beam through the pulse stretcher, the total path length difference is  $2\Delta p$ . Therefore, the duration of the stretched pulse is given by:

$$\Delta t = \frac{4(f-l_g)\sin\Delta\beta}{\cos\beta}(\sin\beta + \sin\alpha)3.33\text{ps/mm} ,$$

where the incident angle  $\alpha$  and the dispersion angle  $\beta$  for a given wavelength  $\lambda$  is related by the grating equation:

$$\sin\beta + \sin\alpha = \frac{\lambda}{d} .$$

The equation shows that the effective dispersion length in a pulse stretcher is four times the distance between the grating  $G_1$  and the folding mirror  $M_3$  (shown in Figure 3.5). Therefore, the stretching capability of a pulse stretcher can be controlled by adjusting the separation between the grating and the folding mirror. On the other hand, however, the beam spreads on the grating with a width of  $2(f-l_g)\sin\Delta\beta$ , so the finite

dimension of the grating will put a limit on the final pulse duration out of the pulse stretcher.

Our pulse stretcher adopts an all-reflective design in order to avoid chromatic aberrations introduced by lenses. The focusing mirror used in the stretcher is a 6-inch gold-coated parabolic mirror with a focal length of 30 inches. The folding mirror located at the focal point of the parabolic mirror is a 1-inch by 4-inch rectangular mirror with gold coating. Specifications of the grating used in the stretcher are listed in Table 3.2. The distance between the grating and the folding mirror is 40 cm. Since the laser pulse travels four times within the pulse stretcher, therefore, the effective dispersion distance is 160 cm. In order to achieve the maximum diffractive efficiency of the gratings, the seed beam is incident at the Littrow angle of  $28.6^\circ$  (i.e. the direction of the first-order diffraction beam coincides with that of the incident beam). At the Littrow configuration, the energy distributed to the first-order diffracted portion of the beam reaches a maximum.

Table 3.2. Specifications of the grating used in the pulse stretcher

Groove frequency:	1200 grooves/mm
Blaze angle:	$21.1^\circ$
Ruled width:	96 mm
Groove length:	46 mm
Littrow angle ( for 800 nm):	$28.6^\circ$
Coating:	gold
Resolving power:	$1.15 \times 10^5$

The spectrum of the seed beam before the pulse stretcher is shown in Figure 3.5. The spectrum shows a nice Gaussian profile centered at 800 nm with a bandwidth of 40 nm.

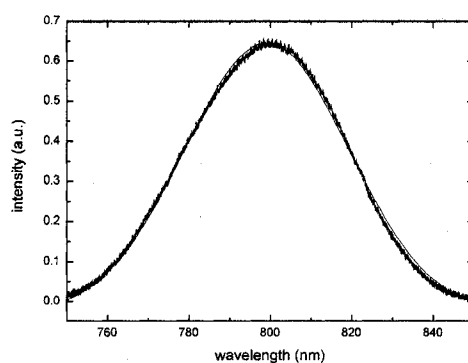


Figure 3.5. Spectrum of the seed beam before entering the pulse stretcher.

Bandwidth of this spectrum is 40.35 nm centered at 800 nm.

After the pulse stretcher, the bandwidth is reduced to 32 nm by the optics in the stretcher, as shown in Figure 3.6. Since the bandwidth corresponding to a Fourier-transform-limited pulse width of 30 fs is 31.3 nm, therefore, the spectrum after the pulse stretcher is still wide enough to support the recompression of the pulse width back to sub-100 fs level.

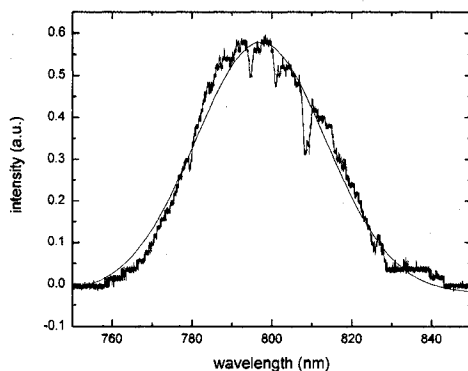


Figure 3.6. Spectrum of the seed beam after the pulse stretcher. The bandwidth of this spectrum is 32.8 nm.

It is necessary to check the spatial profiles of the seed beam before and after the pulse stretcher to make sure no spatial chirp is introduced into the pulse due to misalignment of the telescope in the pulse stretcher. Figure 3.7 shows the comparison between the spatial mode profile of the incident seed beam and that of the beam after

being temporally stretched. This figure shows that the spatial profile is well recovered after the pulse stretcher. When a narrow part of the dispersed spectrum is blocked, the intensity all over the profile is homogeneously decreased without showing any spatial distortion. This indicates that the pulse is free of spatial chirp after passing through the telescope in the pulse stretcher.

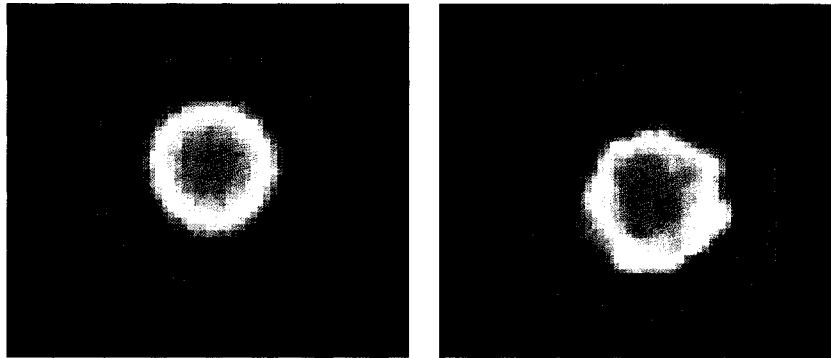


Figure 3.7. Comparison of the spatial mode profiles of the seed beam before and after the pulse stretcher.

The autocorrelation measurement of the stretched pulse shows that the pulse is stretched to 156 ps, corresponding to a stretching factor of 1,500 for a 100-fs input pulse.

Figure 3.8 shows the autocorrelation curve for the stretched pulse.

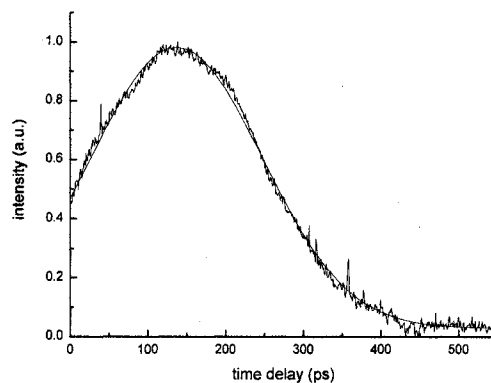


Figure 3.8. Autocorrelation measurement of the stretched pulse. FWHM of the curve is 220 ps. Assuming a Gaussian pulse profile, the pulse width is 156 ps.

### 3.3 Preamplifier

The stretched pulse is injected into an eight-pass preamplifier stage in which the pulse energy is amplified by a factor of  $\sim 10^6$ . The preamplifier uses a multipass configuration because such systems have less high-order phase accumulation than a regenerative system does, and therefore it is easier for a stretched pulse to be compressed back to femtosecond level. The optical setup of the eight-pass preamplifier is shown in Figure 3.9.

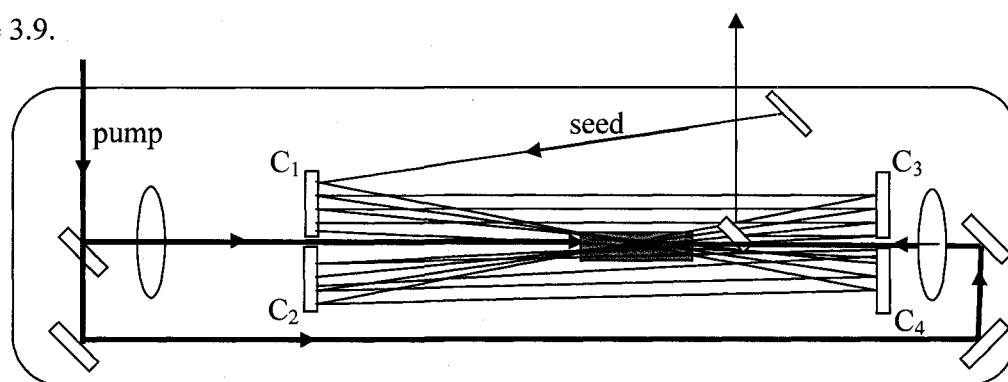


Figure 3.9. Optical setup of the eight-pass amplifier.

The gain medium used in the amplifier is a highly doped Ti:sapphire rod. Some physical specifications of the Ti:sapphire crystal are listed in Table 3.3.

Table 3.3. Physical specifications of the Ti:sapphire crystal used in the eight-pass preamplifier

Rod diameter :	$5 \pm 0.05\text{mm}$
Beam path length :	7 mm
Cut angle :	$60.4^\circ$ (Brewster cut)
Orientation :	E-vector parallel to c-axis
Dopant concentration :	0.25%
Damage threshold :	$5 \text{ J/cm}^2$
Density :	$3.98 \text{ g/cm}^3$

The Ti:sapphire rod is placed at the focal points of four concave mirrors (C1 through C4 in Figure 3.11) . The focal lengths of these curved mirrors are 50 cm. The seed beam is reflected four times on each curved mirror so that it passes through the Ti:sapphire crystal eight times.

A Nd:YAG laser (Spectra-Physics, Quanta-Ray PRO-290-30) is used to pump the pre-amplifier crystal. The wavelength of the pumping light is 532 nm and the pulse duration is 10 ns. The pumping energy used in the 8-pass amplifier is 30 mJ per pulse. In order to obtain the maximum pumping efficiency, the pump beam is split with a 50% beam splitter and pumps the crystal from both sides. To avoid back reflections, the pump beam is vertically offset from one side by a slight angle and an iris is used on each side of the crystal to block the transmitted pumping light while the main pumping beam goes through the aperture.

The repetition rate of the seed beam coming out of the pulse stretcher is 80 MHz, while that of the pump laser is 30 Hz. Therefore, a pulse divider is employed to reduce the high pulse frequency down to 30 Hz. The Pockels cell used between the pulse stretcher and the preamplifier (shown in Figure 3.5) operates as a pulse picker. The Pockels cell works as a half-wave plate between two Calcite polarizers oriented at a 90° angle to one another. High voltage electric pulses are generated by an external power supply. When a high voltage pulse is applied to the Pockels cell, the polarization of the seed beam will be rotated by 90°, and therefore it can go through the second polarizer. Controlling the electric pulses enables the Pockels cell to select a sequence of optical pulses from a high frequency pulse train.

Obviously, the seed beam pulses, the pump beam pulses and the high voltage pulses applied to the Pockels cell must be synchronized such that the seed beam and the pump beam temporally overlap with each other. Furthermore, the time delay between the seed beam and the pump beam must also be tunable to optimize the amplification of the seed beam. The timing scheme used in our amplification system is shown in Figure 3.10.

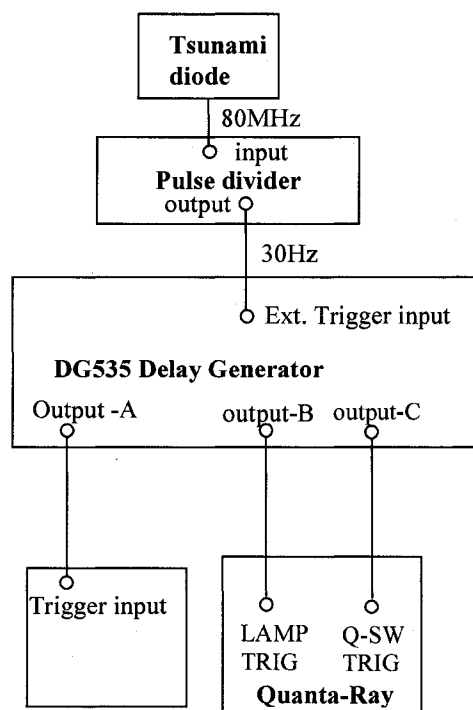


Figure 3.10. Synchronization timing scheme used in the amplification system.

The Delay Generator (Stanford Research Systems, DG535) can be triggered with an external source. It has four output channels which can simultaneously give four synchronized TTL signals of the same frequency, and the time delay between any two output signals can be adjusted at a pico-second resolution. One channel signal is used to trigger the Pockel cell so that the temporal aperture of the Pockels cell coincides with the arrival of the seed beam pulses. Two other channel signals are used to trigger the LAMP

and Q-Switch input in the Quanta Ray laser, respectively. The maximum output of the pumping light can be obtained by adjusting the Q-Switch time delay with respect to the LAMP signal. Further adjustment of the time delay between the LAMP and the Pockels cell triggering time will give the seed beam pulse an appropriate time delay with respect to the pump beam pulse to achieve the maximum amplification. The time delays used in our amplification system are as follows:

- a) LAMP triggering time delay: 0.030000 ms,
- b) Q-Switch triggering time delay: 0.223406 ms,
- c) Pockels cell triggering time delay: 0.218212 ms.

With this timing scheme, the Pockels Cell and the Quanta-Ray laser are synchronized with a tunable time delay between the seed beam and the pump beam.

We can estimate the small signal gain of the eight-pass amplifier from the optical properties of the Ti:sapphire crystal. Table 3.4 gives the absorption and emission cross sections and other optical parameters of the Ti:sapphire crystal.

Table 3.4. Optical specifications of the Ti:sapphire crystal in the preamplifier

Index of refractivity at 800 nm :	1.76
Index of refractivity at 532 nm :	1.77
Absorption cross section $\sigma_{abs}$ :	$4 \times 10^{-20} \text{ cm}^2$
Emission cross section $\sigma_{em}$ :	$3.1 \times 10^{-19} \text{ cm}^2$
Absorption coefficient $\alpha$ :	$4.1 \text{ cm}^{-1} \pm 20\%$

The density of  $\text{Ti}^{3+}$  ions in the sapphire crystal is  $8.6 \times 10^{19} \text{ cm}^{-3}$  for a 0.25% doped  $\text{Al}_2\text{O}_3$  crystal. The 30 mJ/pulse pumping energy is focused down to 1.2 mm diameter. With the absorption cross section  $\sigma_{abs}$ , one can obtain the excited state population to be

$2.47 \times 10^{19} \text{ cm}^{-3}$ . Therefore, the small signal gain is given as:

$$g_0 = N \cdot \sigma_{em} = 2.47 \times 10^{19} \cdot 3.1 \times 10^{-19} = 7.7 \text{ cm}^{-1}$$

When the pulse intensity is approaching the saturation intensity of the medium, the gain is given by  $g = \frac{g_0}{1 + E/E_{sat}}$ , where  $E_{sat}$  is the saturation fluence. For Ti:sapphire crystal, the saturation fluence is about  $0.9 \text{ J/cm}^2$ . The pumping intensity attenuates along the beam path into the crystal exponentially. At a distance  $L$  from the surface of the crystal, the pumping intensity can be written as  $I = I_0 \exp(-\alpha L)$ , where  $\alpha$  is the absorption coefficient of the Ti:sapphire crystal at the wavelength of pumping light, and  $I_0$  is the pumping intensity outside the crystal. Therefore, the total gain in the eight-pass amplifier can be obtained by integrating over the full beam path length through the crystal.

The parameters of our eight-pass amplifier are listed in Table 3.5. To avoid any damage to the gain crystal, the pumping fluence is about half of the damage threshold of the Ti:sapphire crystal. The crystal absorbs about 87% of the pumping energy, resulting in a total amplification of  $2.5 \times 10^6$  after eight passes. The output fluence is very close to the saturation fluence. Table 3.6 shows the amplification for each pass. It also indicates that the amplification saturates after eight passes through the gain medium.

Table 3.5. Specifications of the eight-pass preamplifier

Seed beam pulse energy:	1 nJ
Pump beam pulse energy :	30 mJ (pumping from both sides)
Focused seed beam diameter :	0.6 mm (10-90% level)
Focused pump beam diameter:	1.2 mm (10-90% level)
Amplified pulse energy :	2.5 mJ
Total amplification factor:	$2.5 \times 10^6$
Amplified seed beam fluence:	$0.88 \text{ J/cm}^2$

Table 3.6. Amplification factor and pulse energy per pass

pass	Amplification factor	pulse energy
1	7.3	7.3 nJ
2	7.6	55.4 nJ
3	6.7	371.7 nJ
4	6.9	0.00256 mJ
5	6.3	0.0162 mJ
6	6.0	0.097 mJ
7	5.9	0.572 mJ
8	4.7	2.688 mJ

A CCD camera (Spiricon, LBA-PC) is used to capture the spatial mode profile of the amplified beam after the eight-pass preamplifier, as shown in Figure 3.13 (a). The intensity distributions along the horizontal and vertical cross sections of the beam profile are also plotted, (Figure 3.11 (b) and (c)). It can be seen that the Gaussian spatial profile of the seed beam is well maintained after amplification.

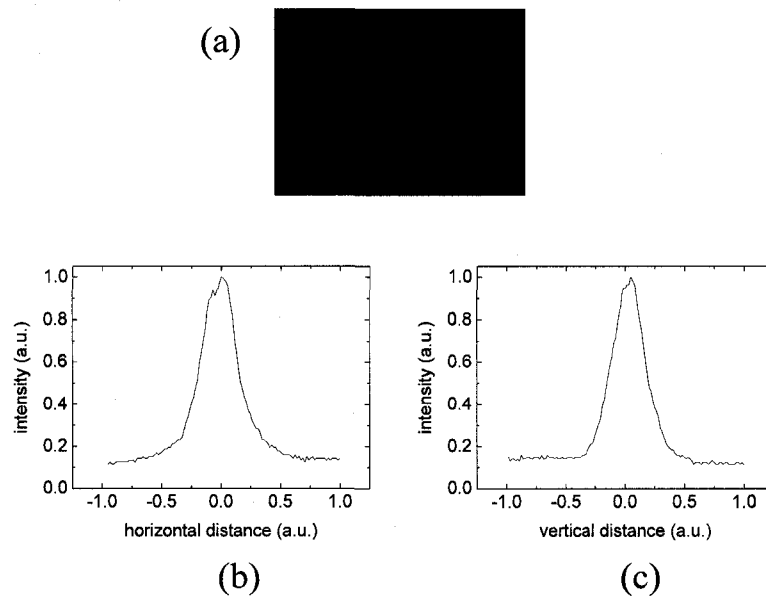


Figure 3.11. Spatial mode profile of the amplified beam after the eight-pass preamplifier. (a) CCD captured profile; (b) intensity distribution along the horizontal cross section of the beam profile; and (c) intensity distribution along the vertical cross section of the beam profile.

The autocorrelation trace of the amplified beam is plotted in Figure 3.12, showing an autocorrelation width of 258 ps. The Fourier transform of a Gaussian-shaped pulse gives a ratio of 1.41 between the autocorrelation width and the pulse width. Therefore, the actual pulse width is 181 ps.

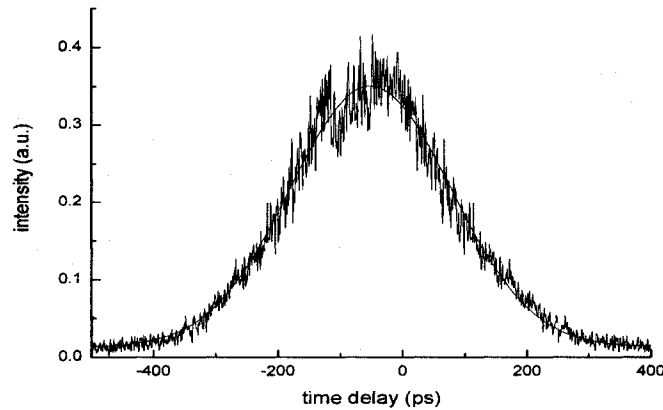


Figure 3.12. Autocorrelation measurement of the pulse width after the eight-pass preamplifier. Assuming a Gaussian temporal profile, the pulse duration is 181 ps.

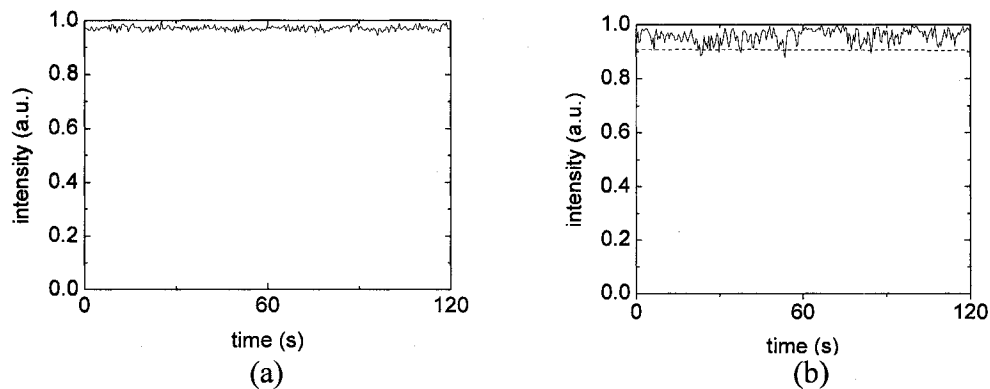


Figure 3.13. stability of the output power from the eight-pass amplifier: (a) pulse-to-pulse stability of the unamplified seed beam; (b) pulse-to-pulse stability of the amplified seed beam.

The output power stability is also measured with an A/D converter (Stanford Research systems, SR245). Figure 3.13 shows the output pulse-to-pulse stability

compared with that of the seed beam. This measurement shows that the output power varies within  $\pm 5\%$  of the mean value of a series of pulses.

### 3.4 Power amplifier

The second amplification stage of the Terawatt amplifier is a four-pass power amplifier. The four-pass setup is similar to that of the preamplifier, but the seed beam is no longer focused since the energy level in the power amplifier is much higher than in the first amplification stage. However, the pump beam is slightly focused in order to reach sufficient pumping intensity in the crystal. Similar to the pumping configuration in the eight-pass amplifier, the pump beam in the four-pass is also split by a 50% beam splitter so that the crystal is pumped from both sides. This can both increase the pumping efficiency and keep the crystal safe. The optical layout of the power amplifier is depicted in Figure 3.14.

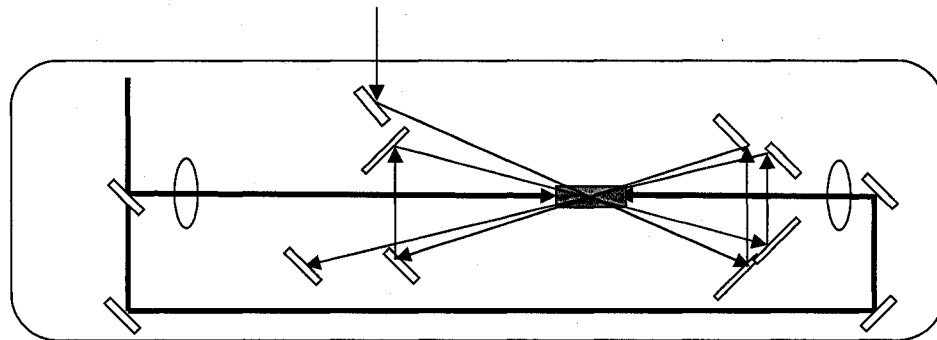


Figure 3.14. Configuration of the four-pass power amplifier.

An iris is used in the beam path between the two amplification stages as a spatial filter to block the Amplified Spontaneous Emission (ASE) from the preamplifier. Spatial coherence of ASE is much less than that of the amplified short pulse itself, so it can be blocked out with a spatial filter.

In the power amplifier, cooling of the Ti:sapphire crystal rod is essential. A Peltier thermal electric cooler is used to control the temperature of the crystal. The crystal mount is sandwiched between two pieces of 40-Watt thermal electric chillers (Melcor Corp., CP1.0-127-06L/W45). Silver paste (Arctic Silver Inc., Arctic Silver V) rather than indium foil (which is normally used as heat transfer media in a laser amplification system) is used between the contacting surfaces of the crystal, the copper mount, the Peltier chips and the water-cooled heat sink. Table 3.7 gives a comparison of the thermal properties between Indium foil, silicon-based thermal grease and the silver paste used in our power amplifier.

Table 3.7. Thermal properties of various heat transfer media[73]

contact	thermal conductance (W/m <sup>2</sup> -°C)	thermal resistance (°C - in <sup>2</sup> / W)
indium	9,000	
silicon grease	20,000	0.05
silver paste	350,000	0.0045

Table 3.7 shows that silver paste has a much higher thermal conductance than the other two heat transfer media. Moreover, the amorphous shape of silver paste can fill the micro gaps between the contacting surfaces. With such a cooling solution, the absorbed heat of the crystal can be dissipated into the heat sink efficiently, and the temperature of the Ti:sapphire crystal can be well controlled.

Before being injected into the power amplifier, the output beam from the eight-pass is expanded with a 1:2 telescope which increases the beam size to 3.5 ~ 4 mm diameter. Due to the high power level of the beams in the four-pass amplifier, the mirrors used in this stage are coated with high-power coating (CVI Laser Corp., TLM1 coating).

The Ti:sapphire crystal used in the four-pass is a 10-mm-diameter by 7-mm-beam-path-length rod. The pump beam is moderately focused by a plano-convex lens with 1500-mm focal length. Other specifications of the power amplifier are listed in Table 3.8.

Table 3.8. Specifications of the four-pass power amplifier

Seed beam pulse energy:	2 mJ
Pump beam pulse energy :	650 mJ (pumping from both sides)
Seed beam diameter :	3.5mm
Focused pump beam diameter:	4.5 mm
Amplified pulse energy :	40 mJ
Total amplification factor:	30
Amplified seed beam fluence:	0.42 J/cm <sup>2</sup>

Figure 3.15 shows the pulse spectrum after the power amplifier. The measured bandwidth is about 23 nm. Due to the gain narrowing effect during the amplification process, the spectral bandwidth of the amplified pulse is much narrower than that of the original seed beam.

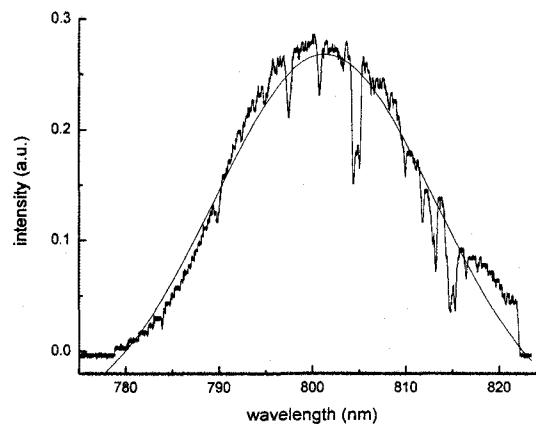


Figure 3.15. Spectrum of the amplified pulse after the four-pass amplifier.

Table 3.9 gives the relationship between the transform-limited pulse duration and the spectral bandwidth (FWHM) for Gaussian-shaped pulses centered at 800 nm. It can

be seen that the 23-nm bandwidth is wide enough to support a sub-100-fs pulse recompression.

Table 3.9. Pulse duration versus spectral bandwidth for Gaussian-shaped pulses

Gaussian bandwidth (nm)	Gaussian pulse duration (fs)
9.4	100
18.8	50
31.3	30
94	10

The autocorrelation trace of the amplified pulse after the four-pass amplifier is shown in Figure 3.16. Before amplification in the four-pass stage, the pulse width was 180 ps, and this autocorrelation measurement indicates that the pulse width is moderately stretched by approximately 10 ps during the power amplification.

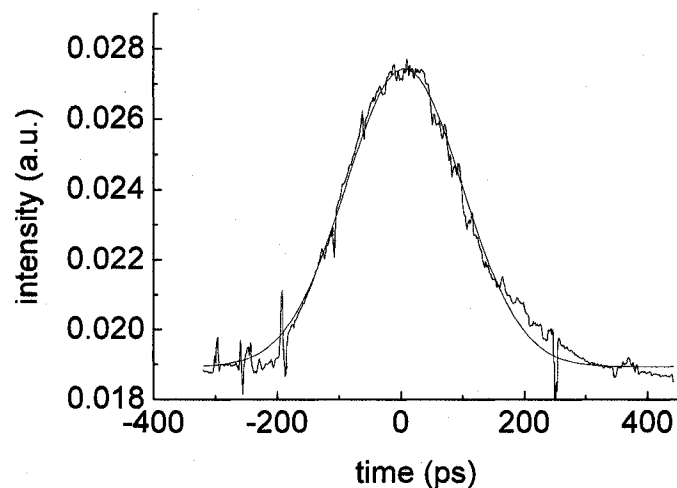


Figure 3.16. Autocorrelation measurement of the pulse width after the four-pass preamplifier. Assuming a Gaussian temporal profile, the pulse duration is 189 ps.

### 3.5 Pulse compressor

The final stage of the Terawatt amplifier system is an all-reflective pulse compressor. The arrangement of the compressor is shown in Figure 3.17.

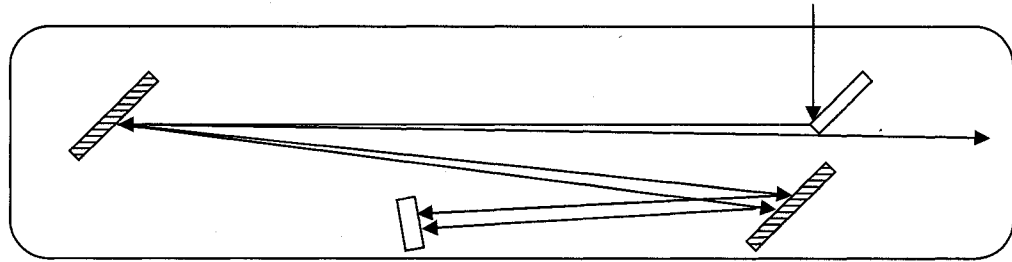


Figure 3.17. Optical configuration of the pulse compressor.

This pulse compressor works in exactly the reversed way of the pulse stretcher as discussed in Section 3.2. The two dispersive elements used in the compressor are gold-coated, 1200 grooves/mm reflective gratings with the same blaze angle as that of the grating used in the pulse stretcher. The effective dispersion distance is twice the separation between the two gratings. A negative chirp is introduced into the pulse during the propagation of this distance. However, the effective dispersion distance in the compressor is not exactly the same as that of the pulse stretcher. When the beam travels through all the optics and Ti:sapphire crystals in the amplification system, some extra dispersion is introduced into the pulse. The negative chirp induced by the pulse compressor will compensate the dispersion coming from both the pulse stretcher and the optical materials present in the amplifier stages. Therefore, the distance between the two gratings is more than half of the effective dispersion distance in the pulse stretcher.

The amplified beam is incident on the gratings at the Littrow angle, but the return pass is slightly offset in the vertical direction in order to couple the beam out of the compressor.

Diffraction efficiency and damage threshold of the gratings in the pulse compressor are the two major factors that limit the output of the amplification system. When used in the first-order Littrow configuration, the gold-coated reflective grating used in our compressor has a diffraction efficiency of 85%. This leads to a ~50% energy loss after the compressor since the beam diffracts from the gratings four times. The damage threshold of a gold coating is typically  $\sim 0.2 \text{ J/cm}^2$  [74,75] for short pulse (0.1ps). The peak power of the pulse from our amplifier will reach  $\sim 0.3 \text{ TW}$  after compression. Therefore, before the pulse enters the compressor, a 1:5 telescope is set up in the beam, expanding the beam diameter to 15 mm. The parameters used in the pulse compressor are listed in Table 3.10.

Table 3.10. Specifications of the pulse compressor

Input pulse energy :	40mJ
Incident spectral bandwidth :	23.5nm
Incident beam size:	$1.77 \text{ cm}^2$
Distance between the gratings:	82 cm
Output pulse width:	73 fs
Output bandwidth:	23.4 nm
Output pulse energy:	20 mJ

The spectrum of the pulse after the compressor is shown in Figure 3.18. The FWHM of the spectrum is maintained at 23 nm compared to the bandwidth of the pulse entering the compressor.

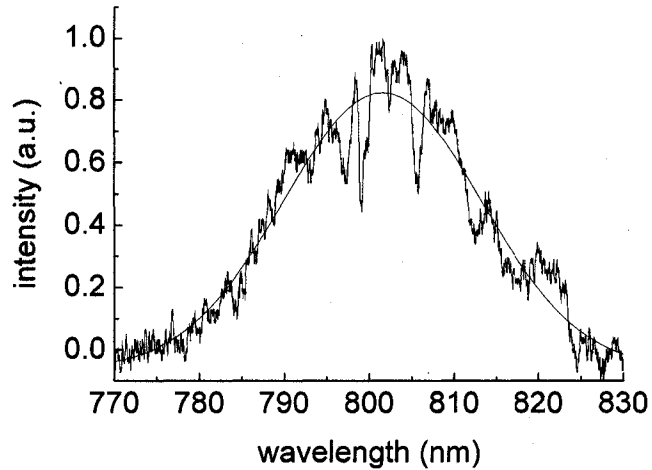


Figure 3.18. Spectrum of the pulse after the compressor. The bandwidth of this spectrum is 23.4 nm.

The autocorrelation measurement of the output pulse width is plotted in Figure 3.19. A Gaussian fitting indicates that the pulse width is 73 fs. Since the output energy is 20 mJ per pulse, the peak power of the compressed pulse reaches 0.3 TW.

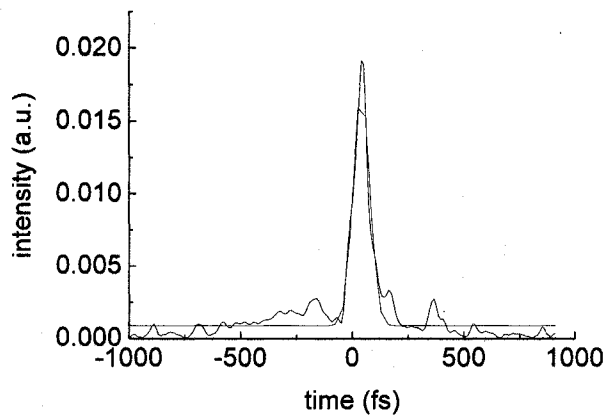


Figure 3.19. Autocorrelation measurement of the pulse width after the pulse compressor.

Figure 3.20 shows the output beam mode profile. The lower right spot is due to the reflection to the CCD camera. The beam mode shows a good Gaussian profile. Figure 3.20 (b) and 3.20 (c) shows the intensity distributions along the horizontal and the

vertical cross section of the beam profile, respectively. In the vertical cross section, a tilted tail of the intensity profile is caused by the background light which is brighter on the top than at the bottom of the CCD sensor area.

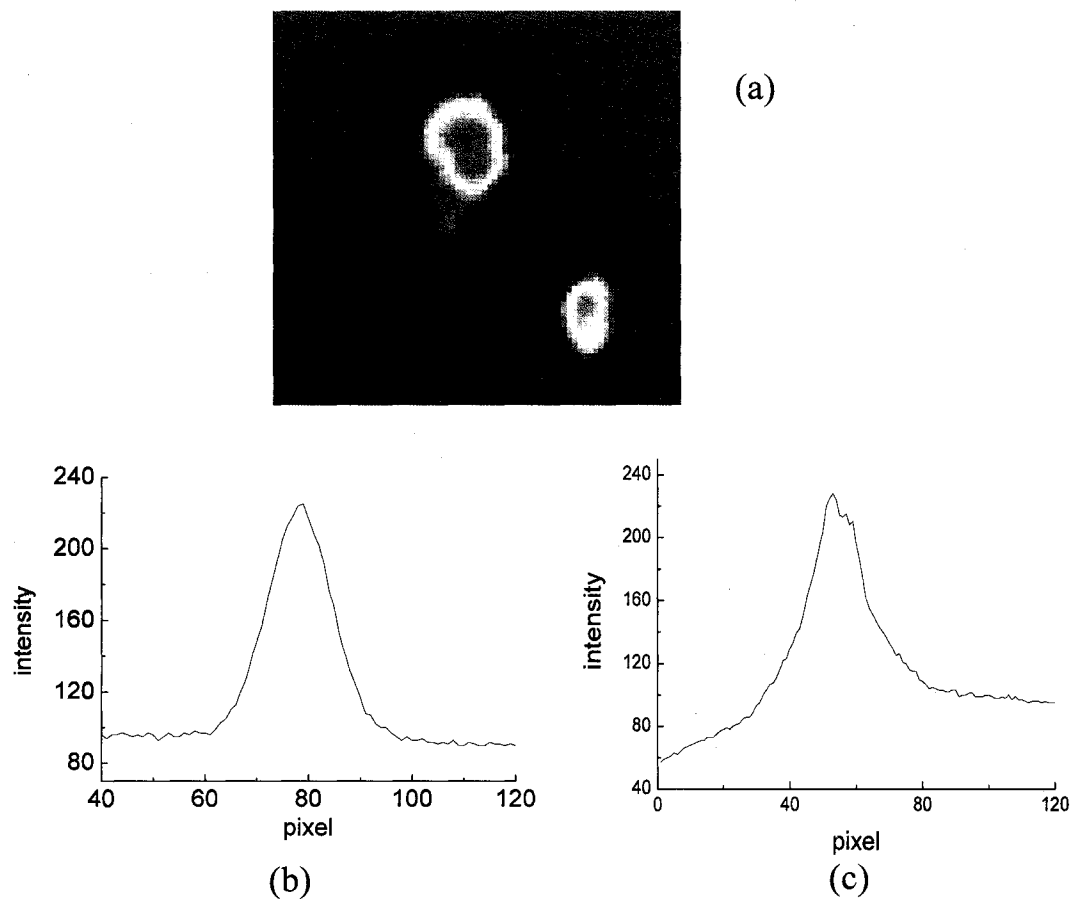


Figure 3.20. Beam mode profile after the compressor: (a) CCD captured beam profile; (b) intensity distribution along the horizontal cross section of the beam profile; and (c) intensity distribution along the vertical cross section of the beam profile.

A picture of the overall layout of the CPA laser amplification system is shown in Figure 3.21. The pictures of the eight-pass preamplifier stage and the following four-pass power amplifier are shown in Figure 3.22 and 3.23, respectively.

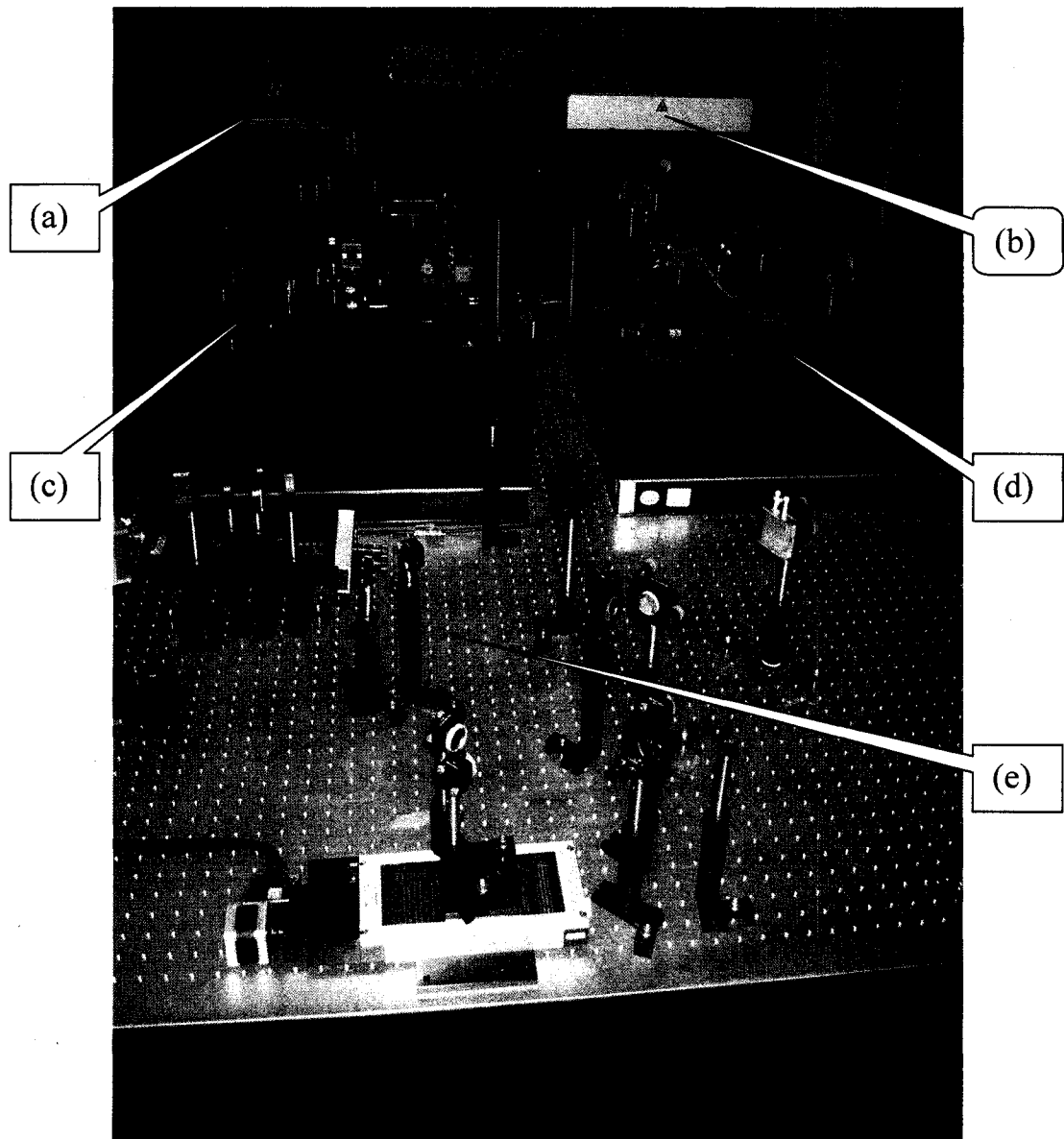


Figure 3.21. Layout of the whole CPA laser amplification system. (a) Tsunami Ti:sapphire laser operating at 800 nm wavelength, serving as the seed beam in the amplification system; (b) Quanta-Ray Nd:YAG laser, the pumping laser in the system; (c) Pulse stretcher and 8-pass pre amplification stages; (d) 4-pass power amplification stage; (e) Two-grating based pulse compressor.

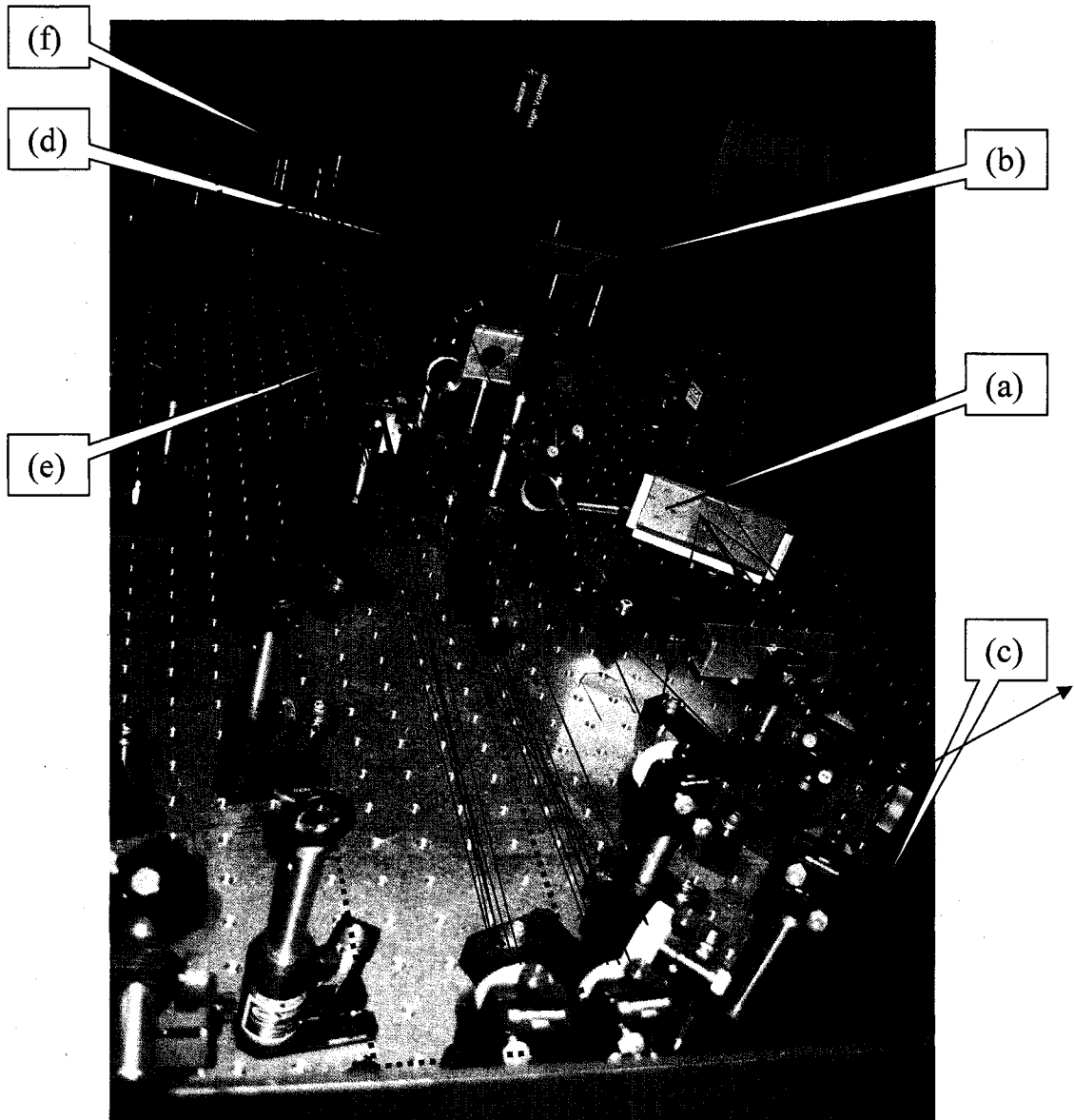


Figure 3.22. Layout of the pulse stretcher and the eight-pass preamplifier stage. (a), (b) and (c) dispersive grating, folding mirror and parabolic mirror of the pulse stretcher, respectively; (d) Pockel's cell serving as a pulse picker; (e) Ti:sapphire crystal in the eight-pass amplifier stage; (f) focusing mirrors for the pump beam.

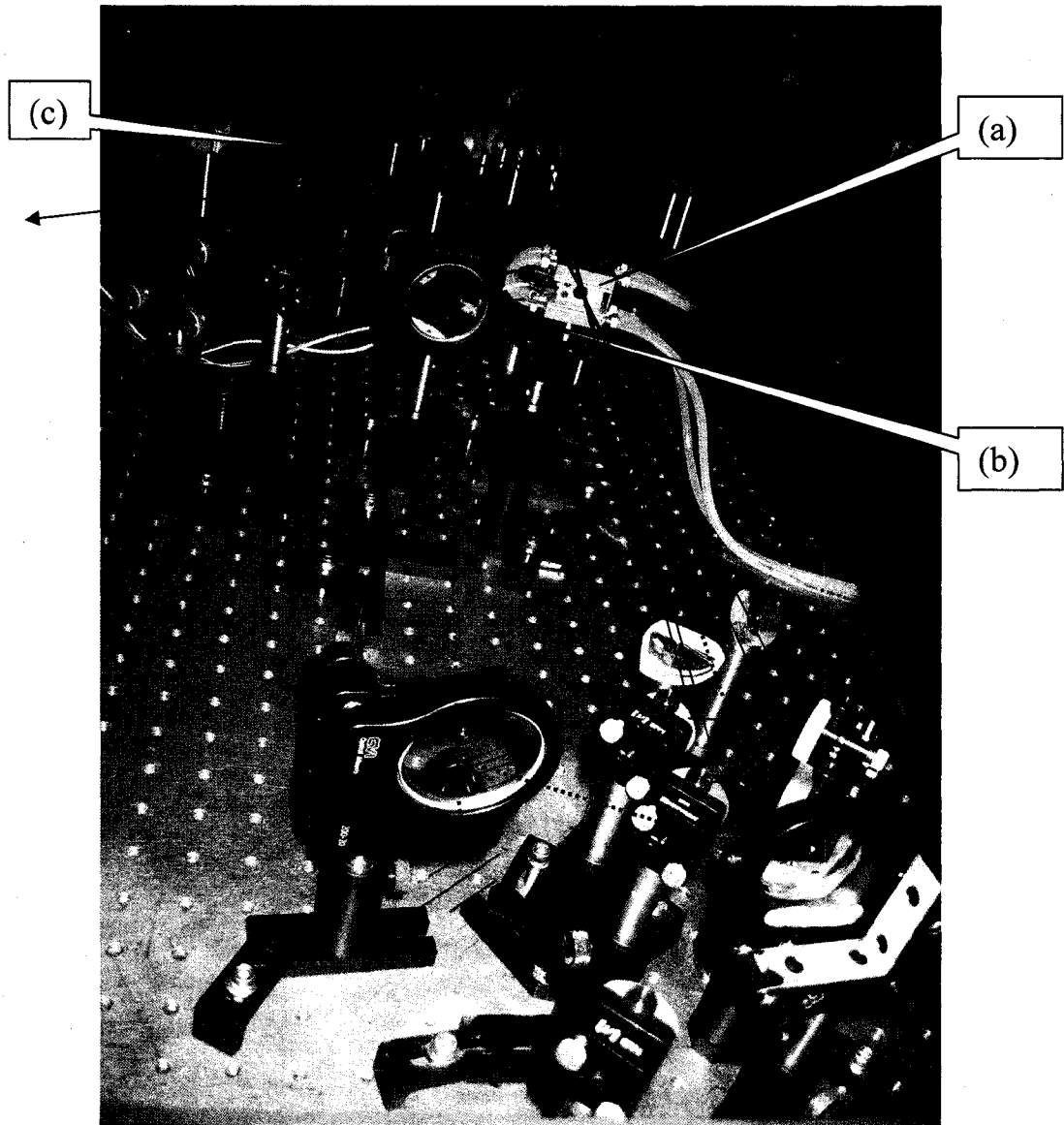


Figure 3.23. Layout of the pulse stretcher and the four-pass power amplification stage. (a), Ti:sapphire crystal in a thermal-electric cooling mount; (b) Beam splitter separating the pump beam so that the crystal is pumped from both sides; (c) Plano-convex lens slightly focusing the pumping beam.

## Summary

In summary, I have built a Terawatt amplification system based on CPA technique. Both the pulse stretcher and compressor adopt the all-reflective design with a near Littrow angle configuration. The Littrow configuration minimizes the reflection loss of high-order dispersion from the gratings, and the all-reflective design of the pulse stretcher/compressor minimizes the chromatic aberration and nonlinear optical effects. The amplification system consists of two stages of multi-pass amplifiers. Each amplifier uses a 0.25% doped, Brewster-cut Ti:sapphire crystal as gain media. Compared with the regenerative amplifiers, our multi-pass amplifier has the advantage of low dispersion and increased spectral throughput. The whole amplification system is pumped longitudinally with a 30-Hz, 800-mW Nd:YAG laser. The output pulse energy from this amplifier is 20 mJ, corresponding to a total gain of  $\sim 4 \times 10^7$  for the seed beam. The pulse duration is compressed back to 73 fs, yielding a 0.3-TW output peak power.

## **Chapter 4**

### **Results and Discussion**

In this chapter, a numerical evaluation of the diffraction integral obtained in the theoretical model is presented. Section 4.1 describes the Monte Carlo method --- the numerical technique used to calculate the diffraction integral, and shows the calculation results of the numerical simulation, including a detailed analysis of spatial and temporal intensity evolution of the ultrashort laser pulse passing through the diffractive beam shaping system

In order to justify the theoretical simulation of the ultrashort high-energy laser pulse beam shaping process, experimental investigation of the beam shaping system are performed. The high-power CPA laser amplification system facilitates the experimental studies of the beam shaping system at various energy levels ranging from 6 nJ to 20 mJ. The transmitted beam profiles through the laser beam shaping system are captured with a CCD camera, and the fluence distribution is compared with the theoretical curves obtained through numerical simulations. These experimental results are presented in section 4.2.

#### **4.1 Numerical simulation**

### 4.1.1 Low-energy pulse beam shaping

The diffraction integral deduced in the theoretical model was given as Equ. (2.25) in Chapter 2:

$$\begin{aligned}
 E(\xi_f, t') = & \int E_0 \exp(-\frac{1}{2}\xi^2) \exp(-(\frac{\Omega-\Omega_0}{\delta})^2) \\
 & \cdot \exp[-i\beta(\phi(\xi) \frac{\Omega-\Omega_0 n(\Omega_0)}{\Omega_0-\Omega_0 n(\Omega_0)} - \xi \xi_f \frac{\Omega}{\Omega_0})] \\
 & \cdot \exp[ik_m'(\Omega_0) \cdot t(\xi)(\Omega - \Omega_0)] \\
 & \cdot \exp[-\frac{1}{2} ik_m''(\Omega_0) \cdot t(\xi)(\Omega - \Omega_0)^2] \\
 & \cdot \frac{1}{i\lambda z_f} \exp(ik_v \frac{\xi_f^2 R_0^2}{2z_f}) \exp(i\Omega t') d\xi
 \end{aligned}$$

This equation derived for ultrashort laser pulse beam shaping needs to be solved numerically. I use the Monte Carlo method[76-78] to evaluate the diffraction integral. The Monte Carlo method is a widely used class of computational algorithms for simulating the behavior of various physical and mathematical systems. A deterministic method of numerical integration usually takes a number of evenly spaced sample points from the integrand function. For a multi-dimensional integration, the number of sampling points will increase exponentially with the degree of freedom in a given physical system. The Monte Carlo method provides an efficient way to avoid the exponential increase by generating random sampling points over the range of the integral. An optimization of this technique uses some algorithms to make the random points denser in regions of high contribution to the integral than from regions of low contribution.

For an integral of the form  $F = \int \int \dots \int f(u_1, u_2, \dots, u_n) du_1 du_2 \dots du_n$ , random vectors  $U_i(u_1, u_2, \dots, u_n)$  and a probability density function  $p_i(U)$  are introduced for each one of such vectors. Then the integral can be approximated by:  $F = \frac{P}{V} \sum_{i=1}^N f(U_i)$ , where

$P = \int p(x) dx$ , and  $V$  is the volume of the multidimensional space. The standard error for

Monte Carlo analysis is given by  $V \sqrt{\frac{\langle f^2 \rangle - \langle f \rangle^2}{N}}$ , where  $\langle f \rangle = \frac{1}{N} \sum_{i=1}^N f(U_i)$  and

$$\langle f^2 \rangle = \frac{1}{N} \sum_{i=1}^N f^2(U_i).$$

The efficiency of the Monte Carlo technique depends greatly on the sampling of random points. In some cases, uniformly distributed random points are not ideal for a quick convergence of the simulation. For example, using evenly distributed random points to integrate a sharply-peaked function could result in a very poor computational efficiency and convergence. In order to improve sampling, change of variables is often necessary. Given an integral  $I = \int_{y_1}^{y_2} f(y) dy$ , where  $f(y)$  is a fast varying function, the

variable can be transformed into  $y = g(x)$ , and the integral becomes  $I = \int_{x_1}^{x_2} f(g(x)) \frac{dg(x)}{dx} dx$ .

One can choose a transformation so that the variable gives a nearly flat distribution. A judging algorithm can also be used to identify the sharpest regions in an integrand so that more sampling points are generated in these regions.

For the two-dimensional diffraction integral we obtained in Equation (2.25), we perform the Monte Carlo numerical simulation as follows: 1. Identify the range of integrand variables  $\xi$  and  $\Omega$  where the random number will be placed; 2. Sample  $m$  points from this two-dimension space. Since the integrand is close to a Gaussian function, generate the random points in a Gaussian distribution; 3. Accept or reject the points based on criterion; 4. If accepted, add  $f(\xi, \Omega)$  to the total sum;

A detailed flow chart of the algorithm used in the numerical simulation is shown in Figure 4.1.

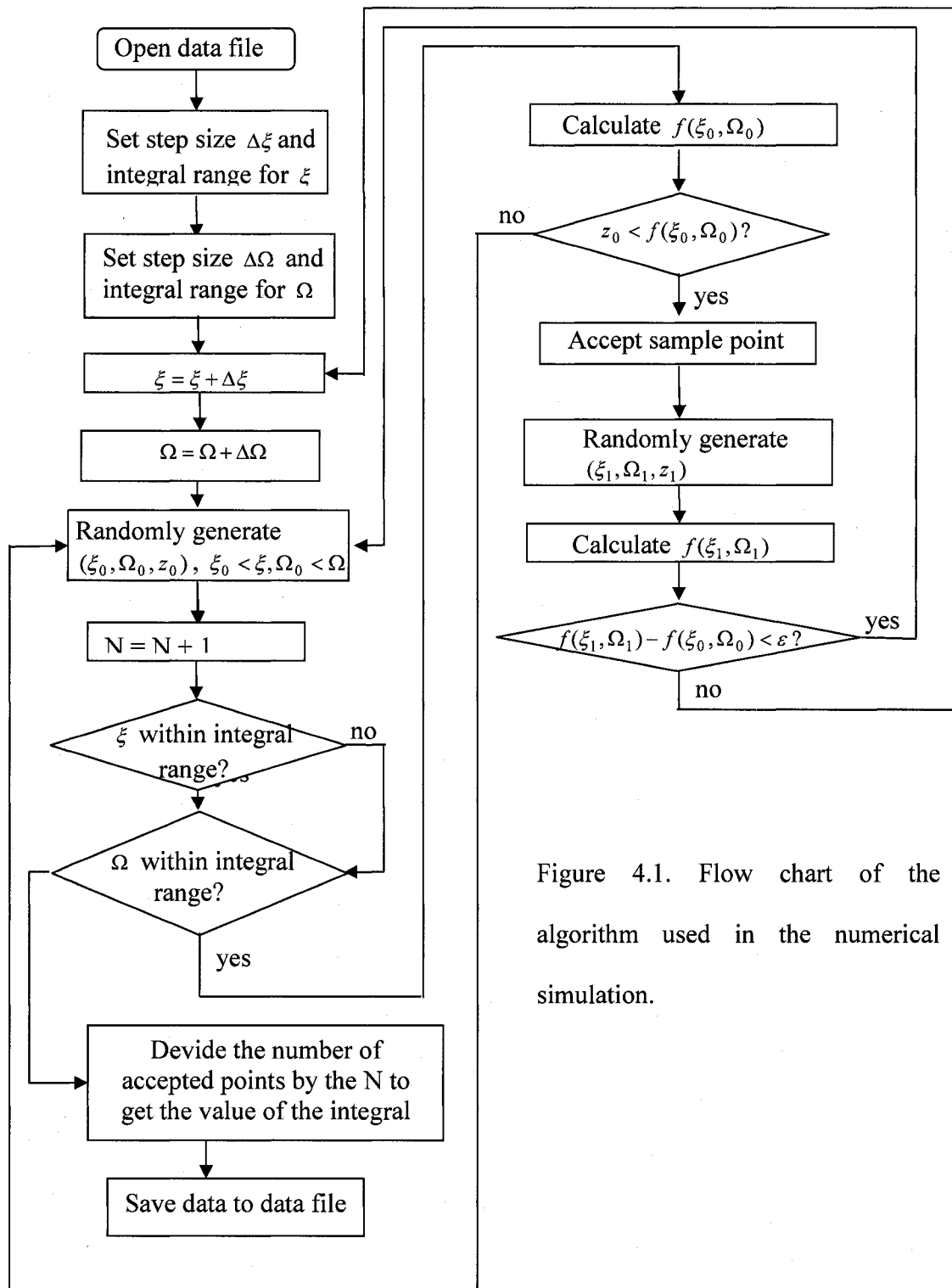


Figure 4.1. Flow chart of the algorithm used in the numerical simulation.

The optical material used in the beam shaping system is BK7 glass. The dispersion relationship expressed in terms of wave vector  $k$  as a function of angular frequency  $\Omega$  is given by  $k(\Omega) = k(\Omega_0) + k_1(\Omega_0)(\Omega - \Omega_0) + \frac{1}{2}k_2(\Omega_0)(\Omega - \Omega_0)^2 + \dots$ , where  $k_1(\Omega_0)$  and  $k_2(\Omega_0)$  are the coefficients of the Taylor series for  $k(\Omega)$ , respectively. The index of refraction  $n(\Omega_0)$  of BK7 glass and its first- and second-order derivatives with respect to the wavelength ( $n_{\lambda}'(\Omega_0)$  and  $n_{\lambda}''(\Omega_0)$ ) are known. Therefore, we can obtain the values of  $k_1(\Omega_0)$  and  $k_2(\Omega_0)$  with the following relationships:

$$\begin{cases} k_0 = \frac{n(\Omega_0)\Omega_0}{c} \\ k_1 = \frac{1}{c} \left( n(\Omega_0) - \lambda \left. \frac{dn}{d\lambda} \right|_{\Omega_0} \right) \\ k_2 = \frac{\lambda^2}{2\pi c^2} \lambda \left. \frac{d^2n}{d\lambda^2} \right|_{\Omega_0} \end{cases}$$

The central wavelength in the simulation is 800 nm, therefore,  $\Omega_0 = 2.355 \times 10^{15} \text{ s}^{-1}$ ,

and[79]

$$\begin{cases} n(\Omega_0) = 1.51077998 \\ \lambda \left. \frac{dn}{d\lambda} \right|_{\Omega_0} = 0.0158594599 \\ \lambda \left. \frac{d^2n}{d\lambda^2} \right|_{\Omega_0} = 0.0393046719 \times 10^6 \text{ m}^{-1} \end{cases}$$

Inserting (2.27) into (2.26), one can obtain the values of  $k_0(\Omega_0)$ ,  $k_1(\Omega_0)$  and  $k_2(\Omega_0)$ :

$$k_0 = 1.1859622 \times 10^7 \text{ m}^{-1}, k_1 = 4.9830684 \times 10^{-9} \text{ s} \cdot \text{m}^{-1} \text{ and } k_2 = 4.4506351 \times 10^{-26} \text{ s}^2 \cdot \text{m}^{-1}.$$

Next, the intensity profile of a 100-fs pulse passing through the beam shaping system is calculated. In the simulation, the radius of the incident beam is 5 mm, and that of the desired output beam is 200  $\mu\text{m}$ . The intensity profile [80] as a function of radius

and time in the target plane is shown in Figure 4.2. Figure 4.3 presents three cross-sections of the pulse profile along the spatial axis in order to show the peak separation more clearly. In Figure 4.3, the zero point of the local time at the target plane is defined to be the time when the pulse front reaches the target plane. Therefore, Fig 4.3(a) corresponds to the pulse's spatial profile when the pulse front reaches the target plane. Figure 4.3(b) and 4.3(c) shows the spatial profiles at earlier times ( $t = -0.1 ps$  and  $t = -0.35 ps$ ) prior to the arrival of the pulse at the target plane. Negative time means that the tail part of the pulse front has not arrived at the target plane yet.

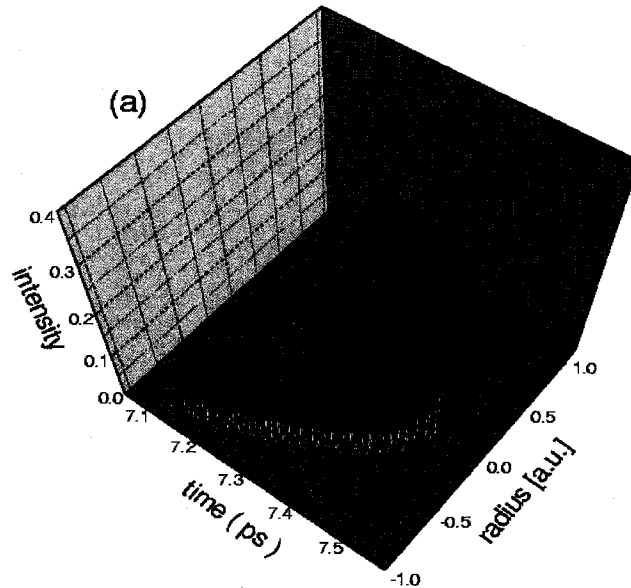


Figure 4.2. Intensity profile of the pulse at the target plane as a function of time and radius. The pulse front is curved due to the Propagation Time Delay (PTD) and broadened due to the Group Velocity Dispersion (GVD).

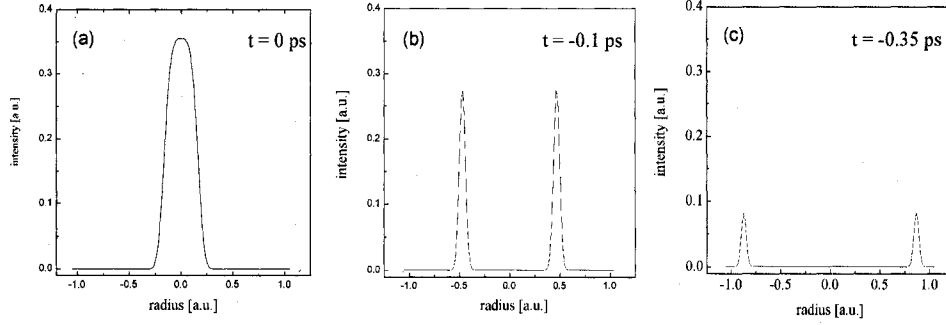


Figure 4.3. Spatial profiles of the laser pulse at different times: (a)  $t = 0$ , (b)  $t = -0.1 ps$ , and (c)  $t = -0.35 ps$ .

From the three dimensional intensity profile in Figure 4.2 one can see that the pulse front is strongly curved, which is due to the Propagation Time Delay (PTD). Since the path length of the beam in the beam shaping element changes laterally with the thickness of the optical media, the pulse front will be delayed with respect to the phase front. PTD depends on two factors: optical path length in the medium and the first order derivative of  $k(\Omega)$ . Using the dispersion of the optical material, the spectrum of the form of  $E_{z=z_0}(t) = E_0(x) \exp(-\Gamma t^2) \exp(i\omega_0 t)$  propagating along z-axis in an optical medium at position  $z = z_0$  can be expressed as :

$$E_{z=z_0}(\omega) = E_0 \exp[ik(\omega_0)z_0] \exp[-ik'(\omega_0)(\omega - \omega_0)z_0] \exp\left[-\frac{1}{4\Gamma} + \frac{1}{2}ik''(\omega_0)(\omega - \omega_0)^2\right].$$

In the time domain, the profile of the pulse is given by:

$$E_{z=z_0}(t) = \sqrt{\frac{\Gamma(z_0)}{\pi}} E_0 \exp\left[i\omega_0\left(t - \frac{z_0}{v_p(\omega_0)}\right)\right] \exp\left[-\Gamma(z_0)\left(t - \frac{z_0}{v_g(\omega_0)}\right)^2\right],$$

where  $\frac{1}{\Gamma(z_0)} = \frac{1}{\Gamma} + 2ik''(\omega_0)z_0$ , and  $v_p(\omega_0) = \frac{\omega_0}{k}$  and  $v_g(\omega_0) = \left.\frac{d\omega}{dk}\right|_{\omega_0}$  are the phase velocity and group velocity of the pulse, respectively. From the above equation, One can see that  $k'(\omega_0)$  causes the propagation time delay. This equation also shows that the group

velocity dispersion in the  $\frac{1}{\Gamma(z_0)}$  term will cause the pulse broadening. These features are all reflected in the pulse intensity profile shown in Figure 4.2.

The spatial intensity distribution deviates significantly from a top-hat profile. Figure 4.4(a) shows the peak intensity as a function of the normalized radius in the target plane. The intensity drops down from the center to the outer area. This can be explained as follows: for each wavelength component, the beam shaping system will shape the beam into a top-hat profile, and the only difference is the size of the top-hat profile due to the scaling feature of the beam shaping system. For an ultra short pulse input, the higher output intensity in the central region results from the superposition of all the top-hat profiles corresponding to different wavelength components. Figure 4.4(b) shows the relationship of pulse duration versus radius in the target plane. As discussed above, the group velocity dispersion causes various pulse broadening depending on the lateral position in the cross section of the laser beam.

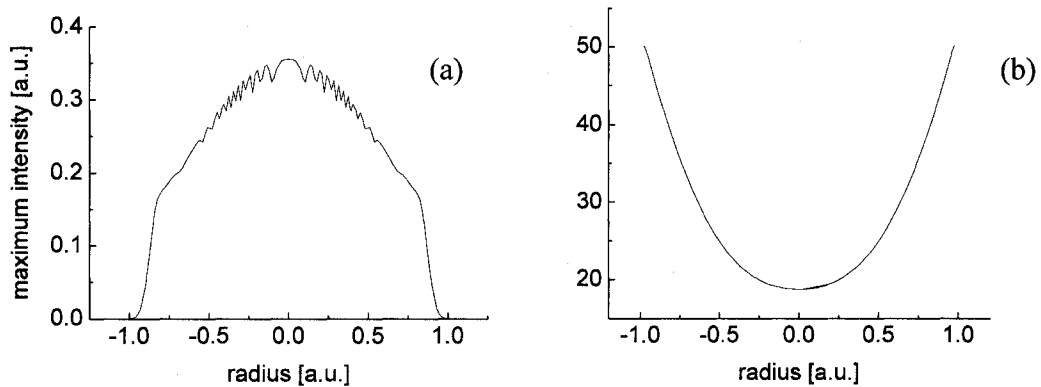


Figure 4.4. (a) Peak intensity of the pulse front as a function of radius in the target plane, and (b) pulse duration time in the target plane as a function of radius.

Although the peak intensity profile deviates significantly from a top-hat profile, we find that the fluence still keeps a flat-top profile. The fluence profile is shown in Figure 4.5[81].

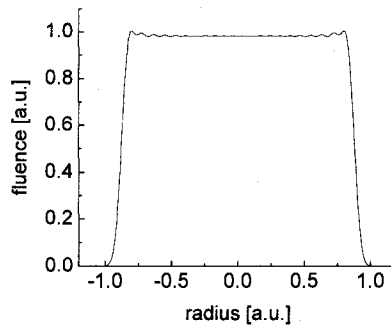


Figure 4.5. Fluence profile through the target plane as a function of radius.

The fluence profile shows that although the beam shaping system was originally designed for CW laser beams, it also works well for ultrashort laser pulses.

#### 4.1.2 Alignment and scaling errors

The effects of misalignments on the beam profile are also studied[81]. In case one, the incident laser beam is not aligned exactly along the optical axis of the beam shaping system, that is, a small lateral deviation is added. Theoretically, this is done by replacing  $\xi$  with  $\xi - \delta$  in Equation (2.25), where  $\delta$  is the relative lateral deviation of the laser beam. In the calculation,  $\delta$  is 10% of the original laser beam diameter. Figure 4.6 shows the corresponding tilt of the output beam profile.

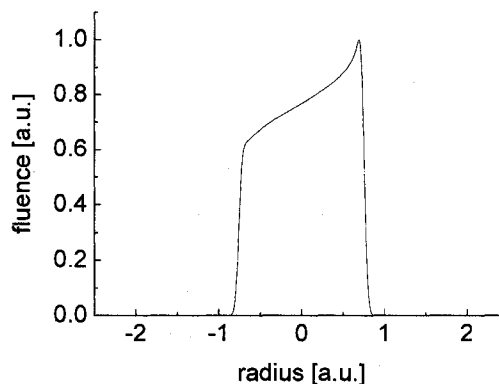


Figure 4.6. Fluence profile when the input beam is off-center by 10%.

The second alignment error corresponds to a deviation in the input beam size. The parameter  $\beta$  is determined by the product of both the input and output beam size. For a designed beam shaper, the input beam size is fixed, therefore the deviation in input beam size can cause distortion in the output top-hat profile. The effects of input beam size 10% larger or smaller than the designed value are shown in Figs. 4.7(a) and (b), respectively. For larger beam size, the profile is lower and wider, but it is higher and narrower for smaller input laser beam. The central part of the flat top sinks when the input beam size is larger and humps when the input beam size is smaller.

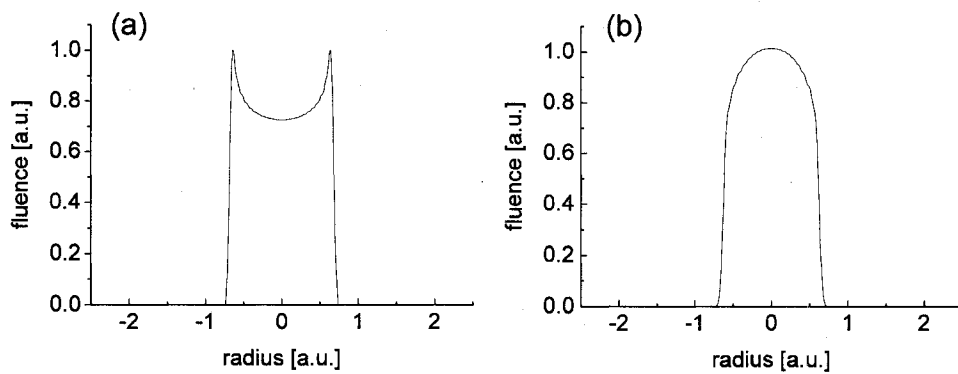


Figure 4.7. Effects of input beam size 10% larger (a) or smaller (b) than the designed value, respectively.

Next, the defocusing effects are calculated in the target plane before or after the focusing plane of the Fourier lens by 2.5% of the focusing length. As shown in Figs. 4.8 (a) and (b), in the case of positive defocusing (the distance between the Fourier element and the target plane is shorter than the focal length of the Fourier lens), the top hat profile is still obtained, but the flat top humps compared with the normal top-hat profile. When the target plane is negatively defocused (the distance between the Fourier element and the

target plane is longer than the focal length of the Fourier lens), a tilting edge appears on the edge of the flat-top fluence profile.

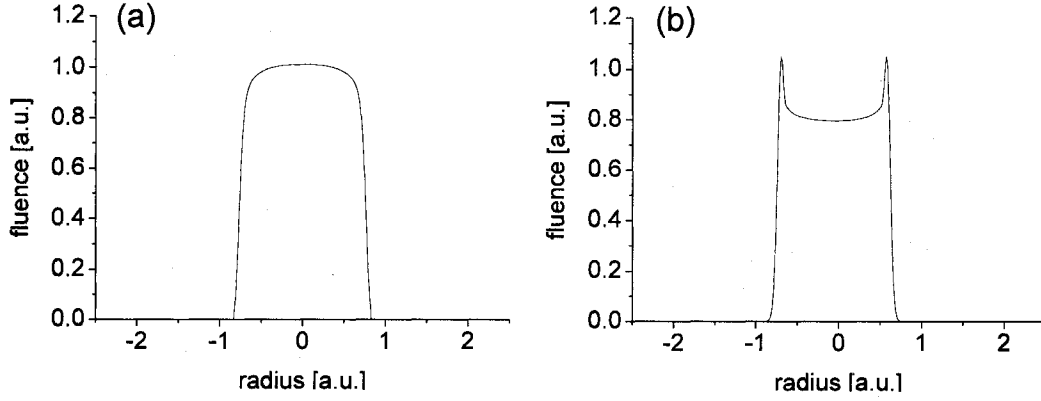


Figure 4.8. Defocusing effects: (a) before and (b) after the focusing plane of the Fourier lens by 2.5% of the focusing length.

#### 4.1.3 Medium- and high-energy pulse beam shaping

For higher-power ultrashort laser pulses, when the nonlinear self-phase modulation effect is considered, the diffraction integral is given Equation 2.29 in Chapter 2:

$$\begin{aligned}
 E(\xi_f, t') = & \iint E_0 \exp(-\frac{1}{2} \xi^2) \exp(-(\frac{\Omega - \Omega_0}{\delta})^2) \\
 & \cdot \exp[-i\beta(\phi \frac{\Omega - \Omega_0 n(\Omega_0)}{\Omega_0 - \Omega_0 n(\Omega_0)} - \xi \xi_f \frac{\Omega}{\Omega_0})] \\
 & \cdot \exp[ik_m'(\Omega_0) \cdot t(\xi)(\Omega - \Omega_0)] \\
 & \cdot \exp[-\frac{1}{2} ik_m''(\Omega_0) \cdot t(\xi)(\Omega - \Omega_0)^2] \\
 & \cdot \frac{1}{i2z_f} \exp(-ik_v \frac{(\xi_f R_0)^2}{2z_f}) \exp(i\Omega t') \\
 & \cdot \exp(i\psi_{NL}) d\Omega d\xi \quad ,
 \end{aligned}$$

Numerical simulation is also performed for this equation[81]. For BK7 glass used in the experiment, the GVD parameter is  $k_m'' = 446 \text{ fs}^2 / \text{cm}$ , and the nonlinear index coefficient of BK7 glass is  $n_2 = 3.71 \times 10^{-16} \text{ cm}^2 / \text{W}$  [82]. The duration time of the pulse passing through the beam shaping system is 100 fs with a peak power ranging from

$1.5 \times 10^{11} W/cm^2$  to  $5 \times 10^{12} W/cm^2$ . The calculated intensity profiles at the target plane as a function of radius and local time at the target plane of the beam shaping system are shown in Figure 4.9.

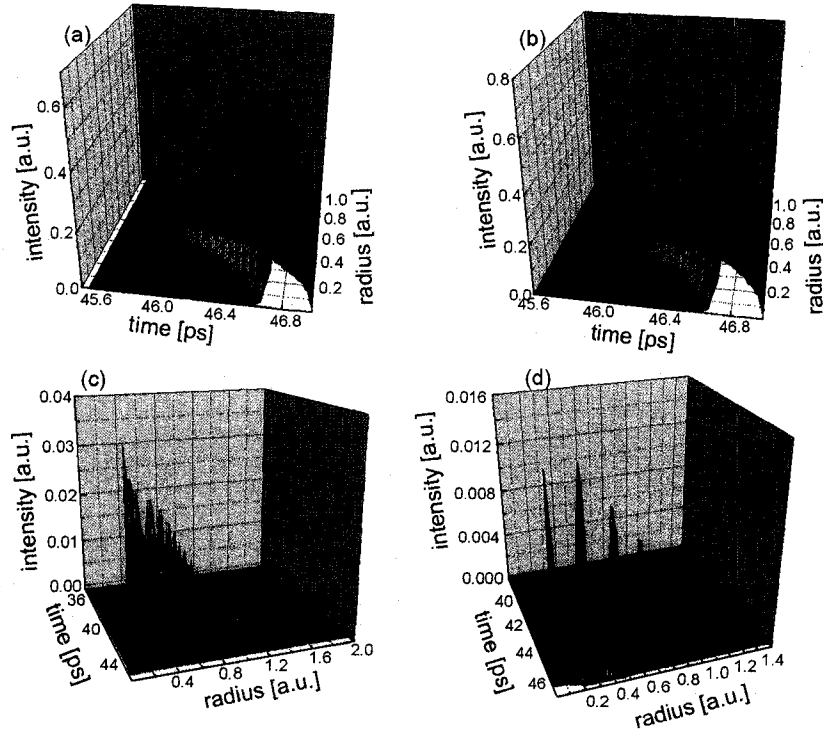


Figure 4.9. Intensity profiles as function of radius and local time at the target plane. The laser pulse duration is 100 fs, and the peak power in each figure is a)  $1.5 \times 10^{11} W/cm^2$ , b)  $5 \times 10^{11} W/cm^2$ , c)  $2.5 \times 10^{12} W/cm^2$  and d)  $5 \times 10^{12} W/cm^2$ .

The energy fluence through the target plane of the beam shaping system is also calculated. Figure 4.10 shows the corresponding fluence curves as a function of the radius in the target plane.

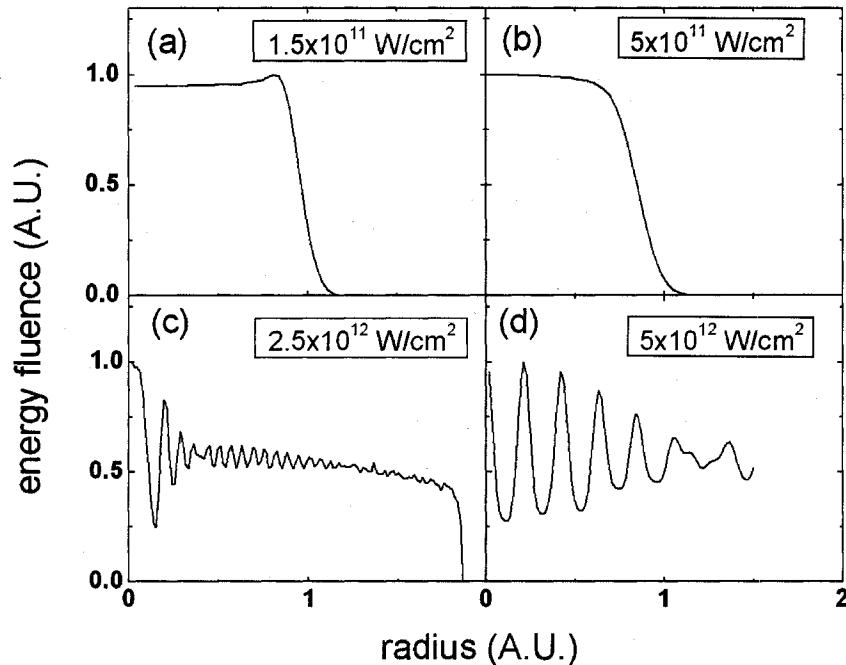


Figure 4.10. Integrated fluence in the target plane. The pulse duration is 100 fs, and the beam diameter is 10 mm. The pulse peak intensity is: a)  $1.5 \times 10^{11} \text{ W/cm}^2$ , b)  $5 \times 10^{11} \text{ W/cm}^2$ , c)  $2.5 \times 10^{12} \text{ W/cm}^2$ , and d)  $5 \times 10^{12} \text{ W/cm}^2$ .

The theoretical simulation shows that at relative low-energy levels ( $<10$  mJ), the top-hat fluence profile is still maintained, but the sharpness of the top-hat profile is reduced (Figure 4.10(b)). As the pulse energy increases, the flat-top is destroyed by the self-phase modulation (Figure 4.10(c) and 4.10(d)). A series of diffraction rings arise at the target plane. The self-phase modulation will result in a phase increment from the center to the edge of the beam, as a result, the intensity profile in transverse wave vector space shows peaks and valleys resulting from constructive and destructive interference. A series of spikes are visible in the fluence curve. The number of bright rings can be estimated from the maximum phase difference  $\Delta\phi_r$  between the center and the edge of

the beam. The number of bright rings is given by the integer closest to but smaller than  $\frac{\Delta\phi_r}{2\pi}$ . For a 100-mJ, 100-fs pulse,  $\Delta\phi_r \approx 44$ . The simulation result therefore shows approximately 7 interference rings (Figure 4.10(d)).

## 4.2 Experimental Data

Theoretical simulations of the pulse intensity profile at different energy levels indicate that at relatively low energy levels (a few milliJoules) this beam shaping system can reshape a Gaussian beam into a top-hat profile without being affected by dispersion and nonlinear phase modulation effects. However, as the pulse energy increases, the sharpness of the top-hat profile will be reduced. When the pulse energy is more than 40 mJ, the flat-top profiles will be completely destroyed.

In order to confirm the theoretical simulations of the reshaped intensity distributions, we send a laser beam with various energy levels ranging from 6 nJ to 20 mJ through the beam shaping system. The reshaped beam profiles are in reasonable agreement with the theoretical calculations.

### 4.2.1 Low-energy pulse beam shaping

For relatively low-energy ultra short laser pulse beam shaping, a Ti:sapphire pulsed laser oscillator (Spectra-Physics, Tsunami) is used as the beam source. It is operating at 800 nm wavelength. The bandwidth of the input pulse is 40 nm measured with a spectrum analyzer. The pulse duration time is 100 fs, and the repetition rate of the pulsed laser beam is 80 MHz. The laser is running at an average power of 450 mW. Therefore, the energy of the laser beam is 6 nJ per pulse. The pulsed laser beam is sent

through the diffractive beam shaping system, and the output intensity profile is captured with a CCD camera. Figure 4.11 shows the three-dimensional beam profile of the incident Gaussian beam and the output top-hat profile captured at the target plane of the beam shaping system.

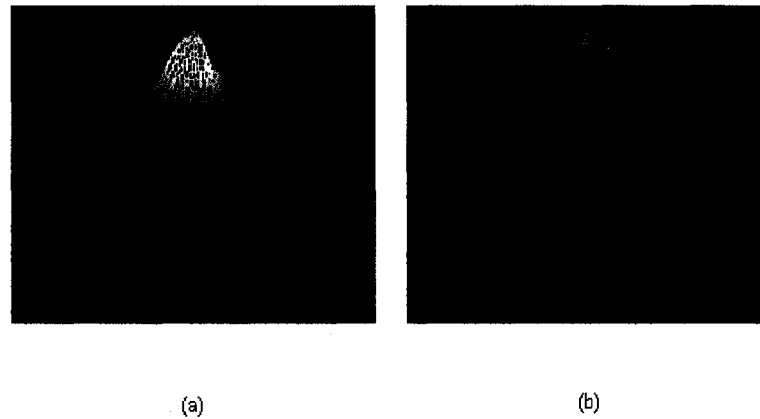


Figure 4.11. (a) Input laser beam with a Gaussian profile, (b) output beam with a flat-top profile.

The profile shown in Figure 4.11(a) is a focused Gaussian laser beam. It was captured at the focal point of the Fourier lens while the phase delay element was removed from the beam shaping system. After the beam shaper was inserted between the beam expander and the Fourier lens, the intensity distribution was changed into a more flat-top beam profile shown in Figure 4.11(b).

The beam shaping system was originally developed for CW laser beams. In order to confirm that this beam shaping system can reshape a Gaussian beam profile into a homogeneous intensity distribution for low-power ultrashort laser pulse as well as for CW laser beam. It is necessary to compare the reshaped beam profiles for ultrashort laser pulse and for CW laser beam. The Ti:sapphire laser used in the experiment is pumped with a diode-pumped solid state 532 nm laser (Millennia, Spectra Physics). During

operation, the Tsunami laser can lose mode-lock if the pumping beam is blocked. When the pump beam is released into the Tsunami laser again, the output properties of Tsunami laser will not change except that the beam is a CW instead of a pulsed laser beam.

In our experiment, we let the Tsunami laser stop mode-locking and didn't find any change in the intensity distribution at the target plane of the beam shaping system. This confirmed that at very low energy levels, the diffractive beam shaping system has the same effect on ultrashort laser pulses as on CW laser beams. This can be understood if we consider the bandwidth of the laser used in these experiments. The spectral bandwidth is 40 nm with a center wavelength of 800 nm. As a result, the variation of  $\beta$  over the spectrum of the pulse is only 5%, and the difference in the final top-hat profile between the pulsed- and CW-input is too small to observe. However, when the pulse is extremely short, the broad bandwidth will result in a large variation of  $\beta$ , and thus the final top-hat intensity profile should be altered considerably.

In micromachining applications, the spatial-temporal intensity distribution of a laser beam is not the most straightforward way to measure the energy deposited onto a specific area of the target material. The integral intensity, i.e. Fluence, is a direct measure of the strength of the radiation field. Fluence is defined as energy per unit area. Its unit is J/m<sup>2</sup>. The Fluence through the center line of the top-hat beam profile is analyzed with the laser beam diagnostic software. Figure 4.12 shows the normalized energy-fluence profile along the central axis on the target plane of the beam shaping system compared with the theoretical calculation results.

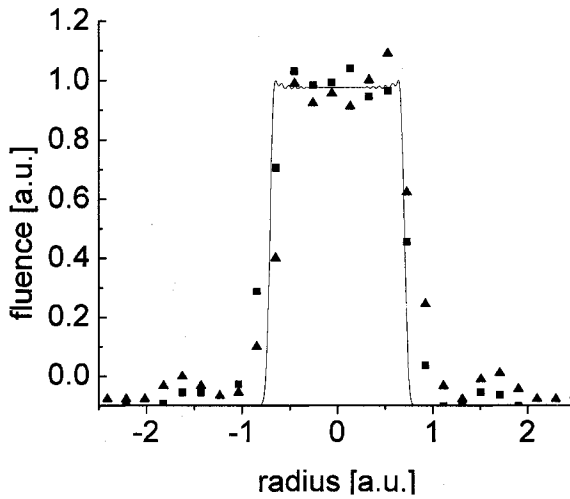


Figure 4.12. Normalized energy-fluence profile along the central axis of the target plane. The theoretical result is plotted as solid curves, and the two sets of experimental data are plotted as filled squares and triangles.

#### 4.2.2 Alignment and scaling errors

Diffraction beam shaping method is inherently sensitive to alignment errors and variations in the input beam properties such as beam size deviation, beam decentering with respect to the optical axis, target plane defocusing and so on. We also studied these alignment error effects in our experiment.

First, the incident laser beam is not aligned exactly along the optical axis of the beam shaping system, that is, a small lateral deviation is added. Theoretically, we do this by replacing  $\xi$  with  $\xi - \delta$  in the diffraction integral. In our experiment, the incident beam's radius is 5 mm, and the lateral misalignment is 0.5 mm. The theoretical curve

along with the experimental data is shown in Figure 4.13. The off-axis incidence in the beam shaping system results in a considerable distortion of the top-hat profile.

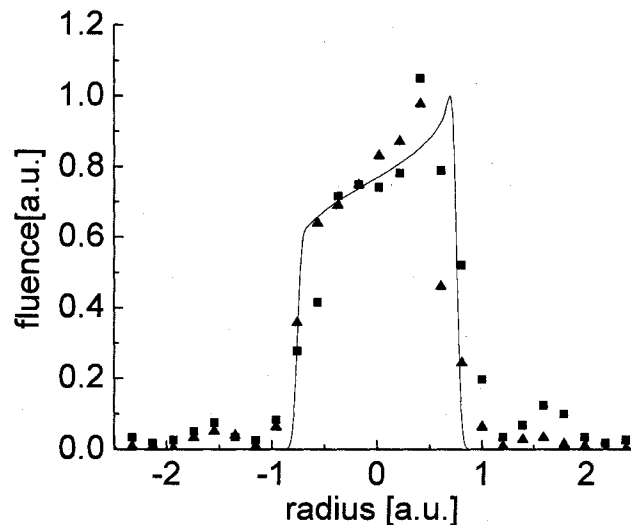


Figure 4.13. Effect of lateral misalignment of 10% of the laser beam diameter. The theoretical result is plotted as solid curves, and the two sets of experimental data are plotted as filled squares and triangles.

We also studied the effect of input beam size deviation on the output beam profile. The scaling parameter  $\beta$  is determined by the product of both input and output beam diameters. However, for a given beam shaper, the input beam size is fixed, therefore, the deviation in input beam size can cause distortion in the output top-hat profile. The effects of input beam size 10% larger and smaller than the designed value are shown in Figures 4.14(a) and 4.14(b), respectively. For a larger beam size, the profile becomes lower and wider, and on the contrary, higher and narrower for smaller input laser beam. The central part of the top hat sinks when the input beam size is larger and humps when the input

beam size is smaller. This can be explained using a geometrical optics representation of the beam shaping process. In this diffractive optical element beam shaping system, the incident collimated rays of the laser beam are bent in a way that the rays near the edge of the beam shaping element are bent more than those near the center, and therefore the energy of the beam is concentrated towards the optical axis so that the Gaussian beam will evolve into a top-hat beam profile at the focal plane of the Fourier lens provided that the bending angles of the rays in different regions of the beam are well adjusted. When the diameter of the input laser beam is smaller than that of the beam shaping element, there will be more rays at the edge of the beam bent towards the center. That means more energy is concentrated at the center of the target plane, therefore, the central part of the top-hat profile will hump. In the opposite case, the top-hat profile will sink in the central part if the beam is larger than the designed size.

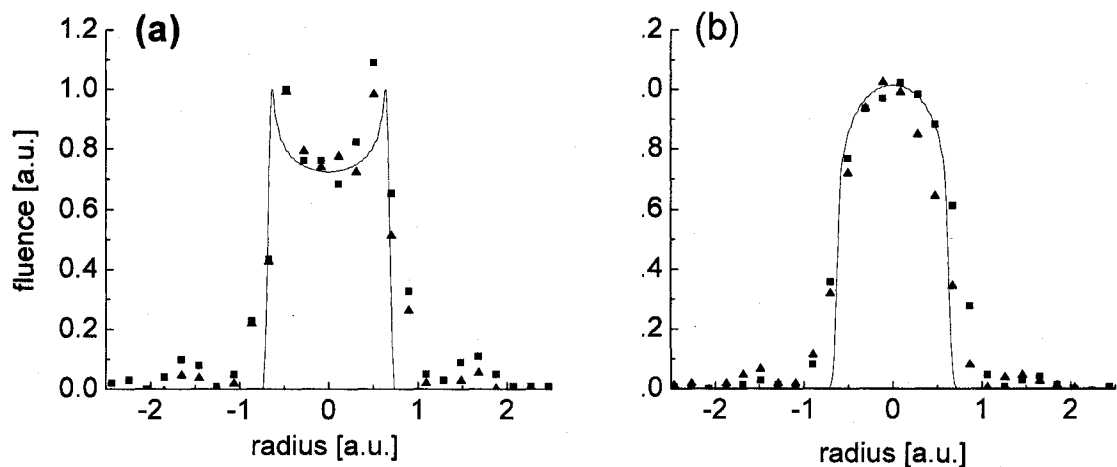


Figure 4.14. Effects of beam size deviation. (a) input beam size 10% larger than the designed value, (b) input beam size 10% smaller than the designed value. The theoretical result is plotted as solid curves, and the two sets of experimental data are plotted as filled squares and triangles.

Besides the fluence distribution in the target plane, we also studied the beam profiles in front and behind the focusing plane of the Fourier lens. Defocusing effects of 2.5% of the focusing length are calculated in the target plane before and after the focal plane of the Fourier lens. In the former case, the top hat profile is still obtained, except that the sharpness of the top-hat is reduced as shown in Figure 4.15(a). And in the latter case, a tilt edge appears on the top-hat profile as shown in Figure 4.15(b). This manifests the evolution of the energy fluence profile while the laser beam propagates through the focal plane of the Fourier lens, that is, the top-hat energy fluence profile only exists at a certain range around the target plane. This is because the phase front of the laser beam is curved and the energy within the laser beam will be redistributed while traveling along the direction of the optical axis.

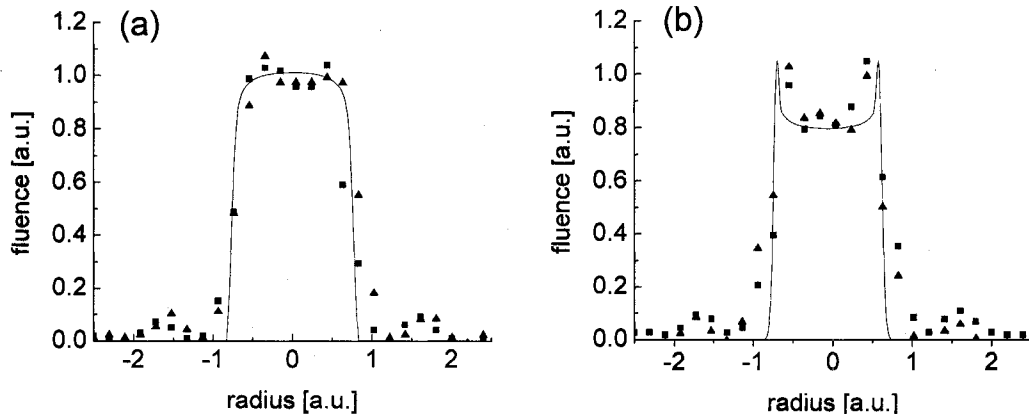


Figure 4.15. Defocusing effects. (a) intensity profile before the focusing plane of the Fourier lens by 2.5% of the focal length, (b) intensity profile after the focusing plane of the Fourier lens by 2.5% of the focal length, The theoretical result is plotted as solid curves, and the two sets of experimental data are plotted as filled squares and triangles.

### 4.2.3 Medium- and high-energy pulse beam shaping

The CPA laser amplification system enables us to study the beam shaping system for high-energy ultrashort laser pulses. After being amplified by the first stage of the laser amplifier, the pulse energy reaches 1 mJ. The pulse duration is compressed back to 80 fs after passing through the grating-based pulse compressor. This 80-fs, 1-mJ pulsed laser beam is expanded to 10 mm in diameter and switched into the diffractive beam shaping system. We record the output beam profile at the focal plane of the Fourier lens with the CCD camera. Figure 4.16 shows the experimental data of the fluence profile along the central axis of the target plane together with the calculated fluence curve. The captured beam profile agrees with the theoretical top-hat distribution. This result confirms the validity of this beam shaping system for the application of ultrashort laser pulses at millijoule energy level.

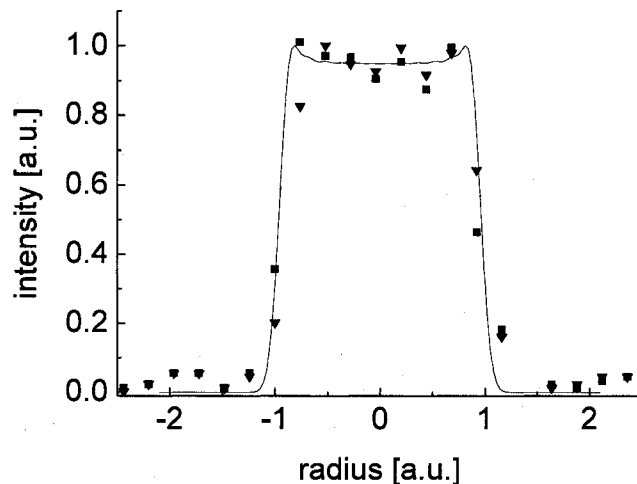


Figure 4.16. Fluence profile along the central axis of the target plane for a 1-mJ, 80-fs laser pulse passing through the beam shaping system. The theoretical result is plotted as solid curves, and the two sets of experimental data are plotted as filled squares and triangles.

The final output of the laser amplifier system reaches 20 mJ with a pulse duration of 70 fs. Our theoretical calculation indicates that at this energy level, the output beam profile from the beam shaping system starts to deviate from the top-hat profile due to the nonlinear self phase modulation. The sharpness of the top-hat fluence profile will be reduced. The experimental data agree with the fluence profile calculated from the diffraction integral including the self-phase modulation effect. Figure 4.17 shows the reshaped beam profile of a 20-mJ, 70-fs pulsed laser beam along the central axis on the target plane of the beam shaping system.

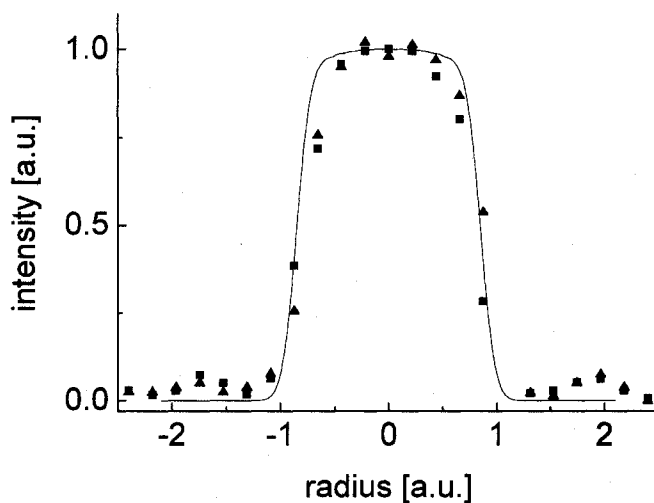


Figure 4.17. Fluence profile along the central axis of the target plane for a 20-mJ, 70-fs laser pulse passing through the beam shaping system. The theoretical result is plotted as solid curves, and the two sets of experimental data are plotted as filled squares and triangles.

## Summary

In conclusion, I have performed numerical simulations to obtain the spatio-temporal intensity distribution of the pulse front and the energy fluence profile through

the target plane of the beam shaping system. The calculation result indicates that this beam shaping system can work well when the peak power of the laser pulse is below a certain level ( $<20$  mJ). As the pulse energy increases, the top-hat fluence profile will be destroyed due to nonlinear self-phase modulation.

Experimental studies of the beam shaping system for ultra short laser pulses at various energy levels confirm that although this beam shaping system was originally developed for CW lasers, it can work well for ultra short laser pulses of several millijoules, an energy level frequently used in many micro-machining technologies. I also studied the influence of alignment error and variations in the input beam on the reshaped beam profile. The experimental results indicate that the diffractive beam shaping system is sensitive to the optical alignment as well as the input beam size variation.

## **Chapter 5**

### **Conclusion and Future Work**

#### **5.1 Conclusion**

In this thesis, a diffractive beam shaping system originally developed for continuous wave lasers is studied for ultrashort high-power laser pulses. A diffraction-based theoretical model is developed to simulate the reshaped intensity profiles for a 100-fs pulse with various energy levels. Both temporal evolution and spatial intensity distribution of the pulse propagating to the target plane of the beam shaping system are calculated. Numerical simulation shows that after passing through the beam shaping system, the pulse front is significantly curved due to the propagation time delay, and the pulse duration time through the target plane is broadened because of the group velocity dispersion. However, for relatively low-energy pulses (on the order of millijoules), although the intensity distribution is changed considerably, the fluence top-hat profile is well maintained. This feature extends the application of this beam shaping system into the regime of ultrashort laser pulses. While millijoule pulses are commonly used in the micromachining technology, the adaptability of this diffractive beam shaping system is greatly improved.

Theoretical calculation also shows the limit when the top-hat profile starts to degrade. For very high-energy laser pulses (>40 mJ per pulse), the homogeneous fluence profile, as well as the intensity distribution, is destroyed due to the nonlinear self-phase modulation.

A terawatt CPA laser amplification system was built in order to verify the theoretical simulation in experiment. The output of his CPA amplifier is operating at 30 Hz repetition rate with a pulse energy of 20 mJ/pulse. The compressed pulse duration is 70 fs, resulting in a pulse peak power of 0.3 TW.

This thesis also presents an experimental study of the beam shaping system for ultrashort high-power pulses generated in a CPA laser amplifier. Experimental results are in reasonable agreement with the numerical simulation of the reshaped fluence profiles at various energy levels from 6nJ to 20 mJ. The experimental results confirm the validity of this diffractive beam shaping system for ultrashort pulses with an energy lower than 20 mJ/pulse.

## **5.2 Future work**

Applications of the ultrashort pulse beam shaping system in micromachining technology can be studied further as a future work. Since the mechanism used in the diffractive beam shaping system is based on phase-shifting technique, the propagation properties of the reshaped laser beam will affect, to a large extent, the treatment conditions and results in a micromachining system. Therefore, the beam focusing, contour and projection for the reshaped top-hat laser beam need to be considered for the purpose of practical applications. On the other hand, in many applications such as pulsed

laser-plasma deposition of thin films, laser-driven microwelding and micropatterning, the interaction of the reshaped high-power laser radiation with matter (e.g. the process of plasma formation) also needs to be studied due to the unique properties of the homogenized high-power laser beam. Therefore, the future work of the ultrashort, high-power laser beam shaping system can be categorized into two major directions: (1) investigation of the beam control techniques, and (2) study of the interaction between the reshaped laser radiation and matter.

In this thesis, the CPA laser amplifier is used to study the beam shaping system for ultrashort high-power laser pulses. However, this high-power laser amplification system can be used for much more than the beam shaping study. As a future work, the amplified terawatt laser beam is going to be used to generate pulsed x-ray on a femtosecond time-scale.

X-rays are extremely useful in the study of the atomic structures because they can interact with core electrons directly. A pulsed x-ray on a femtosecond time-scale is especially desirable due to its high temporal resolution so that it can be used in the research of the atomic dynamics, such as the dynamics of a chemical reaction or the process of a phase transition.

A practical approach to generate femtosecond x-ray pulses is to create a high-intensity plasma by focusing a terra-watt laser beam onto a metal surface. The duration of the driven laser pulses is on a femtosecond time-scale, therefore, intense short-lived plasmas can be created during the period of the interaction between the laser and the metal. The electrons from the plasma will penetrate into the material, knocking out inner

shell electrons of the atoms. The recombination of the outer shell electrons and the core holes results in the  $K_{\alpha}$  x-ray emissions.

Another scheme to generate soft x-rays using the terawatt femtosecond laser pulses is high-order harmonic generation in gases. Harmonic radiation can be generated by focusing the terawatt infrared laser beam into the gas which flows through a hollow fiber. The photon energies of the harmonic pulses are in the soft x-ray regime, and can be used for time-resolved photoelectron spectroscopy of metals and semiconductors.

## BIBLIOGRAPHY

1. B. R. Frieden, "Lossless conversion of a plane laser wave to a plane wave of uniform irradiance," *Appl. Opt.* **4**, 1400-1403 (1965)
2. J. Kreuzer, "Laser light redistribution in illuminating optical signal processing systems," in *Optical and Electro-Optical Information Processing*, J.T. Tippet, D.A. Berkowitz, L.C. Clapp, C.J. Koester, and A. Vanderburgh, Jr., eds. (Massachusetts Institute of Technology Press), 365-369 (1965)
3. Kreuzer, US Patent 3,476,463, 1969: "Coherent light optical system yielding an output beam of desired intensity distribution at a desired equiphase surface."
4. D. R. Herriott, "Applications of laser light," *Sci, Am.* **219**, 140 (1968)
5. T. E. Horton and J. H. McDermit, "Design of a specular aspheric surface to uniformly radiate a flat surface using a nonuniform collimated radiation source," *J. Heat Transfer Trans. ASME* **C94**, 453-458 (1972)
6. P.W. Rhodes and D. L. Shealy, "Refractive optical systems for irradiance redistribution of collimated radiation: their design and analysis," *Appl. Opt.* **19**, 3545-3553 (1980)
7. I. S. Moskalev, V. V. Fedorov, and S. B. Mirov, "Multiwavelength mid-IR spatially dispersive CW laser based on polycrystalline  $\text{Cr}^{2+}:\text{ZnSe}$ ," *Optical Express* **12**, 4986-4992 (2004)

8. E. P. Walker, and T. D. Milster, "Beam shaping for optical data storage," in Laser beam shaping II, Fred M. Dickey; Scott C. Holswade; David L. Shealy; eds., Proc. SPIE **4443**, 73-92, (2001)
9. Fred M. Dickey, Scott C. Holswade, David L. Shealy, Laser beam shaping applications: optical engineering (Taylor and Francis Group, Boca Raton, Florida, 2006)
10. Saulius Juodkazis, Markas Sudzius, Vyngantas Mizeikis, and Hirokai Misawa, "Three-dimensional recording by tightly focused femtosecond pulse in LiNbO<sub>3</sub>," Appl. Phys. Lett. **89**, 062903 (2006)
11. E. B. Kley, M. Cumme, L. Witting, M. Thieme, W. Gabler, "Beam-shaping elements for holographic applications, micromachining and microfabrication" in Micromachining Technology for Micro-Optics, S. H. Lee, and E. G. Johnson eds, Proc. SPIE **4179**, 58-65 (2000).
12. Zhao, W.; Kim, J. H.; Palffy-Muhoray, Peter, "Z-scan measurement on liquid crystals using top-hat beams," in Nonlinear Optical Materials for Switching and Limiting, M. J. Soileau eds, Proc. SPIE **2229**, 131-147, (1994)
13. Bing Gu, Xian-Chu Peng, Tao Jia, Jian-Ping Ding, Jing-Liang He, and Hui-Tian Wang, "Determinations of third- and fifth-order nonlinearities by the use of the top-hat-beam Z scan: theory and experiment," Journal of the Optical Society of America B, **22**, 446-452 (2005)
14. Zhao, W.; Palffy-Muhoray, P., "Z-scan measurement of  $\chi^{(3)}$  using top-hat beams," Appl. Phys. Lett., **65**, 673-675 (1994)

15. W. Zhao and P. Palffy-Muhoray, "Z-scan technique using top-hat beams," *Appl. Phys. Lett.*, **63**, 1613-1615 (1993).
16. Shimada, Tsutomu; Kurnit, Norman A.; Sheik-Bahae, M., "Measurement of nonlinear index by a relay-imaged top-hat z-scan technique," in 27th Annual Boulder Damage Symposium: Laser-Induced Damage in Optical Materials, H. E. Bennett, A. H. Guenther, M. R. Kozlowski, B. E. Newnam, and M. J. Soileau eds, *Proc. SPIE*, **2714**, 52-60 (1995)
17. S.M. Metev, V.P. Veiko, "Laser Microshaping" in *Laser assisted micro-technology*, U. Gonser, R. M. Osgood, Jr., M. B. Panish, and H. Sakaki, eds. (Springer-Verlag, Berlin Heidelberg), 145-469 (1994)
18. J.L. Kreuzer, "Coherent light optical system yielding an output beam of desired intensity distribution at a desired equiphase surface", US Patent 3476463 (1969)
19. J. H. McDermit, T. E. Horton, "Reflective optics for obtaining prescribed irradiative distributinos from collimated sources. *App. Opt.* **13**, 1444–1450 (1974)
20. J. H. McDermit, "Curved reflective surfaces for obtaining prescribed irradiation distributions. Ph.D. Dissertation, University of Mississippi, Oxford, MS (1972)
21. J.A. Hoffnagle, C.M. Jefferson, "Design and performance of a refractive optical system that converts a Gaussian to a flattop beam", *Applied Optics*, **39**, 5488-5499, (2000)
22. P. W. Rhodes and D. L. Shealy, "Refractive optical systems for irradiance redistribution of collimated radiation: their design and analysis," *Appl. Opt.* **19**, 3545-3553 (1980)

23. W. Jiang, D. L. Shealy, and J. C. Martin, "Design and testing of a refractive reshaping system," in *Current Developments in Optical Design and Optical Engineering III*, R. E. Fischer and W. J. Smith eds., Proc. SPIE **2000**, 64–75 (1993)
24. D. Shafer, "Gaussian to flat-top intensity distributing lens," *Opt. Laser Technology* **14**, 159–160 (1982)
25. P. J. Sands, "Inhomogeneous lenses. IV. Aberrations of lenses with axial index distributions," *J. Opt. Soc. Am.* **61**, 1086-1091 (1971)
26. C. Wang and D. L. Shealy, "Design of gradient-index lens systems for laser beam reshaping," *Appl. Opt.* **32**, 4763-4769 (1993)
27. L.R. Romero, F. M. Dickey, "Lossless laser beam shaping," *J. Opt. Soc. Am. A* **13**, 751-760 (1996)
28. A. Walther, "The Fresnel approximation" in *The ray and wave theory of lenses*, Chapter 15.2, P. L. Knight, and A. Miller eds. (Cambridge University Press, 1995), pp. 149-151.
29. J. A. Hoffnagle., "A new derivation of the Dickey-Romero-Holswade phase function," in *Laser Beam Shaping VI*, F. M. Dickey, and D. L. Shealy eds, Proc. SPIE **5876**, 45-52 (2005)
30. Daniel Brown, "multi-aperture beam integrator/ method producing a continuously variable complex image," United State Patent 6909553, (2005)
31. X. Deng, X. Liang, Z. Chen, W. Yu, and R. Ma, "Uniform illumination of large targets using a lens array," *Appl. Opt.* **25**, 377-381 (1986)
32. F. M. Dickey, B. D. O'Neil, "Multifaceted laser beam integrators: general formulation and design concepts," *Opt. Eng.* **27**, 999-1007 (1988)

33. R. Tommasini, F. Lowenthal, J. E. Balmer, and H. P. Weber, "Iterative method for phase-amplitude retrieval and its application to the problem of beam-shaping and apodization," *Opt. Comm.* **153**, 339-346 (1998)
34. Yang, G. Z., Dong, B. Z., Gu, B.Y., Zhuang, J. and Ersoy, O. K., "Gerchberg-Saxton and Yang-Gu algorithms for phase retrieval in a nonunitary transform system: a comparison," *Appl. Opt.* **33**, 209 (1994)
35. Y. Zhang, B. -Z. Dong, B. -Y. Gu, and G. -Z. Yang, "Beam shaping in the fractional Fourier transform domain ," *J. Opt. Soc. Am. A* **15**, 1114-1120 (1998)
36. D. Brown, "Beam shaping with diffractive diffusers," in *Laser beam shaping: theory and techniques*, F. M. Dickey and S. C. Holswade eds. (Marcel Dekker Inc., New York), 249-271 (2000)
37. M. A. Webster, K. J. Webb, A. M. Weiner, J. Xu, and H. Cao, "Temporal response of a random medium from speckle intensity frequency correlations ," *J. Opt. Soc. Am. A* **20**, 2057-2070 (2003)
38. J. C. Dainty, "laser speckle and related phenomena," (Springer-Verlag, New York, 1984)
39. A. Walther, "The Raleigh-Sommerfeld integral" in *The ray and wave theory of lenses*, Chapter 14.1, P. L. Knight, and A. Miller eds. (Cambridge University Press, 1995), pp. 135-139.
40. A. Walther, "The Fraunhofer approximation" in *The ray and wave theory of lenses*, Chapter 15.1, P. L. Knight, and A. Miller eds. (Cambridge University Press, 1995), pp. 148-149.

41. A. Walther, "The Fresnel approximation" in *The ray and wave theory of lenses*, Chapter 15.2, P. L. Knight, and A. Miller eds. (Cambridge University Press, 1995), pp.149-151.
42. M. V. Fedoryuk, "The stationary phase method and pseudodifferential operators," *Russian Mathematical Surveys* **26**, 65-115 (1971)
43. L. A. Romero and F. M. Dickey, "Mathematical and physical theory of lossless beam shaping" in *Laser beam shaping: theory and techniques*, F. M. Dickey and S. C. Holswade eds. (Marcel Dekker Inc., New York), 36-40 (2000)
44. F. M. Dickey and S. C. Holswade, "Gaussian beam shaping: diffraction theory and design" in *Laser beam shaping: theory and techniques*, F. M. Dickey and S. C. Holswade eds. (Marcel Dekker Inc., New York), 119-162 (2000)
45. S. Zhang, Y. H. Ren, M. J. Kelley, and G. Lüpke, "Beam shaping of ultra-short laser pulses," *Proc. University/Government/Industry Microelectronics Symposium*, 60-63 (2001)
46. C. Sulem and P. L. Sulem, "Weakly nonlinear dispersive waves," in *Nonlinear Schrodinger Equations: self-focusing and wave collapse*, J. E. Marsden and L. Sirovich eds. (Springer-Verlag, New York), 3-7 (1999)
47. S. O. Konorov, D. A. Sidorov-Biryukov, I. Bugar, D. J. Chorvat, V. I. Beloglazov, N. B. Skibina, L. A. Mel'nikov, A. V. Shcherbakov, D. Chorvat, A. M. Zheltikov, "Self-phase modulation of femtosecond pulses in hollow photonic-crystal fibres," *Quantum Electronics* **34**, 56-58 (2004)
48. R. W. Void, "Ultrafast and intense field nonlinear optics," in *Nonlinear Optics* (Academic Press, San Diego), 533-560 (2003)

49. S. Zhang, G. Lüpke, "Spatial beam shaping of high power ultra-short pulses," in Laser Beam Shaping VII, F. M. Dickey and D. L. Shealy eds., Proc. SPIE **6290**, 62900E (2006)
50. D. E. Spence, P. N. Kean, and W. Sibbett, "60-fsec pulse generation from a self-mode-locked Ti:sapphire laser," Opt. Lett. **16**, 42-44 (1991)
51. M. M. Murnane, and H. C. Kapteyn, "Ultrashort light pulse: pushing the limits," IEEE Lasers and Electro-Optics Society Monthly Newsletter, August (1995)
52. S. A. Diddams, David. J. Jones, Jun Ye, T.M. Fortier, R. S. Windeler, S. T. Cundiff, T. W. Hänsch, and John L. Hall, "Optical frequency metrology and the phase control of femtosecond pulses--Towards the ultimate control of light," Optics and Photonics News **11**, 16-22 (2000)
53. D. Strickland, and G. Mourou, "Compression of amplified chirped optical pulses," Opt. Commun. **56**, 219-221 (1985)
54. S. Biswal, J. Itatani, J. Nees, and G. A. Mourou, "Efficient energy extraction below the saturation fluence in a low-gain low-loss regenerative chirped-pulse amplifier," IEEE Journal of Selected Topics in Quantum Electronics, **4**, 421-425 (1998)
55. F. Estable and A. Brun, "Direct Measurement of Saturation fluence in Ti: Al<sub>2</sub>O<sub>3</sub>," Opt. Comm. **72**, 235-238, (1989)
56. S. Seidel, "Improvement of extraction efficiency by regenerative amplification in an Nd: YAG-MOPA with a phase-conjugating SBS cell," Optical and Quantum Electronics, **27**, 625-632 (2004)

57. M. Pessot, J. Squier, P. Bado, G. Mourou, and D. J. Harter, "Chirped pulse amplification of 300 fs pulses in an alexandrite regenerative amplifier," *IEEE J. Quantum Electron.* **25**, 61-66 (1989).
58. P. Maine, D. Strickland, P. Bado, M. Pessot, and G. Mourou, "Generation of ultrahigh peak power pulses by chirped pulse amplification," *IEEE J. Quantum Electronics* **24**, 398-403 (1988)
59. C. Zhao, J. Degallaix, L. Ju, Y. Fan, D. G. Blair, B. J. J. Slagmolen, M. B. Gray, C. m. Lowry, D. E. McClelland, D. J. Hosken, D. Mudge, A. Brooks, J. Munch, P. J. Veitch, M. A. Barton, and G. Billingsley, "Compensation of strong thermal lensing in high-optical-power cavities," *Phys. Rev. Lett.* **96**, 231101 (2006)
60. Z. Cheng, F. Krausz, and C. Spielmann, "Compression of 2 mJ kilohertz laser pulses to 17.5 fs by pairing double-prism compressor: analysis and performance," *Optics Commun.* **201**, 145 (2002)
61. M. Schmid, R. Weber, and H. P. Weber, "Modeling of Thermal Birefringence in Longitudinal Diode-Pumped Nd:YAG Laser Systems," *CLEO Laser and Electro-optics Europe* **14**, 217 – 217 (1998)
62. H. Kiriya, T. Yoshida, N. Srinivasan, M. Yamanaka, Y. Izawa, T. Yamanaka, S. Nakai, T. Kanzaki, H. Miyajima, M. Miyamoto, H. Kan, and T. Hiruma, "Highly efficient thermal-birefringence-compensated laser-diode-pumped novel eight-pass Nd:YAG slab amplifier," *CLEO Lasers and Electro-optics* **11**, 369-370 (1997)
63. I. Shoji, Y. Sato, S. Kurimura, V. Lupei, T. Taira, A. Ikesue, and K. Yoshida, "Thermal-birefringence-induced depolarization in Nd:YAG ceramics," *Opt. Lett.* **27**, 234-236 (2002)

64. Furukawa, Hiroyuki; Hiura, Norimitsu; Kato, Yoshinori; Matsui, Hiroki; Yamanaka, Masanobu; Izawa, Yasukazu; Nakai, Sadao; Yamanaka, Chiyo, "Evaluation of thermal birefringence power loss in the laser-diode-pumped Nd:glass laser," in *Advanced High-Power Lasers*, Marek Osinski; Howard T. Powell; Koichi Toyoda; Eds Proc. SPIE **3889**, 610-618 (2000)
65. R. Fluck, M. R. Hermann, and L. A. Hackel, "Birefringence compensation in single solid-state rods," *Appl. Phys. Lett.* **76**, 1513-1515 (2000)
66. H. Kiriya, T. Yoshida, N. Srinivasan, H. Matsui, K. Nishida, M. Yamanaka, Y. Izawa, T. Yamanaka, and S. Nakai, "Thermal birefringence effect on the performance of a laser-diode pumped solid-state laser," *Jpn. J. Appl. Phys.* **36**, 7197-7201 (1997)
67. S. Lee, M. Yun, B. H. Cha, C. J. Kim, S. Suk, and H. S. Kim, "Stability Analysis of a Diode-Pumped, Thermal Birefringence-Compensated Two-Rod Nd:YAG Laser with 770-W Output Power," *Appl. Opt.* **41**, 5625-5631 (2002)
68. G. Cheriaux, and J. P. Chambaret, "Ultra-short High-intensity laser pulse generation and amplification," *Measurement Science and Technology*, **12**, 1769-1776 (2001)
69. J. Seres, A. Müller, E. Seres, K. O'Keeffe, M. Lenner, R. F. Herzog, D. Kaplan, C. Spielmann, and F. Krausz, "Sub-10-fs, terawatt-scale Ti:sapphire laser system," *Opt. Lett.* **28**, 1832-1834 (2003)
70. M. Hentschel, Z. Cheng, F. Krausz, Ch. Spielmann, "Generation of 0.1-TW optical pulses with a single-stage Ti:sapphire amplifier at a 1-kHz repetition rate," *Applied Physics B: Lasers and Optics* **70**, S161-S164 (2000)

71. R. Szipocs, K. Ferencz, C. Spielmann, and F. Krausz, "Chirped multilayer coatings for broadband dispersion control in femtosecond lasers," *Opt. Lett.* **19**, 201-203 (1994)
72. M. M. Wefers and K. A. Nelson, "Analysis of programmable ultrashort waveform generation using liquid-crystal spatial light modulators," *J. Opt. Soc. Am. B* **12**, 1343-1362 (1995)
73. J. Didierjean, S. Forget, S. Chenais, F. Druon, F. Balembos, and P. Georges, "High-resolution absolute temperature mapping of laser crystals in diode-end-pumped configuration," in *Solid State Lasers XIV: Technology and Devices*, H. J. Hoffman, R. K. Shori, eds, *Proc. SPIE* **5707**, 370-379 (2005)
74. R. D. Boyd, J. A. Britten, D. E. Decker, B. W. Shore, B. C. Stuart, M. D. Perry, and L. Li, "High-efficiency metallic diffraction gratings for laser applications," *Appl. Opt.* **34**, 1697- (1995)
75. B. C. Stuart, M. D. Perry, J. Miller, G. Tietbohl, S. Herman, J. A. Britten, C. Brown, D. Pennington, V. Yanovsky, and K. Wharton, "125-TW Tisapphire / Ndglass laser system ," *Opt. Lett.* **22**, 242-244 (1997)
76. Hammersley, J. M. "Monte Carlo Methods for Solving Multivariable Problems." *Ann. New York Acad. Sci.* **86**, 844-874 (1960)
77. W. H. Press, B. P. Flannery, S. A. Teukolsky, and W. T. Vetterling, "Simple Monte Carlo Integration" and "Adaptive and Recursive Monte Carlo Methods." in *Numerical Recipes in FORTRAN: The Art of Scientific Computing*, 2nd ed. (Cambridge University Press, Cambridge, England) 295-299 and 306-319 (1992)

78. C. W. Ueberhuber, "Monte Carlo Techniques." in Numerical Computation 2: Methods, Software, and Analysis. (Springer-Verlag, Berlin ) 124-125 and 132-138, (1997)
79. W. J. Tropf, M. Thomas, and T. J. Harris, "Optical and physical properties of materials," in Handbook of Optics, Volume II (McGraw-Hill Professional, New York) 33 (1994)
80. S. Y. Zhang, Y. H. Ren, and G. Lüpke, "Ultra-Short Laser Pulse Beam Shaping," Appl. Opt. **42**, 715-718 (2003)
81. S. Y. Zhang, Q. Yang, and G. Lüpke, "Spatial beam shaping of ultrashort laser pulses: theory and experiment," Appl. Opt. **44**, 5818-5823. (2005)
82. G. P. Banfi, D. Fortusini, M. Bellini, and P. Milani, "Wave-dispersed two-photon absorption of C<sub>60</sub>," Phys. Rev. B **56**, R10075 - R10078 (1997)

## **VITA**

Shuyan Zhang

Shuyan Zhang was born in Luoyang, China on February 13, 1974. Shuyan Zhang received his B.S. in Physics at Fudan University in 1997. He received his M.S. degree at Fudan University in 2000, with a concentration in Optics.

In August 2000, the author entered the College of William and Mary as a research assistant in the Department of Applied Science. With the completion of the thesis and satisfaction in all other degree requirements, the author received his Ph. D. Degree in Applied Physics in August 2007.